DISSERTATION ZUR ERLANGUNG DES DOKTORGRADES

DER FAKULTÄT FÜR CHEMIE UND PHARMAZIE

DER LUDWIG-MAXIMILIANS-UNIVERSITÄT MÜNCHEN

MULTIFUNCTIONAL MESOPOROUS NANOPARTICLES FOR CATALYSIS, SENSING AND DRUG DELIVERY APPLICATIONS

STEFAN NIEDERMAYER

aus

Rain am Lech

2013

Erklärung

Diese Dissertation wurde im Sinne von § 7 der Promotionsordnung vom 28. November 2011 von Herrn Prof. Dr. Thomas Bein betreut.

Eidesstattliche Versicherung:
Diese Dissertation wurde eigenständig und ohne unerlaubte Hilfe erarbeitet.

Ort, Datum	Unterschrift

Datum der Einreichung: 14.11.2013

1. Gutachter: Prof. Dr. Thomas Bein

2. Gutachter: Prof. Dr. Christoph Bräuchle

Tag der mündlichen Prüfung: 17.12.2013

Danksagung

Diese Arbeit wäre nicht möglich gewesen ohne die Unterstützung von vielen Leuten, welchen ich meine tiefste Dankbarkeit aussprechen möche.

Als Erstes möchte ich mich bei meinem Doktorvater Professor Thomas Bein für die Aufnahme in seine Forschungsgruppe sehr herzlich bedanken. Die steten Diskussionen über laufende Projekte und vor allem das Vertrauen in den Erfolg von selbst erdachten Forschungsarbeiten haben mich sehr motiviert. Ausserdem bedanke ich mich für die Unterstützung bei meinem Stipendienantrag, sowie für die unermüdliche Hartnäckigkeit bei dem "Kampf" mit der Personalabteilung um meine vertragliche Einstufung. Auch für die Möglichkeit, meine Projekte auf zahlreichen Konferenzen präsentieren zu können, bin ich sehr dankbar. Highlights für mich waren hier sicherlich die NanoHealth Konferenz in Seoul, sowie das MRS spring meeting in San Francisco.

Professor Christoph Bräuchle möchte ich ebenfalls sehr herzlich für die exzellente Zusammenarbeit danken. Durch die gemeinsame Kooperation und die stets sehr interessanten Meetings konnte ich viel lernen. Zusätzlich bedanke ich mich sehr herzlich für die Erstellung des Zweitgutachtens.

Bei Professor Ernst Wagner möchte ich mich ebenfalls für die tolle Kooperation und die Einführung in die Welt der Tierexperimente bedanken. Diese Experimente haben uns grundlegende Einsichten über das Verhalten unserer Partikel in lebenden Tieren gewährt.

Des Weiteren möchte ich Danke sagen bei Privatdozent Stefan Thalhammer für die Kooperation im Dengue Fieber Projekt. Zusätzlich möchte ich mich noch für das

Ausleihen der vier Taschenatlanten bedanken, welche es hoffentlich bei der Verteidigung zurück gibt.
Ein riesiges Dankeschön geht an Veronika Weiß für die unendlich vielen Zellbilder meiner Partikel und der Bereitschaft immer wieder neue Experimente zu entwickeln und durchzuführen. Ausserdem auch dafür Danke, dass Du mir nie böse gewesen bist, wenn die Proben mehr Bakterien als Partikel enthalten haben.
In Verbindung mit diesem Projekt gilt mein Dank auch Annika Herrmann und Dr. Daniel Edinger aus der Gruppe von Professor Ernst Wagner. Vielen Dank für die viele Zeit (vor allem von Annika im Tierstall), die sofortige Bereitschaft an dem Projekt zu arbeiten und natürlich mir immer wieder zu erklären welches Signal zu welchem Organ in den Tieren gehört.
Aus der Gruppe von Stefan Thalhammer möchte ich mich ganz herzlich bei Elisangela Linares für die tolle Kooperation und die Ausdauer, nach den anfangs nicht gerade ermutigenden Ergebnissen, bedanken. Schön dass es sich am Ende gelohnt hat immer wieder neue Dinge zu testen.
Aus der eigenen Gruppe möchte ich mich für die Kooperation mit Dr. Benjamin Mandlmeier bedanken. Durch die Zusammenarbeit konnten wir nicht nur eine Publikation schreiben, sondern ich konnte mich dadurch auch über der Türe in dem Labor im zweiten Stock verewigen. Meinem langjährigen Bürokollegen Benni gilt neben dem Dank für die exzellente wissenschaftliche Zusammenarbeit, auch besonderer Dank für die tägliche Kooperation an der Kaffeemaschine und dem Geschirrspüler. Herzlichen Dank auch an Stefan und Andi für die Bereitstellung der MIL-Nanopartikel und die interessanten Diskussionen zu diesem Thema. Bedanken möchte ich mich auch bei Christian, Basti und Alex für die vielen lustigen Tage und Wochen auf Konferenzen in der ganzen Welt. In diesem Zusammenhang möchte ich mich ganz herzlich bei den Mitgliedern der MesoBio Subgroup, Anderl, Axel, Valentina, Basti, Alex, Christian, Cindy, Karin, Noggi, Martina und Stefan für die sehr unterhaltsamen und konstruktiven Gespräche bedanken. Vielen Dank natürlich auch an den Rest der Gruppe für die lustige Zeit und dafür dass ich als "Externer" so super aufgenommen wurde. Ganz besonders möchte ich mich auch

bei meinen Bürokollegen, Johann, Benni, Fabi, Hans, Norma, Flo, Ilina, Enrico und Mona für die tolle Zeit und die gebotene Abwechslung zum harten Laboralltag bedanken. In diesem Zusammenhang bedanke ich mich auch beim Hedgefonds-Team, unnamed, Flo, Team Amerika und BrinkyBain für die unzähligen Schneebälle und Wassermelonen.

Ein herzliches Dankeschön geht an Basti für die vielen PovRay Kunstwerke, welche ganz entscheidend zur Illustrierung der einzelnen Projekte beigetragen haben. Vielen Dank für die unzähligen Stunden die du hierfür am PC verbracht hast. **Ganz besonderer Dank gilt Tina** dafür, dass sie sich um einfach ALLES kümmert und uns Doktoranden das Leben so einfach wie möglich macht. Ausserdem kann man Tina zu jeder Zeit aufsuchen und sie findet immer ein offenes Ohr für die Sorgen und Nöte, nicht nur im wissenschaftlichen Sinn. **Ebenso möchte ich mich bei Regina bedanken.** Insbesondere dafür dass Regina mir als verwaltungstechnischem Analphabeten immer wieder (und wenn es sein musste auch wiederholt) erklärt hat, wie welches Formular auszufüllen ist und mir somit viel Zeit und Nerven erspart hat. Dank gilt auch meiner Bachelorstudentin Tanja, sowie meinen Praktikanten Sarah, Marina, Martina, Carina, Sarah, Arne, Evelyn und Wenyu. Bedanken möchte ich mich auch bei Evelyn für ihr Vertrauen, nach ihrem Praktikum auch noch ihre Masterarbeit von mir leiten zu lassen.

Besonderer Dank gilt gilt meinen Elten für die tatkräftige Unterstützung in all den Jahren. Vor allem bin ich sehr dankbar dass sie mir ermöglichten ein Semester in Bath und zwei Semester in Paris zu studieren. Ihre persönliche und finanzielle Unterstützung und die Tatsache dass sie sich für meine Arbeit interessierten (auch, wenn es manchmal nicht so leicht zu erklären war, was ich hier so treibe) machten diese Arbeit überhaupt erst möglich.

Ausserdem möchte ich mich bei meiner geliebten Sabine für ihre stete Unterstützung bedanken. Dir, liebe Sabine, danke ich von ganzem Herzen dass du immer für mich da bist und dein Leben mit mir teilst. Ich freue mich schon sehr auf unsere gemeinsame Zeit im schönen Rain. Danke.

Abstract

Mesoporous materials have attracted increasing attention in the past decades. Based on host-guest interactions, many different applications in the fields of catalysis, drug delivery, separation of fine chemicals, adsorption of biomolecules, or more recently, water-splitting, photovoltaic and energy storage have been demonstrated with this class of materials. Infiltration of the mesoporous frameworks can lead to composites with properties that differ from the individual bulk materials. Hence, knowledge about the interactions of the guest species with the pore walls plays an important role for the creation of new systems. The synthesis of mesoporous nanoparticles offers the possibility to design concepts that can be used in targeted drug delivery and biological sensing applications.

The present work is focused on the synthesis and modification of nanometer-sized, mesoporous materials and their investigation for the use in biocatalysis, targeted drug delivery and immunoassay applications.

Information on the pH inside the pores of mesoporous silica particles was gained by infiltration with pH indicator molecules. With this approach, we could show that the pH inside the pores of mesoporous silica immersed in buffer solutions may differ significantly from the bulk pH, depending on the pore size of the material and the ionic strength of the buffer solution. Covalent attachment of catalytic centers within the mesopores allowed us to investigate the impact of pore wall functionalization on the catalytic performance of the catalyst-silica composite material.

In a second project, a cap system for nanosized mesoporous carbon spheres was developed. It was demonstrated that surface oxidation of carbon spheres synthesized by an inverse opal templating technique results in stable colloidal suspensions

of single particles that can be sealed with a supported lipid bilayer. For the first time we were able to show successful capping and on demand release of guests from mesoporous carbon materials.

pH-responsive release of different cargos and targeting of specific cells was investigated in a joint project between the groups of Prof. Bein, Prof. Bräuchle and Prof. Wagner. We developed a modular toolbox based on a mesoporous silica core, capped with a pH-responsive polymer. The use of bifunctional polymers allowed the sequential attachment of different functionalities, depending on the final task of the delivery vehicle. With this system, we were able to demonstrate successful delivery of different cargos into living cells and targeting thereof. Animal experiments in mouse models revealed an excellent biodistribution of the nanocarriers, as well as succcesfull targeting of KB breast cancer *in vivo*.

This concept of pH-responsive capping of nanoparticles with polymers was transferred to a different class of material. We used crystalline metal-organic framework nanoparticles, to create a drug delivery system based on this material. The particles were functionalized with the same polymer-based cap system that was developed for mesoporous silica. In this project, we could demonstrate on demand release of fluorescent dyes as model drugs upon changing the pH of the media.

Finally, together with the group of PD Dr. Stefan Thalhammer we introduced a completely new field of application for mesoporous silica nanoparticles. By incorporation of catalytic centers into the cores and attachment of recognition sites to the outer surface, we were able to demonstrate the use of these multifunctional nanoparticles in immunoassay applications. Compared with state of the art detection systems for NS1 antigens, we were able to show enhanced performance of our system.

To summerize, three different topics were investigated in this thesis. In a first project, we could gain insights into the behavior of catalytic centers within differently functionalized mesoporous silica. In further projects, a variety of drug delivery systems was introduced. Additionally, we introduced a completely new field of application for mesoporous silica nanoparticles aimed at immunoassay based biosensing.

Contents

Chapter 1

Introduction

1.1 The history of porous materials

Before 1992, two classes of materials were used extensively as heterogenous catalysts, adsorption media and ion exchangers. These materials consisted of microporous (pore diameters $\leq$ 20 Å) and mesoporous ($\sim$ 20-500 Å) inorganic solids.[1,2] In the last 20 years, advances in various fields such as hydrogen storage,[3–5] heat storage,[6] photovoltaics,[7,8] chemical sensors,[9–11] nanodevices[12,13] and medical applications[14,15] require the development of ordered porous materials with controllable size and pore morphology.[16] Zeolites, having pore diameters in the range of 0.5 to 1 nm, have pores which are too small for immobilization of enzymes, antibodies or the controlled release of large molecules. Therefore mesoporous silica materials with larger pore diameters had to be developed. In their well-known paper, Kresge and co-workers from Mobil Oil company introduced a means of combining sol-gel chemistry with liquid-crystalline templating to create a novel type of silica-based molecular sieves named the M41S family including MCM-41 (MCM = Mobile Composition of Matter), with 2D hexagonal pore arrangement, MCM-48 with a 3D cubic pore system and MCM-50 with a 1D arrangement of layered sheets.[1,17] In this type of material, the pores were templated by surfactants, whereas the walls were build from amorphous silica. After removal of the surfactant, an open porous structure with an internal surface area of around 1000 m^2g^{-1} and pore diameters

in the range of 3-5 nm were obtained. Subsequently different synthesis strategies and numerous kinds of surfactants were developed. Today, it is possible to synthesize materials with pore sizes in the range of 2-50 nm, and pore arrangements, particle sizes and shapes[16] that are tailor-made for many applications of interest like controlled release,[18] immobilized enzymes for catalysis,[19,20] or the growth of nanowires within the confined space of cylindrical mesopores.[21–23]

In the late 1980's, advances in the synthesis of zeolites drew academic attention towards the synthesis of new classes of porous materials.[24–26] A very important class of porous compounds was introduced in 1995 by Yaghi *et al.*.[27] The concept of "metal organic frameworks" (MOFs) is based on the formation of a three-dimensional hybrid framework consisting of inorganic metal ion centers and organic linkers. These frameworks typically consist of di-, tri-, or tetravalent metal centers connected by chelating organic linker molecules. As chelating groups carboxylates, phosphonates, sulfonates and nitrogen derivatives have been reported.[25,28] Similar to the development of zeolites, the first published examples of MOFs showed microporosity. A few years later, Ferey *et al.* reported the first mesoporous MOF with a pore size of $\geq$ 2 nm.[29] Moreover, this new "MIL" (Materiaux de Institut of Lavoisier) was the first crystalline mesoporous solid.[30] The MOF material with the largest pores so far was reported by Deng *et al.* with an average pore size of 9.8 nm which is large enough to incorporate proteins like GFP.[31] Related to the concept of metal organic frameworks, Yaghi *et al.* developed porous materials with covalent bonds instead of coordinative bonds. This material was named covalent organic frameworks (COFs) and can be obtained by the reversible condensation reaction of organoboronic acids with diol-moieties.[32] With this approach 1D porous networks can be synthesized. Linear pores are formed *via* $\pi - \pi$ interactions between the layers. Dogru *et al.* showed the great potential of these materials as conducting and light absorbing electrodes in photoelectronic devices.[33]

1.2 The synthesis of mesoporous silica materials

Mesoporous silica materials are usually synthesized *via* a liquid-crystal templating approach, in which alkoxysilanes condense around a template that determines the final shape of the pores. As template materials, surfactants or combinations of surfactants and small molecules are used. Cooperative self-assembly and "true" liquid-crystal templating processes are the two main pathways in the synthesis of mesoporous structured materials, as shown in Figure 1.1.[16]

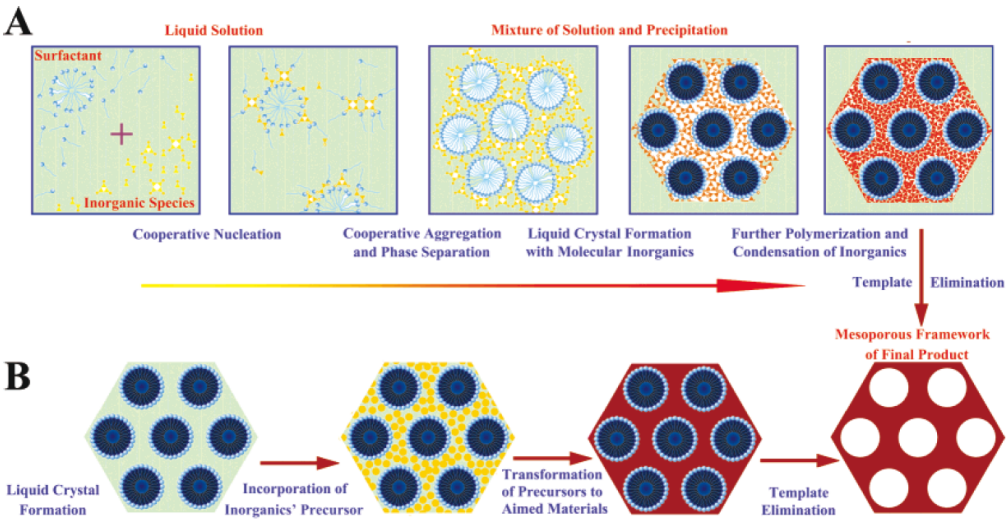

Figure 1.1: Two strategies for the synthesis of mesoporous materials: (A) cooperative self-assembly; (B) "true" liquid-crystal templating process.[16]

Condensation of the silica source can either be acid or base catalyzed, and water or alcohols are usually used as solvents. Many different synthesis protocols have been described, depending on the nature of surfactant and precursor molecules.[16,34,35] In the case of cationic surfactants, strong ionic interactions between the positively charged headgroup of the template (e. g. CTAC, CTAB) and the negatively charged oligosilicates strongly influence the formation mechanism of mesoporous silica, and no initial liquid crystalline phase is required.[36,37] Coulomb forces lead to an assembly of positively charged headgroups of the template around negatively charged silica oligomers. This balance in charge drastically reduces the template's solubility within the aqueous reaction mixture and leads, as a result of optimization of the interfacial

energy, to the formation of micelles. The final mesostructure is formed by further polymerization of the silicate species (Figure 1.1 A).[16] The second prominent pathway discussed in the literature is called the "true"' liquid crystal templating pathway. Here, true or semi-liquid-crystal mesophases are already present under the reaction conditions, which often requires high concentrations of usually nonionic surfactants (e. g. Pluronic P123, F127) as templates.[38] Condensation of inorganic precursors around these liquid crystals leads to frameworks with amorphous pore walls (Figure 1.1 B).[16] The evaporation induced self assembly method (EISA), which is used in the preparation of mesoporous silica films can also be assigned to this pathway.[39,40]

1.3 Mesoporous silica nanoparticles

In the early stage of mesoporous silica research, the main focus was based on the development of materials with different pore sizes, morphologies and the formation mechanisms thereof. The most famous families, MCM and SBA show particle diameters in the micrometer range. Many applications such as drug delivery require mesoporous nanoparticles with diameters in the range of 20-300 nm. With a careful control of the self-assembly process and the silica condensation rate, not only mesostructures and morphologies, but also the particle size can be tailored.[41] In 1999, Brinker and coworkers developed an aerosol-based procedure for the preparation of mesoporous silica nanospheres (MSNs) with different pore morphologies.[42] This method relies on an EISA process taking place in the confined space of small aerosol droplets (Figure 1.2).

Small droplets of a homogeneous water/ethanol solution containing silica precursors and surfactants in a concentration below the critical micelle concentration are created by an atomizer and pass through a reaction chamber with different temperature zones, followed by separation of the resulting particles. Using different structure directing agents, lamellar, cubic or hexagonally ordered mesoporous silica particles with a geometric size distribution of 2 were obtained. With this method,

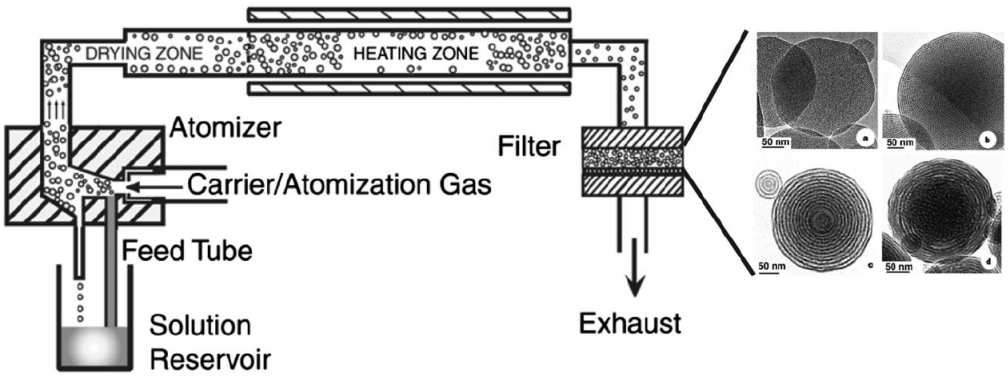

Figure 1.2: Left: Diagram of the aerosol reactor. Right: TEM micrographs of mesostructured nanoparticles obtained with this method.[41,42]

particles with a size distribution around 120 nm and tunable pore sizes between 3 and 40 nm were synthesized.

Grun,[43] Cai,[44] Mann[45] and Ostafin[46] were the first who succeeded in the synthesis of mesoporous silica nanoparticles from solution in a modified Stöber method. Submicrometer sized MCM-41 spherical particles were prepared by Grün *et al.* in a modified Stöber method simply by adding a cationic surfactant to the synthesis mixture.[43] Uniform MSNs with different pore sizes and mesostructures were synthesized from mixtures of alcohol, water, ammonia and different structure directing agents. It was found that monodisperse MSNs are formed through aggregation of small clusters during the initial stage of the synthesis.[47] By seperating the nuclei formation from the particle growth, Mou *et al.* were also able to synthesize monodisperse MSNs.[48] The size of the MSNs could be modulated by the variation of the pH in the reaction solution.[49] Lower pH values resulted in smaller particles due to higher condensation rates and thus production of more nuclei.

Suzuki *et al.* synthesized MSNs with a dual surfactant system. In their approach a cationic surfactant acting as structure directing agent and the non-ionic surfactant Pluronic F127 serving as a steric stabilizer was used. Pluronic F127 formed a layer around the surfactant-silicate hybrid material and suppressed grain growth, which resulted in MSNs with a mean diameter of 50 nm in a concentrated solution.[50] Besides non-ionic surfactants, other surface protecting agents like PEG,[51] L-lysine[52] and triethanolamine (TEA)[53] were used to limit particle growth.

1.4 Functionalization of mesoporous silica

For the incorporation of specific functionalities into mesoporous silica, reactive groups bearing organic moieties have to be attached to the silica surface. Functionality can be introduced *via* the modification of silanol groups present at the surface. The groups show chemical reactivity and can be reacted with alkoxy- or chlorosilane derivatives to introduce organic functionality *via* a condensation reaction. Generally, two main approaches of modification exist: co-condensation and postsynthethic grafting.[54]

Co-condensation. The co-condensation approach involves the condensation reaction between tetraalkoxysilanes with organoalkoxysilanes (R'$_x$Si(OR)$_{4-x}$), which results in a direct modification of the surface.[55] In a first step, the organosilanes are hydrolyzed which changes their hydrophilic/hydrophobic balance. The resulting hydroxysilanes serve as a cosurfactant that is incorporated *via* the organic residue into the micelles. A major drawback of this method is the relatively low achievable degree of functionalization as the incorporation into the micelles can lead to less order of the mesoporous structure in the final material. On the other hand, sequential co-condensation offers the possibility to synthesize mesoporous silica nanoparticles with orthogonal functionalities in the pores and on the outer surface as shown in figure 1.3.[56]

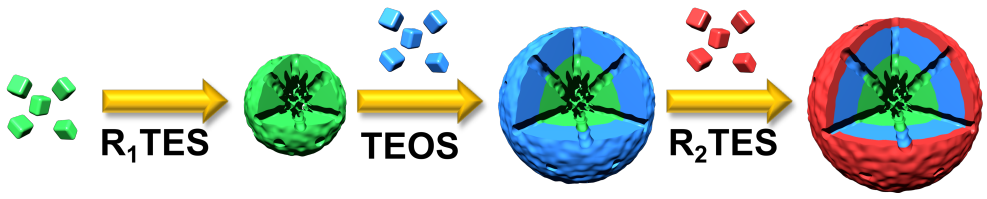

Figure 1.3: Co-condensation approach for the creation of core-shell-functionalized MSNs.

Postsynthetic grafting. In the postsynthetic grafting approach, mesoporous materials are functionalized after synthesis. Hydroxyl groups present within the mesopores and at the external surface are condensed with trifunctional organosilanes R'Si(OR)$_3$ in organic solvents. This method shows two major advantages

compared to the co-condensation approach: First, maximal surface coverage can be achieved without pertubation of the order of the mesoporous framework. Second, further stabilization of the mesoporous framework by calcination can be conducted prior to the functionalization. On the other hand, several drawbacks limit the use of the postsynthetic grafting method compared to the co-condensation approach. Multilayer deposition of the organosilane can lead to a decrease in pore-size and to the formation of bottle-necks at the entrance of the pores. As the whole surface of the material is functionalized, the direct synthesis of core-shell-functionalized materials is not possible.
More recently, alternative routes to achieve organic functionality on mesoporous materials have been reported. The direct formation of Si-C bonds with metalorganic reagents like Grignard or organolithium compounds were introduced.[57,58] With this method, multilayer deposition can be avoided, but the relatively harsh conditions can lead to a partial degradation of the mesoporous material.

1.5 Targeted drug delivery with mesoporous silica nanoparticles

In recent years, functional nanoparticles have attracted much attention in the fight against various diseases including bone tissue engineering,[59] diabetes,[60,61] inflammation[62] and cancer[63] which can be seen in the number of publications per year (Figure 1.4).[64]

With the help of nanoparticles, drug molecules can be hidden inside the carrier until the delivery vehicle has reached its target site. After arriving at the desired tissue or single cells, the sealing of the nanoparticles needs to be opened either independently or by an external trigger. Targeted drug delivery can offer several advantages like reduced drug doses or minimized side effects. In this context, MSNs contribute significantly to overcome several challenges due to their high internal surface area and pore volume, tunable pore sizes, colloidal stability and the possibility

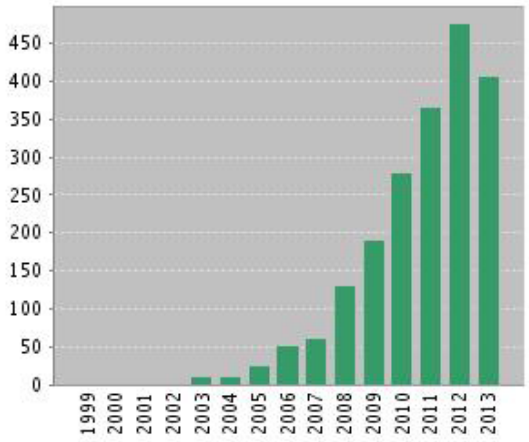

Figure 1.4: Statistics of papers indexed in the ISI web of science by the topic of "mesoporous silica" and "drug delivery". [64]

to attach different kinds of functionalities to a single particle. Since mesoporous silica exhibits excellent biocompatibility, [65–67] it has been widely investigated as a drug delivery platform in targeted drug delivery. [68–70] To be able to serve as a multifunctional delivery tool, the final particle has to fulfill several requirements as shown in figure 1.5. [71]

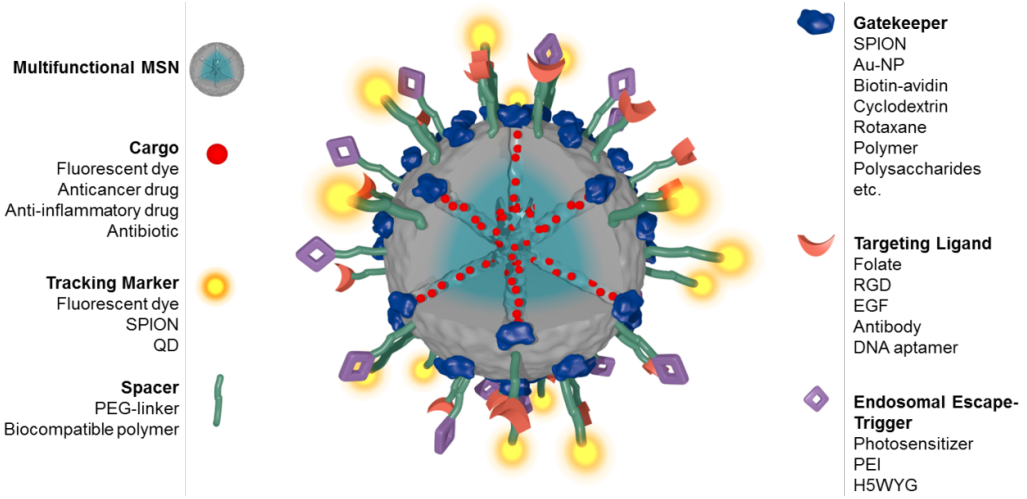

Figure 1.5: Cartoon of an ideal drug delivery vehicle based on MSN. [71]

In the cartoon, several different possible functionalizations are depicted. The basis of the system is built by a multifunctional mesoporous silica nanoparticle. Core-

shell architecture with orthogonal functionalities offers the possibility to achieve control over interactions of drug molecules with the pore walls whereas different moieties can be selectively attached to the outer particle surface. To prevent premature release of the cargo (red) from the nanoparticles, gatekeeping molecules (blue) need to be attached that enable opening and closing of the pores on demand. This can be accomplished either by conformational changes of the gatekeeper itself or by decomposition or changes in chemical properties of the linker molecule between the MSN and the gatekeeper. Further attachment of fluorescent labels (yellow) allows to track mechanisms of cellular uptake and quantification of MSNs within cells with fluorescence spectroscopy. Targeting ligands (orange) enable attachment of MSNs to specific receptors overexpressed on the desired cancer cell surface. Spacer molecules (green) are essential to ensure good dispersability of the carrier system in the body to avoid undesired agglomeration in healthy tissue. Optionally, if membrane non-permeable molecules have to be delivered, a trigger for endosomal release (purple) is required to release the cargo into the cytosol of the cancer cell. If it is possible to implement all requirements mentioned above within a single particle, the efficacy of state of the art therapy approaches can be significantly enhanced while simultaneously reducing financial costs.

1.5.1 Stimuli-responsive gatekeeping systems

To achieve the final goal of targeted drug delivery, it is important to release the drug only at the desired location under defined conditions. In the last 15 years many different concepts of molecular capping systems were investigated, attracting researchers from various scientific disciplines. So far, the most prominent release mechanisms include enzyme-responsive, redox-responsive, light-responsive, temperature-responsive or pH-responsive systems of different kinds. Most gatekeeping systems reported so far rely on the use of bulky object like proteins, cyclodextrins or inorganic nanoparticles that block the pores after attachment to the external silica surface.[72–75] Schlossbauer *et al.* reported on a delivery system based on the strong interaction between biotin and avidin.[74,76] In a first publication, MSNs were reacted

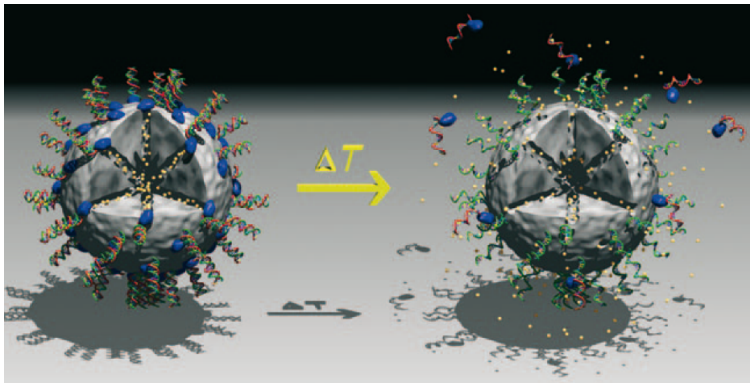

Figure 1.6: Concept of a programmable molecular valve system. The avidin caps are opened by melting the DNA linkers at specifically chosen temperatures.[76]

on the outer particle surface with biotin. After loading of a fluorescent model drug, avidin was added to seal the particles. Release experiments showed tight closure of the system prior to the addition of the protease trypsin which led to degradation of the protein cap. Based on these findings, a programmable temperature responsive system was developed (Figure 1.6). In this approach, one strand of a double-stranded DNA was attached to the outer surface of MSN. The second strand was functionalized in a way that after hybridization of the DNA, biotin was located close to the particle surface. In this system, the release depended on the melting temperature of the DNA which depends on the length of the double-strands.

A redox-responsive release mechanism was studied by Lin *et al.*. CdS or iron oxide nanoparticles were attached *via* a disulfide-bridge containing linker. They were able to show a release of vancomycin and adenosine triphosphate upon addition of reducing agents like mercaptoethanol or dithiothreitol that are able to reduce disulfides to thiols.[72,77] Photoresponsive release of rhodamine B was introduced by Zink *et al.* by using the fact that β-cyclodextrines (β-CD) show different affinity towards azobenzenes in different conformational states.[78] The high affinity of β-CD to trans azobenzenes was used to create a tight sealing around MSNs. Irradiation of the sample led to a conformational change in the azobenzene unit resulting in detachment of β-CD followed by the release of rhodamine B. Lin *et al.* showed that gold nanoparticles attached *via* a photocleaveable linker to MSNs can act as a

photoresponsive drug delivery vehicle (Figure 1.7).[79] By irradiation with UV-light, the linker molecule is cleaved, resulting in a negatively charged part connected to the gold nanoparticle that is repelled by the also negatively charged silica surface.

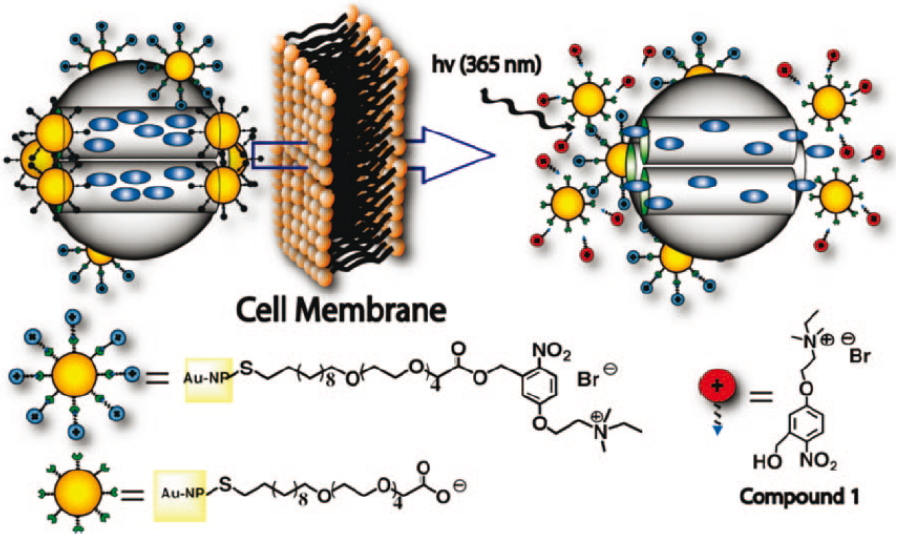

Figure 1.7: Cartoon of the construction and function of a photocleaveable delivery vehicle.[79]

In 2003, Tanaka and co-workers designed a photo-controlled reversible drug release system based on MCM-41 that does not rely on the concept of bulky stoppers attached *via* cleaveable linker molecules to the particle surface.[80] They showed that attachment of coumarin molecules to MCM-41 results in cyclobutane coumarin dimers upon irradiation with UV-light (310 nm) followed by sealing of the pore entrances of MCM-41. Reversible opening was achieved when the wavelength of UV irradiation was changed to 250 nm. A similar approach without bulky gatekeepers was introduced by our group in which the pH-dependent release of ibuprofen from MSNs was shown.[81] MSNs functionalized with aminopropyl-functionalities on the outer surface were reacted with 4-sulfophenyl isothiocyanate. Closure was obtained *via* the interaction of the sulfonic acid groups and the remaining protonated aminogroups at the surface. The release of ibuprofen was triggered by an increase of the pH in the solution leading to electrostatic repulsion of the sulfonic acid moiety and the silica surface. A very sophisticated approach for sealing MSNs was reported by Zink *et al.*. They designed a base-activated Curcurbit[6]uril (CB[6]) pseudoro-

taxane cap-system attached to the silica surface *via* an azide-alkyne cycloaddition. Upon deprotonation at pH 10, CB[6] detached from the surface resulting in a release of the model drug (see Figure 1.8).[82] This concept was further developed into an acid-activated cap system by the same group.[83] The organic chain was functionalized in a way that it contains three ammonium moieties: two tetramethylene and a terminal anilinium unit (see Figure 1.8). The function of the MSNs relies on the difference in basicity of the anilinium nitrogen atom in comparison with the other two tetramethylene nitrogen atoms. The anilinium nitrogen atom is approximately 10^6-fold less basic than the alkyl nitrogen, resulting in a deprotonation at neutral pH of the former. Lowering the pH to the point were the anilinium nitrogen is protonated leads to a release of the CB[6] followed by the release of the model drug. Increasing the pH to a point where all three nitrogen groups are deprotonated leads to a complete lift-off of the CB[6]-cap. Whereas the opening at low pH is reversible, a complete loss of the cap is observed for high pH values.

A combination of the high loading capacity of MSNs with the exceptional biocompatibility of phospholipid bilayers was introduced by Brinker *et al.*, the so-called supported lipid bilayer (SLB).[84] The whole particle surface was completely surrounded by a lipid bilayer made of 1,2-dioleolyl-3-trimethylammoniumpropane (DOTAP) and 1,2-dioleolyl-*sn*-glycero-3-(phospho-L-serine) (DOPS) by an electrostatically driven liquid exchange mechanism. In further publications, the successful targeted delivery of different cargos into living cells was shown.[85,86] In our group, the concept of SLB was extended by the attachment of photosensitizers that enable endosomal escape.[87] Upon illumination with light (405 nm) singlet oxygen is produced by the photosensitizer which leads to a cascaded rupture of the SLB followed by degradation of the endosomal membrane. Subsequently, the loaded drug can diffuse out of the mesopores directly into the cytosol as shown in figure 1.9. Schlossbauer *et al.* were able to show the release of chromobodies and their subsequent coordination to GFP-tubulin of HuH7 cells with this system.

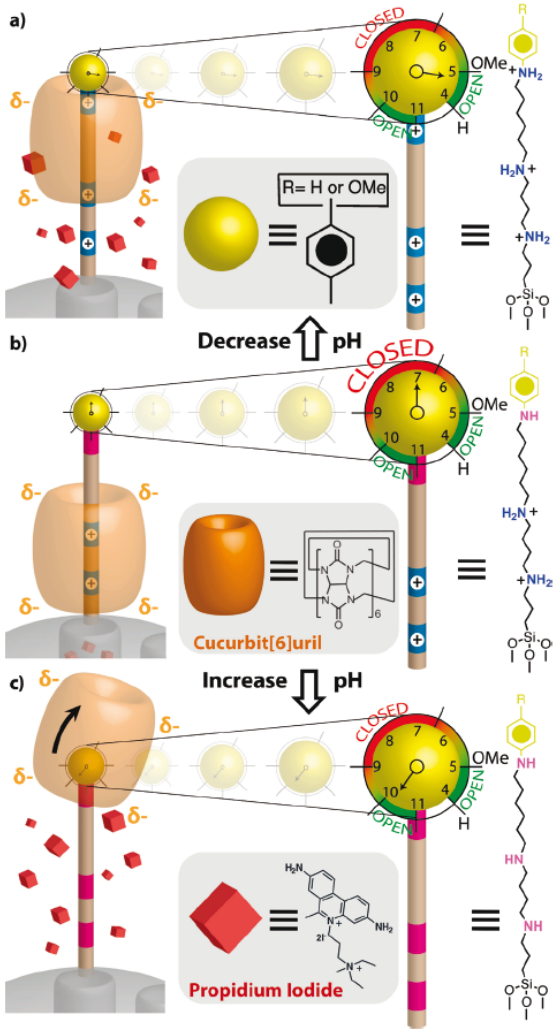

Figure 1.8: Cartoon of the construction of an pH-activated Curcurbit[6]uril capped MSN.[83]

In a further development of this project, large-pore MSNs were coated with a supported lipid bilayer.[88] As trigger for endosomal escape, a red-light-photosensitizer was used. This system offers two major advantages: first, MSNs with larger pores offer the possibility to deliver space-demanding cargos like proteins or RNA. Second, the activation of the photosensitizer with red light instead of blue light reduces the phototoxicity and significantly increases the depth of tissue penetration.

A different way to achieve full surface coverage of MSNs is the use of functional polymer coatings. You *et al.* used the fact that Poly(*N*-isopropylacrylamide) (PNIPAM) shows a change from a hydrated to a dehydrated state at the lower critical solution temperature (LCST) as demonstrated in Figure 1.10.[89] The resulting

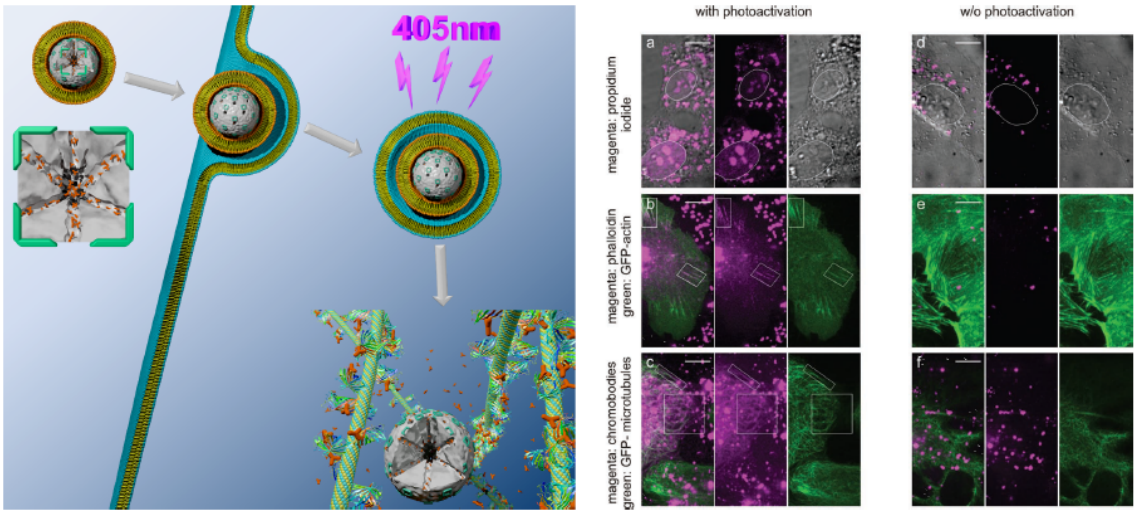

Figure 1.9: Left: Schematic representation of photoinduced delivery of chromobodies (red) and their subsequent coordination to GFP-tubulin of HuH7 cells. Right: Confocal microscopy of living HuH7 cells exposed to MSNs loaded with different model drugs.[87]

polymer-nanoparticle composite showed uptake and release of a model drug at temperatures below the LCST (38 °C), whereas at temperatures above the LCST good sealing of the pores was reported.

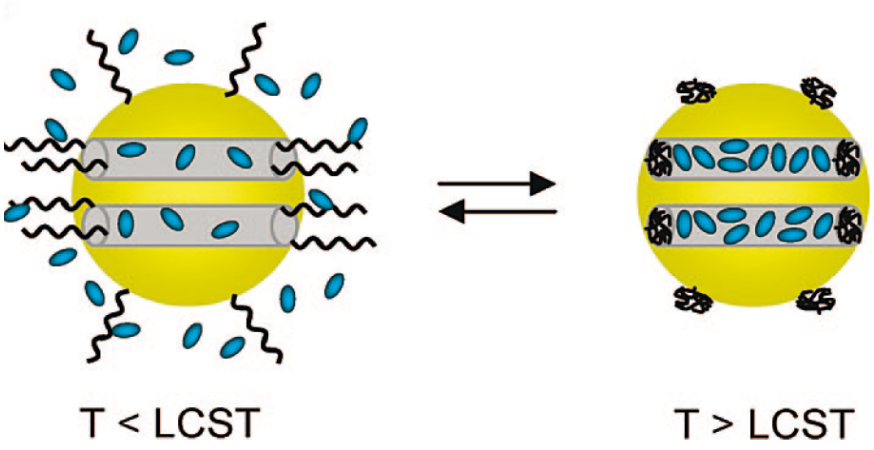

Figure 1.10: Schematic representation PNIPAM-polymer-nanoparticle composites.[89]

Using different polymers, Lopez and co-workers designed a system in which release was observed at temperatures above the LCST.[90,91] Additionally redox-responsive polymeric cap systems have been reported.[92] The system consists of poly(*N*-acryloxysuccinimide)-grafted MSNs, in which the polymer was attached to

the pore entrance. After loading of the model drug, the openings were blocked by the addition of a disulfide-based bifunctional primary amine, leading to cross-linking of the polymer. Addition of reducing agents like dithiothreitol led to reduction of the disulfide bridges resulting in redox-controlled release of the model drug. Liu *et al.* reported on pH-responsive release of model drugs out of poly(4-vinylpyridine) (P4VP) capped MSNs.[93] P4VP was attached *via* multipoint anchoring of the amine residue to the surface of brominated MSNs. At high pH, the deprotonation of the polymer produced a hydrophobically collapsed state and inhibited the release of trapped molecules. In the swollen state at low pH, the polymer was permeable to molecular diffusion, leading to pH-controlled release.

1.5.2 Drug delivery without capping systems

Another possible approach to confine drugs is their covalent attachment to the pores of MSNs. The major advantage of this approach is that synthetically demanding gatekeeping systems are not necessary. As the delivered species themselves are reversibly attached to the pore walls, they have to feature at least one functional group that allows for reversible binding. Using this approach, Lin *et al.* reported on the successful delivery of the membrane impermeable thiol-containing aminoacid cystein into living cells.[94] Cystein was reversibly attached to thiol functionalized MSNs *via* disulfide bridges. These bridges can either be cleaved *in vitro via* addition of DTT or *in vivo* by the reductive milieu of the cytosol. This approach was further investigated by live-cell imaging in our group as a joint project with the research group of Prof. Bräuchle.[95] Direct immobilization of compounds is very interesting for the delivery of sterically demanding molecules like proteins, as it is very challenging to seal large-pore materials. Schlossbauer *et al.* have demonstrated the successful immobilization and release of the bee venom melittin attached *via* an acetal linker.[96] After acidification of the sample, the acetal linkers were cleaved and melittin was able to diffuse out of the pores of SBA-15. Cell experiments showed that the protein retained its orignial function after the whole procedure. Gao *et al.* designed a versatile pH-responsive system based on the coordinative bonding of metal ions to

amino-groups in the mesopores.[97] Nitrogen-bearing guest molecules were immobilized at free coordination sites of the metal forming a ”host-metal-guest" architecture. Successful release of anticancer drugs bearing coordinatively binding groups was achieved by lowering the pH. Light induced cis-trans isomerization of azobenzenes (”nanoimpellers") was proven to accelerate the release of small molecules from mesopores (Figure 1.11).[98] Continuous illumination at 413 nm causes a constant cis-trans photoisomerization about the N=N bond causing dynamic wagging motion resulting in a release. Without illumination, premature release was almost negligible.

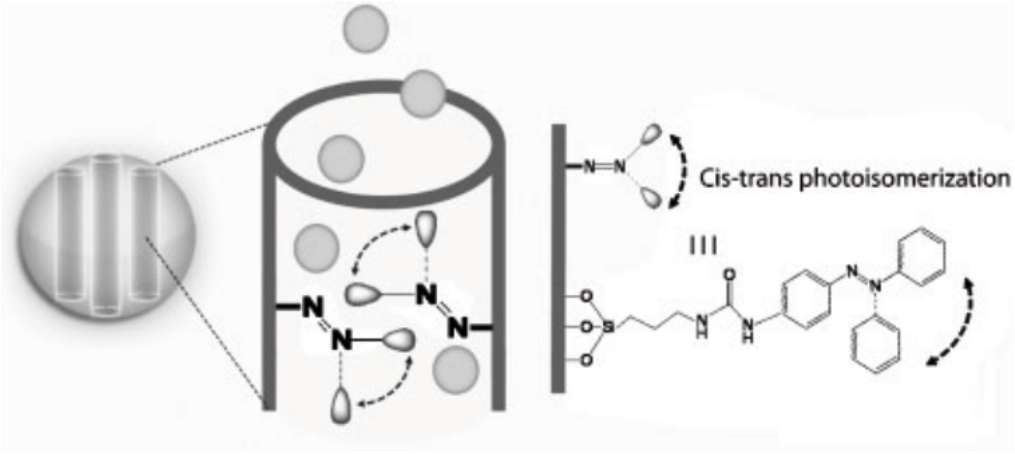

Figure 1.11: Schematic representation of the light driven nanoimpellers.[98]

1.5.3 Targeting of cancer cells

One of the biggest challenges in targeted drug delivery with nanoparticles is to achieve sufficiently high local drug concentrations in tumors, while sparing healthy tissue. In anticancer therapy, limited selectivity of cytostatins and cytotoxins towards tumor cells is responsible for many undesired side effects. The therapeutic index is determined by biodistribution, metabolism, and clearance of nanoparticulate drug delivery systems.[99] Nanoparticles have to pass different barriers before reaching the desired location (Figure 1.12).

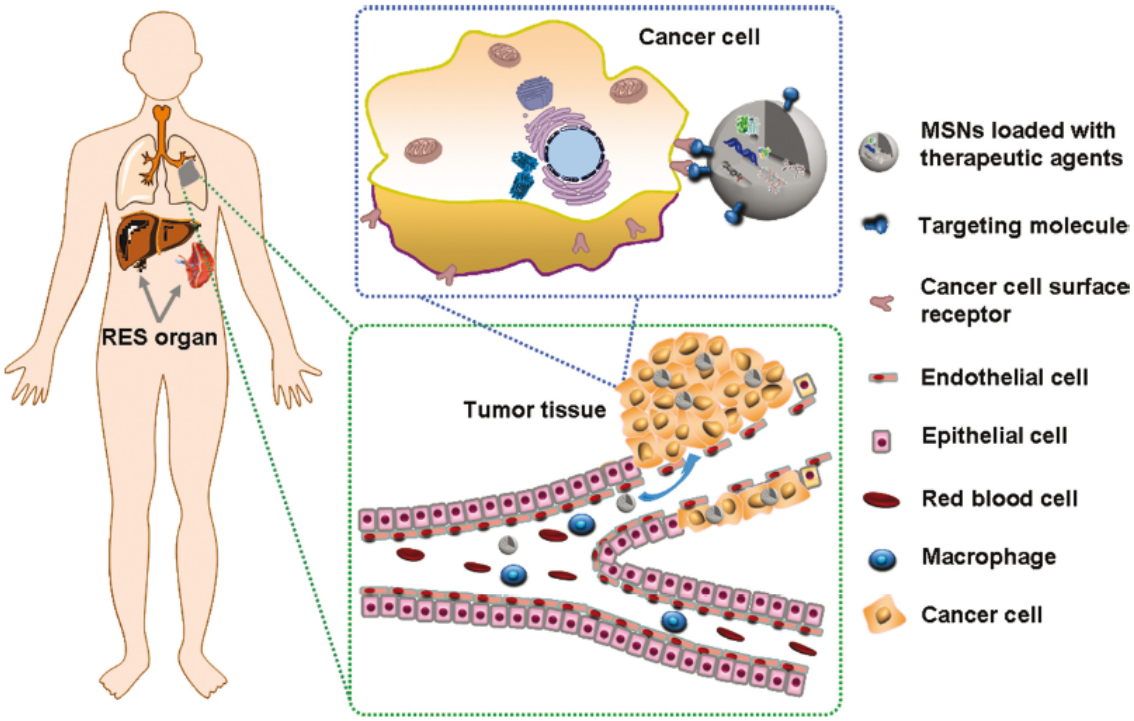

Figure 1.12: *In vivo* barriers encountered by nanometer-sized drug delivery systems after systemic administration for cancer therapy and the nanotechnology-based strategies developed for targeted cancer therapy.[99]

Precise understanding of these barriers is crucial for designing nanoparticles with the ability to bypass these barriers and reach cancer cells, as these barriers are highly efficient in removing foreign materials including nanoparticles from the body. Passive targeting relies on the abnormal vascular structure of tumor tissue, which results in substantial advantages for nanoparticulate drug delivery systems with sizes ranging from around 30 to 400 nm, and allows nanoparticles to accumulate in the interstitial tumor space.[100] Enhanced permeability and retention (EPR) describes passive accumulation of nanoparticles in tumor tissue. Despite the EPR effect, difficulties still exist for homogeneous distribution of nanoparticles in all regions of tumor tissue.[99] The limitations in EPR lead to the development of active targeting. Due to the high metabolic demands for rapid proliferation, cancer cells generally overexpress folate, transferrin, epidermal growth factor or $\alpha\nu\beta3$ receptors.[87,101–103] In this context, nanoparticles functionalized with specific antibodies, peptides, ligands, aptamers and oligonucleotides were developed to bind selectively to receptors

overexpressed on certain cancer cells (Figure 1.12). An efficient uptake of folic acid-modified nanoparticles compared with unfunctionalized ones was demonstrated by Linden *et al.*.[104] Others have reported successful targeting of the $\alpha\nu\beta3$ receptor with arginine-glycine-aspartate tripeptide (RGD) modified MSNs.

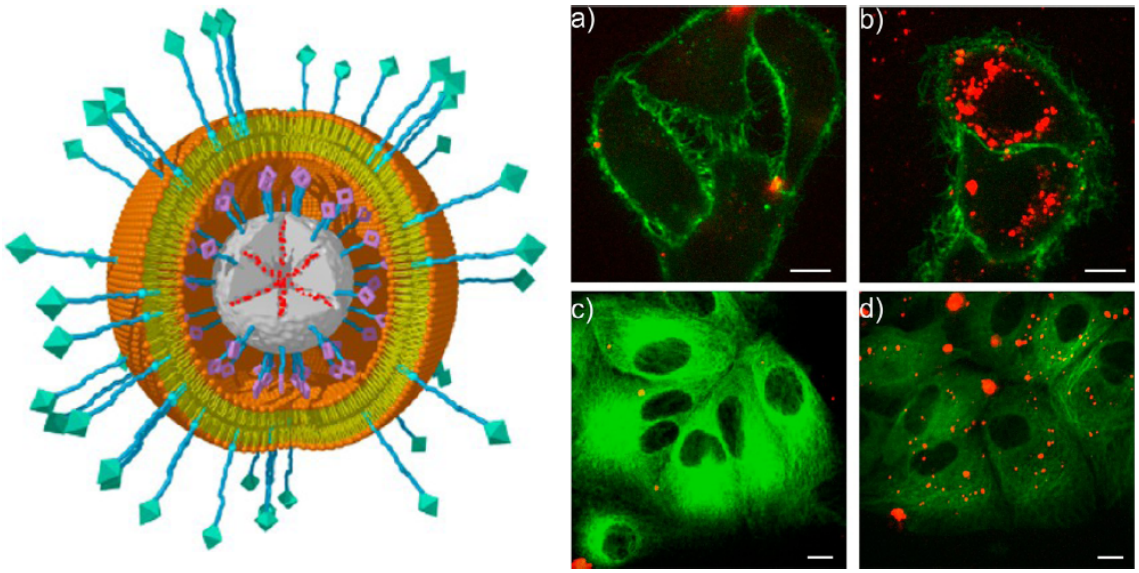

Figure 1.13: Left: Cartoon of the used delivery vehicle. Right: Unspecific and receptor-mediated endocytosis of particles with folic acid ligand (b) by KB cells and particles with EGF ligand (d) by HuH7 cells with GFP tagged tubulins (HuH7tub), respectively. Uptake of particles without targeting ligand is shown in a) and c).[88]

Recently our group together with the group of Prof. Bräuchle showed that MSNs coated with a lipid bilayer can serve as a versatile platform for the attachment of different targeting ligands (Figure 1.13).[88] Lipid functionalized folic acid and EGF ligands were introduced into the delivery vehicle *via* diffusion. A significantly enhanced uptake into cancer cells could be observed with live-cell imaging. Wagner *et al.* have shown the uptake and gene transfection efficiency in cells of DNA-polyplexes conjugated with EGF.[105]

1.6 Immobilization of proteins in mesoporous silica

In 1916, the first example of protein immobilization was reported. Nelson *et al.* showed that the activity of invertase can be retained after the attachment on char-

coal.[106] The main goals of immobilization are the enhancement of stability and the simplification of enzyme recovery and reusability at high activity levels. Therefore, many different immobilization techniques on numerous support materials have been investigated.[107–121] An important aspect for the selection of a suitable mesoporous support material for a specific protein involves the matching of the physicochemical properties of the protein and the support (Figure 1.14).[122,123] In an ideal case, the active center of a protein is directed away from the mesoporous surface, with sufficient mobility to retain its catalytic acitivity but without leaching from the support.

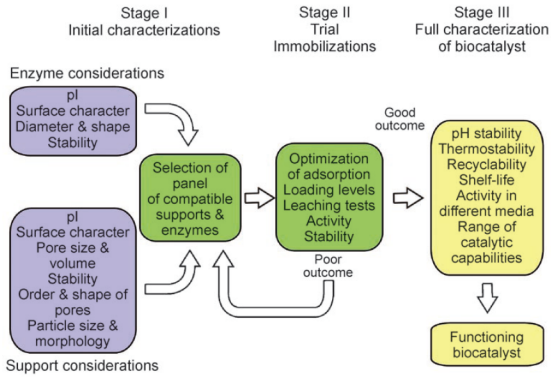

Figure 1.14: Important factors for the generation of a novel immobilized protein biocatalyst.[122]

1.6.1 Size relation of the mesopores and the protein

Proteins only have access to the inner surface of mesoporous supports if the hydrodynamic diameter of the protein is smaller than the pore opening of the mesoporous host. Otherwise proteins can only be adsorbed without further protection at the outer surface of the material. Diaz *et al.* showed that horseradish peroxidase (mean diameter ca. 4.6 nm) cannot be taken up by MCM-41 (pore diameter ca. 4 nm) as it is too large to fit into the pores.[124] In similar experiments 8 μmol per gram of cytochrome c could be adsorbed on MCM-41 with a pore diameter of 4.5 nm but with smaller pores in the range of 2.8 nm, only less than 1 μmol g^{-1} was obtained at same adsorption conditions.[125] These experiments show that matching the hydro-

dynamic diameter of the protein and the pore diameter is essential for obtaining high loadings. However, loading is also strongly influenced by the accessible pore volume and the specific surface area. The use of mesoporous silica for the immobilization of antibodies in biosensors is limited by the pore size, although Hu *et al.* showed the immobilization of an antibody fragment that showed good binding efficiencies for a strong neurotoxin from shellfish.[126] The direct entry of proteins in sufficiently large mesoporous structures still has to be proven by direct imaging of enzymes or proteins inside the pores.[127] Up to now, entering of proteins into pores has been indicated indirectly through higher loading capacities and enhanced stability compared with nonporous reference samples. For DNA, Cauda *et al.* were able to visualize directly the confined movement of a labeled DNA double strand in long-range ordered SBA-15 fibers with single molecule fluorescent microscopy.[128] Takahashi *et al.* reported that for enhanced activity in organic solvents and increased hydrothermal stability of horseradish peroxidase, it is mandatory to have similar diameters of pores and guest molecules.[129,130] Similar results regarding optimized fitting for enhanced stability were published by other research groups.[131–134] Small pore openings can reduce leakage of proteins which are not attached covalently to the host material. However there still has to be enough space to ensure diffusion of the substrate. A reduction of the diffusion ability would lead to a drop of catalytic activity.[132,135] Additionally, the hydrophobic and hydrophilic nature of the substrate contribute significantly to the activity of an immobilized enzyme.[125,132,134] Diffusion of a hydrophobic substrate can be slowed down in hydrophilic mesoporous silica structures. This problem can be reduced either by increasing the pore diameter or modification of the pore walls with hydrophobic residues. On the other hand, a hydrophilic substrate is able to diffuse easily through small pores which offer better stabilization for the immobilized enzyme.

1.6.2 Particle size and morphology

The pore volume of mesoporous supports after protein immobilization is often decreased by a larger extent than the corresponding volume occupied by the immobi-

lized protein.[136,137] Materials with shorter mesoporous channels (smaller particles) and similar pore volume show higher loading capacities (37 compared to 5 μmol per gram SBA-15). The reason for that is a lower amount of blocked pores.[138] As a consequence, the particle size and morphology need to be taken into account when comparing adsorption in mesoporous materials. These two attributes significantly influence adsorption isotherms, adsorption kinetics and specific activities of proteins on mesoporous materials.[132,138–142]

1.6.3 Stability of the mesoporous material

To ensure reusability of an immobilized enzyme, the support material has to be stable under working conditions. Degradation of the host material leads to a release of the enzyme and therefore to a loss in activity after recovery. If the host material is used as a release and rebind system, the mesoporous material has to maintain its structure so that the protein is able to diffuse in after the reaction.[143] It has been reported that SBA-materials are, due to their thicker walls, hydrothermally more stable than MCM-materials.[137,144,145] However, inconsistant reports exist concerning materials produced by different synthesis protocols. Ji *et al.* observed, similar to Katiyar *et al.*, that Al-MCM-41 is instable at pH-values above 9.[146,147] In contrast to these findings, Hernandez *et al.* reported the degradation of MCM-41 at pH-values of 7.4.[148] Other groups used specific synthesis protocols to enhance the hydrothermal stability of MCM-41 materials, e. g. zeolitic clusters were used as silicon dioxide source in combination with numerous surfactants.[132] Periodic mesoporous organosilicates with bridged amino-groups showed low stability at pH values between 4-10. Through variation of the surfactant under identical synthetic conditions, more stable materials were obtained in which chloroperoxidase could be immobilized and recovered without loss of activity.[149]

1.6.4 Isoelectric points of mesoporous silica and protein

The isoelectric point (IP) of a particle or protein corresponds to the specific pH-value at which the surface charge is zero. Below or above this pH-value, the protein

is either positively or negatively charged. It has been discussed that best adsorption behavior can be achieved in immobilization buffers with a pH below the IP of the protein and above the IP of the support material.[124] At pH-values below the IP of the protein, the enzyme will exhibit a net positive surface charge which favors interaction with the silica material that is negatively charged at pH > 3.[125,136] Simulations with cytochrome c and trypsin showed that proteins with similar IP can have different surface potentials at pH 7.[150] While compatible sizes and isoelectric points are necessary for successful immobilization, they do not automatically lead to adsorption.[126,151,152] Only low loading could be obtained for subtilisin, which is small enough to fit into the pores of mesoporous silica modified with cyano groups, even at appropriate pH-values.[136] Interactions between the two surfaces are influenced by the surface charge density and charge distribution of the enzyme. These aspects are not described accurately enough by the isoelectric point and need to be determined more precisely to understand interactions with the surface of the support material. The isoelectric point of mesoporous silica is often estimated to a value of approximately 2,[143,153,154] as found for amorphous silica.[155] For MCM-41 Deere *et al.* determined a value of 3.6, whereas for commercial silica and mesoporous silica templated with F127 isoelectric points of 2.9 and 2.8 were found, respectively.[136] Electrostatic interactions with proteins can further be tuned by the functionalization of pure mesoporous silica with organic functional groups.

1.6.5 Functional groups at the surfaces of mesoporous silica and proteins

Strong interactions between proteins and host materials can be obtained by complementary functionalization. Mesoporous silica has been modified with various different functionalities, which led to different loadings and activities depending on the way and amount of modification.[149,151,156] However, residual solvent molecules originating from the functionalization step can lead to a drop in activity. High degrees of modification can result in pore blocking or reduction of the pore diameter. Further functionalization of the pores after protein immobilization can enhance the

hydrophobicity or amphiphilicity of the support leading to better diffusion kinetics of the substrate and products.[127,157,158] Covalent linkage of amino-groups at the surface of the mesoporous support to amino-groups of the enzyme *via* glutaraldehyde can significantly improve stability, reduce leakage and therefore enable reusability. With this approach, many different enzymes like penicillin-G-acylase,[159,160] glucose oxidase,[161] α-amylase,[162] lipase,[163] glucose isomerase,[164] trypsin,[135] invertase,[165] and glucoamylase[165] have been covalently immobilized. 1-Ethyl-3-(3-dimethylaminopropyl)carbodiimide (EDC) was used to covalently attach chloroperoxidase[133,166] and α-L-arabinofuranosidase[141] *via* amide bond formation between the carboxylic acid groups of the enzyme and the amino-groups of the support material. Proteins can furthermore be attached by reaction of epoxy-modified pores with amino-groups of the protein, which was demonstrated for penicillin acylase.[167] Schlossbauer *et al.* reported on the covalent attachment of alkyne modified trypsin on azide functionalized SBA-15 *via* a "click chemistry" approach.[168] The enhanced rigidity of the enzyme resulting from covalent immobilization can lead to decreased activity as observed for penicillin acylase,[167] glucose isomerase[164] and trypsin.[168] Furthermore, the effect of metal ions in mesoporous silica on the adsorption behavior of proteins and enzymes has been investigated. Aluminum substituted mesoporous silica has been used to immobilize enzymes like cytochrome c,[132] bovine serum albumine,[146] lysozyme[137,145] and cytochrome P450.[148] Aburto *et al.* reported on improved loading of chloroperoxidase on SBA-16 impregnated with Cs^+.[133] The creation of weakly acidic centers through functionalization of MCM-48 with Co^{2+} leads to better loading of penicillin-G-acylase as shown by Xue *et al.*.[169]

1.6.6 Interactions between proteins and support

It is difficult to gain detailed information about interactions between a protein and its host material through loading experiments at specific conditions. In most cases at least the differentiation between covalent attachment and physical adsoption can be made. For explicit evaluation of the interactions of absorbed proteins with a support material such as hydophilic, hydrophobic or electrostatic interactions, different

experiments have to be performed. Such experiments include the use of desorptive agents like polyethylene glycol, methanol and ammonium sulfate, or the change of the ionic strength of the immobilizaion buffer.[136,152,170] Depending on the host material, cytochrome c shows distinct adsorption behavior. Diaz *et al.* reported on hydrophilic interactions between cytochrome c and MCM-41. Investigations by Deere *et al.* with desorptive agents revealed that electrostatic interactions between cytochrome c and cyano-modified mesoporous silica play the most important role, whereas with silica gel hydrophobic interactions are the most prominent.[124,136] Other studies with cytochrome c on SBA-15 showed electrostatic, with ethylene bridged periodic mesoporous organosilica hydrophobic/hydrophilic interactions.[123] Highest loading capacities were found for pH values close to the point of zero charge of the protein. At this pH, repelling forces between the protein molecules are minimized and therefore loading is enhanced. Similar observations have been made for the adsorption of lysozyme on MCM-41 and SBA-15.[137,147]

1.6.7 Preservation of the enzymatic activity after immobilization

The activity of an immobilized enzyme can be influenced by the surface of mesoporous materials.[135,160] It is difficult to obtain host-guest interactions that are on the one hand strong enough to prevent leakage but on the other hand weak enough to maintain enzyme flexibility and as a consequence thereof its activity. Evaluation and interpretation of the activity of a leaking enzyme is in most cases not feasible. Different strategies have been developed to prevent leakage, such as cross-linking of the enzymes inside the pores (cross-linked enzyme aggregates, CLEAs) or covalent attachment to the pores.[132,168,171,172] For α-chymotrypsin and mucor-javanicus-lipase, cross-linking led to a material which showed enhanced stability against shaking and degradation by trypsin.[132,171] After adsorption on MCM-48 and cross-linking, papain showed only 70% residual activity. However, enhanced temperature- and pH-stability could be observed. The system could be recycled for 12 days without further loss of activity.[132] Deere *et al.* reported on enhanced

activity of cytochrome c after immobilization on mesoporous materials compared to the free enzyme in solution, which is due to the high-spin-Fe^{3+} centers present in the immobilized state.[136,173] Highest activities were obtained for low loadings of cytochrome c, because access to the pores can be hindered through high loadings or multilayer adsorption. Enhanced protein activity has also been observed for immobilized glucose oxidase,[132,152] microperoxidase-11[174] and candida-antarctica-lipase (CAL).[175] Altogether, enzyme activity depends on the enzymes' nature, the mesoporous support and the way of immobilization. Trypsin showed, after covalent immobilization on SBA-15, only 17 % residual activity compared to the free enzyme.[168] Chloroperoxidase immobilized on mesoporous cellular foam showed only half the activity of the free enzyme,[153] whereas covalent attachment to SBA-16 resulted in enhanced activity compared to the physically adsorbed enzyme.[133] A loss in activity was found for penicillin acylase adsorbed on differently functionalized SBA-15. Only vinyl-functionalized SBA-15 showed twice the activity as free penicillin acylase.[159] For some proteins, e. g. α-chymotrypsin and aldolase-I-antibody, enantioselectivity was maintained after immobilization.[131,176] Every system containing proteins on mesoporous supports shows different bahavior so that the relative activity of each biocatalyst needs to be determined.

1.6.8 Reusability and enhanced stability of the biocatalyst

In biocatalysis with composite materials it is mandatory to immobilize the protein permanently on the support material. Enzymes washed out of the support can hardly be separated from the reaction mixture. Immobilization inside mesopores can increase the protein stability against heat, extreme pH values, denaturing agents and organic solvents. Zheng *et al.* reported on the enhanced stability against heat under ideal conditions (pH 8 in the presence of CTAB) for pseudomonas-cepacia-lipase.[177] The loss in activity of 50 % after 8 cycles was explained by washing out of the enzyme and incomplete recovery. α-chymotrypsin immobilized in MCM-41 could be used over 100 cycles within one week.[131] A possibility to prevent leakage is the reduction of the pore openings by silanization after protein adsorption.[124,178] However,

this process can lead to deactivation of the protein. As already mentioned for enzyme aggregates in subsection 1.6.7, immobilization can enhance storage properties. Trypsin immobilized on MCM-41 remained active even after storage at 25 °C for one week, whereas free trypsin was completely inactive.[124] For the use as biosensors with immobilized proteins, storage stability is very crucial. Immobilized antibody fragments preserved their binding affinity for 42 days, as reported by Hu *et al.*.[126] Covalently attached enzymes, even if they show reduced activity, can be the catalyst of choice due to the facile recovery, which makes them promising candidates for several applications.

1.7 Nanoparticles for biosensing applications

Due to their unique properties, nanoclusters, nanoparticles and nanocomposites have become very popular objects of study and also tools in research in many laboratories.[179] Since nanoparticles feature sizes similar to biological macromolecules, they have the ability to provide information about the studied system (e. g. living cells) in the form of fluorescent emission or the release of certain compounds. Recently, nanocomposites have found many practical applications, e. g., clinical diagnostics,[180] food safety control,[181] environmental monitoring[182] and detection of biological warfare agents.[183] To realize sensing of special analytes, nanoparticles should possess the ability to specifically recognize their targets and translate the recognition into detectable signals. As already discussed in the sections 1.5 and 1.6, mesoporous silica materials are able to combine both requirements: targeting and the production of coloured compounds by enzymatic reactions. A very popular approach to realise nano-bioconjugation uses the biotin-avidin (or streptavidin) interaction as a universal linkage that connects the desired recognition site to the nanoparticle.[179,184] Furthermore, nanostructures can be functionalized with enzymes, antibodies, affinity proteins and cell receptor specific ligands.[185] Among those, the high specificity of antibodies makes them - in combination with nanoparticles - a very interesting tool for immunoassays.

1.7.1 Immunoassays

If analytes cannot be detected directly *via* substrate-specific characteristics (e.g. extinction coefficient, enzymatic activity,...), or the concentration of the analyte excludes other procedures, immunoassays are usually used. For the use of immunoassays the chemical structure of the analyte has to be known in order to be able to produce specific antibodies, or a specific natural antibody has to be known.[186] Yalow and Berson were the first scientists reporting on the development of immunoassays in the 1950s.[187] Immunoassays became considerably simpler to perform and more popular in the late 1960s, when it was shown that enzymes can be chemically linked to antibodies. Today, a variety of different labels for detection of antibodies and antigens are known. The most prominet labels are enzymes, radioactive isotopes, DNA reporters, electroluminescent tags and fluorophores including nanoparticles among others.[188] Furthermore, label-free immunoassays have been reported that are based on the fact that changes in resistance of an electrode can occur upon binding of antibodies or antigens.[189] Antibodies (also known as immunoglobulin) are large Y-shaped proteins of the immune system that are able to recognize unique parts of a foreign target, called an antigen.[190] They consist of four polypeptide chains: two identical *heavy chains* and two identical *light chains* connected by disulfide bridges (Figure 1.15).

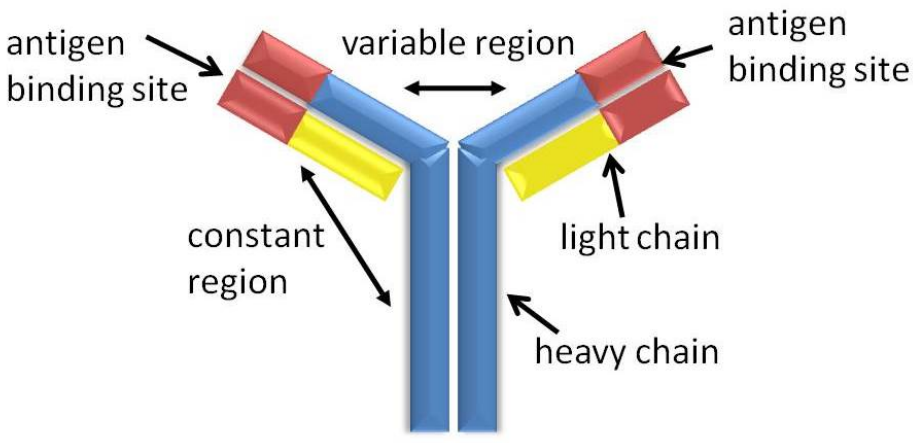

Figure 1.15: Schematic representation of an antibody.[191]

Each chain is composed of structural domains called immunoglobulin (Ig) domains which exhibit a characteristic immunoglobulin fold in which two beta sheets create a ”sandwich" shape that is held together by interactions between conserved cysteins and charged amino acids. The region of an antibody that binds to the antigen is called antigen-binding fragment, which is composed of one constant and one variable domain of each of the heavy and the light chain. These domains shape the paratope and bind the epitope of the corresponding antigen.[192] This specific binding behavior can be used to design analytic assays, of which the enzyme-linked-immunosorbent-assay (ELISA) and the lateral-flow-immunoassay (LFIA) will be further described in the following sections.

1.7.2 Enzyme-linked-immunosorbent-assay (ELISA)

Before the development of the ELISA technique, radioimmunoassays were the only option for conducting an immunoassay. The potential risk of using radioactive labels led to the attachment of enzymes onto the antibodies to enable optical read-out.[193,194] Today, different approaches can be used for ELISA, indirect, competitive and the most used sandwich type (Figure 1.16).

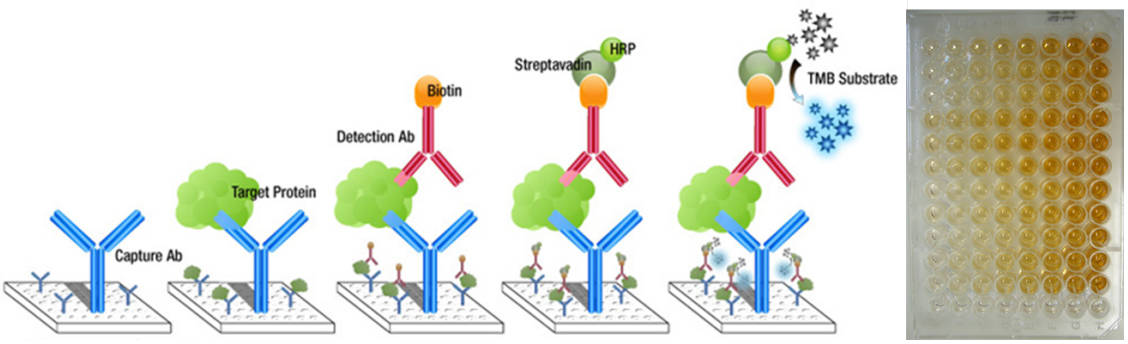

Figure 1.16: Left: Scheme of a sandwich ELISA. Ab = antibody, HRP = horseradish peroxidase, TMB = tetramethylbenzidine. Right: Image of a multiwell plate ready for optical read-out.[195,196]

First, a capture antibody specific to the analyte of interest is immobilized on a solid phase (e. g. microtiter plate). Subsequently, all nonspecific binding sites on the surface are blocked before the antigen-containing sample is applied to the plate. The

analyte is captured by the immobilized antibody and detected by a second analyte-specific antibody. Hence, the antigen is stuck between two antibodies forming a "sandwich"). The second antibody is bearing either an enzyme (e. g. horseradish peroxidase) or a label that allows to attach further molecules (e. g. biotin) which enable the translatation of the concentration of the antigen into an optical signal. To determine the concentration, calibration curves have to be recorded. ELISA is limited to large molecules such as proteins, since the analyte has to feature two epitopes.[197]

1.7.3 Lateral-flow-immunoassay (LFIA)

Lateral-flow tests represent simple devices which report on the presence or absence of an analyte. Based on the technique developed for ELISA, LFIA uses immobilized antibodies that capture and detect the analyte. One major difference compared to ELISA is that a liquid sample has to move along a strip made of different membranes. The LFIA is assembled from different components including (Figure1.17):[197]

- Sample pad
- Conjugate pad
- Reaction membrane
- Absorbent pad
- Backing material

The assay has two lines (test and control) that appear when a positive sample is added to the sample pad. The test line indicates that an antibody-coated label has bound to the antigen captured by the antibody immobilized on the nitrocellulose membrane. First, the sample is added to the sample pad and starts to flow through the membrane due to capillary forces. The analyte molecules move to the second membrane (conjugate pad) where particles containing antibodies specific for

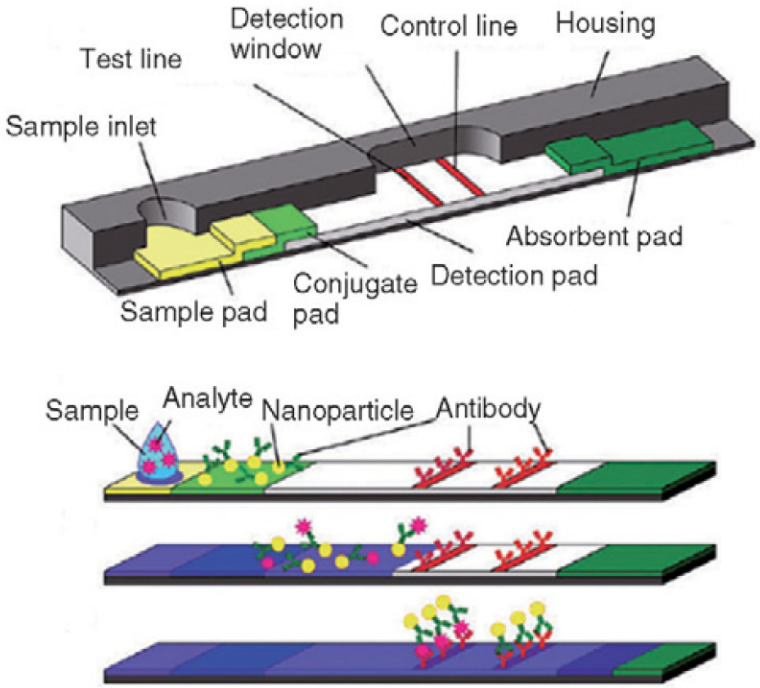

Figure 1.17: Schematic of a lateral flow strip (upper part) and lateral flow immunoassay (LFIA) based on a sandwich format (lower part).[198]

the analyte are deposited. The analyte interacts with an antibody-coated particle, producing the analyte-antibody-particle-complex. The complexes flow into the reaction membrane, where antibodies specific to the antigen (test line) and to the antibody from the particles (control line) are immobilized in line format. In the first line, the antigen-antibody-particle complexes are trapped by atigen-antibody interactions and produce a signal which is characteristic for the particles. Most of the commercial tests are based on gold nanoparticles, developing a red line as a positive result. The antibody-coated particles that do not bind to the analyte are trapped in the control line by antibody-antibody interactions. The excess of liquid is absorbed in the absorbent pad.[197] The success of the analysis can be read out directly. If two lines appear in the read-out window, the analyte was present in the sample. A negative result is obtained if only the control line appears coloured. In the case where no line is observable, the test failed.

Bibliography

[1] Beck, J. S., Vartuli, J. C., Roth, W. J., Leonowicz, M. E., Kresge, C. T., Schmitt, K. D., Chu, C. T. W., Olson, D. H., and Sheppard, E. W. *Journal of the American Chemical Society* **114**, 10834–10843 (1992).

[2] of Symbols, I. M. and Terminology, Appendix 2, P. . *Pure Applied Chemistry* **31**, 578 (1972).

[3] Yu, M., Li, S., Falconer, J. L., and Noble, R. D. *Microporous and Mesoporous Materials* **110**(2-3), 579 – 582 (2008).

[4] Nijkamp, M., Raaymakers, J., van Dillen, A., and de Jong, K. *Applied Physics A* **72**(5), 619–623 (2001).

[5] Kazansky, V., Borovkov, V., Serich, A., and Karge, H. *Microporous and Mesoporous Materials* **22**(1-3), 251 – 259 (1998).

[6] Tchernev, D. I. *Reviews in Mineralogy and Geochemistry* **45**(1), 589–617 (2001).

[7] Caro, J. *Microporous and Mesoporous Materials* **125**(1-2), 79 – 84 (2009).

[8] Calzaferri, G., Bruhwiler, D., Megelski, S., Pfenniger, M., Pauchard, M., Hennessy, B., Maas, H., Devaux, A., and Graf, U. *Solid State Sciences* **2**(4), 421 – 447 (2000).

[9] Schäf, O., Ghobarkar, H., and Kanuth, P. *Enzyclopedia of Sensors* **10**, 491 – 500 (2006).

[10] Xu, X., Wang, J., and Long, Y. *Sensors* **6**(12), 1751–1764 (2006).

[11] Ozin, G. A., Kuperman, A., and Stein, A. *Angewandte Chemie International Edition in English* **28**(3), 359–376 (1989).

[12] Liu, P.-H., Thebault, P., Guenoun, P., and Daillant, J. *Macromolecules* **42**(24), 9609–9612 (2009).

[13] Thebault, P., Niedermayer, S., Landis, S., Chaix, N., Guenoun, P., Daillant, J., Man, X., Andelman, D., and Orland, H. *Advanced Materials* **24**(15), 1952–1955 (2012).

[14] Platas-Iglesias, C., Vander Elst, L., Zhou, W., Muller, R. N., Geraldes, C. F. G. C., Maschmeyer, T., and Peters, J. A. *Chemistry - A European Journal* **8**(22), 5121–5131 (2002).

[15] Vallet-Regi, M., Balas, F., Colilla, M., and Manzano, M. *Solid State Sciences* **9**(9), 768 – 776 (2007).

[16] Wan, Y. and Zhao. *Chemical Reviews* **107**(7), 2821–2860 (2007).

[17] Kresge, C. T., Leonowicz, M. E., Roth, W. J., Vartuli, J. C., and Beck, J. S. *Nature* **359**, 710–712 (1992).

[18] Lopez, T., Ortiz, E., Alexander-Katz, R., Basaldella, E., and Bokhimi, X. *Nanomedicine* **5**, 170–177 (2009).

[19] Wang, Y. and Caruso, F. *Chemistry of Materials* **17**(5), 953–961 (2005).

[20] Galarneau, A., Phuoc, L. T., Falcimaigne, A., Renard, G., and Fajula, F. In *Recent Progress in Mesostructured Materials Proceedings of the 5th International Mesostructured Materials Symposium (IMMS2006),* Dongyuan Zhao, Shilun Qiu, Y. T. and Yu, C., editors, volume 165 of *Studies in Surface Science and Catalysis*, 637 – 641. Elsevier (2007).

[21] Ke, J., Su, W., Howdle, S. M., George, M. W., Cook, D., Perdjon-Abel, M., Bartlett, P. N., Zhang, W., Cheng, F., Levason, W., Reid, G., Hyde, J.,

Wilson, J., Smith, D. C., Mallik, K., and Sazio, P. *Proceedings of the National Academy of Sciences* **106**(35), 14768–14772 (2009).

[22] Bao, R., Jiao, K., He, H., Zhuang, J., and Yue, B. In *Recent Progress in Mesostructured Materials Proceedings of the 5th International Mesostructured Materials Symposium (IMMS2006),* Dongyuan Zhao, Shilun Qiu, Y. T. and Yu, C., editors, volume 165 of *Studies in Surface Science and Catalysis*, 267 – 270. Elsevier (2007).

[23] Eliseev, A., Gorozhankin, D., Zaitsev, D., Lukashin, A., Knotko, A., Tretyakov, Y., and Goernert, P. *Journal of Magnetism and Magnetic Materials* **290-291**, 106 – 109 (2005).

[24] Hoskins, B. F. and Robson, R. *Journal of the American Chemical Society* **111**(15), 5962–5964 (1989).

[25] Kitagawa, S., Kitaura, R., and Noro, S.-i. *Angewandte Chemie International Edition* **43**(18), 2334–2375 (2004).

[26] Ferey, G. *Chem. Soc. Rev.* **37**, 191–214 (2008).

[27] Yaghi, O. M., Li, G., and Li, H. *Nature* **378**, 703 (1995).

[28] Rao, C. N. R., Natarajan, S., and Vaidhyanathan, R. *Angewandte Chemie International Edition* **43**(12), 1466–1496 (2004).

[29] Ferey, G., Mellot-Draznieks, C., Serre, C., Millange, F., Dutour, J., Surble, S., and Margiolaki, I. *Science* **309**(5743), 2040–2042 (2005).

[30] Ferey, G., Serre, C., Mellot-Draznieks, C., Millange, F., Surble, S., Dutour, J., and Margiolaki, I. *Angewandte Chemie International Edition* **43**(46), 6296–6301 (2004).

[31] Deng, H., Grunder, S., Cordova, K. E., Valente, C., Furukawa, H., Hmadeh, M., Gándara, F., Whalley, A. C., Liu, Z., Asahina, S., Kazumori, H., OŠKeeffe,

M., Terasaki, O., Stoddart, J. F., and Yaghi, O. M. *Science* **336**(6084), 1018–1023 (2012).

[32] Cote, A. P., Benin, A. I., Ockwig, N. W., O'Keeffe, M., Matzger, A. J., and Yaghi, O. M. *Science* **310**(5751), 1166–1170 (2005).

[33] Dogru, M., Handloser, M., Auras, F., Kunz, T., Medina, D., Hartschuh, A., Knochel, P., and Bein, T. *Angewandte Chemie International Edition* **52**(10), 2920–2924 (2013).

[34] Huo, Q., Margolese, D. I., Ciesla, U., Feng, P., Grier, T. E., Sieger, P., Leon, R., Petroff, P. M., Schueth, F., and Stucky, G. D. *Nature* **368**, 317–321 (1994).

[35] Huo, Q., Margolese, D. I., Ciesla, U., Demuth, D. G., Feng, P., Gier, T. E., Sieger, P., Firouzi, A., and Chmelka, B. F. a. *Chemistry of Materials* **6**(8), 1176–1191 (1994).

[36] Chen, C.-Y., Burkett, S. L., Li, H.-X., and Davis, M. E. *Microporous Materials* **2**(1), 27 – 34 (1993).

[37] Monnier, A., Schüth, F., Huo, Q., Kumar, D., Margolese, D., Maxwell, R. S., Stucky, G. D., Krishnamurty, M., Petroff, P., Firouzi, A., Janicke, M., and Chmelka, B. F. *Science* **261**(5126), 1299–1303 (1993).

[38] Attard, G. S., Glyde, J. C., and Goeltner, G. *Nature* **378**, 366–368 (1995).

[39] Yang, P., Zhao, D., Margolese, D. I., Bradley, F. C., and Stucky, G. D. *Nature* **396**, 152–155 (1998).

[40] Lu, Y., Ganguli, R., Drewien, C. A., Anderson, M. T., Brinker, J. C., Gong, W., Guo, Y., Soyez, H., Dunn, B., Huang, M. H., and Zink, J. I. *Nature* **389**, 364–368 (1997).

[41] Wu, S.-H., Mou, C.-Y., and Lin, H.-P. *Chem. Soc. Rev.* **42**, 3862–3875 (2013).

[42] Lu, Y., Fan, H., Stump, A., Ward, T. L., Rieker, T., and Brinker. *Nature* **398**, 223–226 (1999).

[43] Grün, M., Lauer, I., and Unger, K. K. *Advanced Materials* **9**(3), 254–257 (1997).

[44] Cai, Q., Luo, Z.-S., Pang, W.-Q., Fan, Y.-W., Chen, X.-H., and Cui, F.-Z. *Chemistry of Materials* **13**(2), 258–263 (2001).

[45] Fowler, C. E., Khushalani, D., Lebeau, B., and Mann, S. *Advanced Materials* **13**(9), 649–652 (2001).

[46] Nooney, R. I., Thirunavukkarasu, D., Chen, Y., Josephs, R., and Ostafin, A. E. *Chemistry of Materials* **14**(11), 4721–4728 (2002).

[47] Nakamura, T., Mizutani, M., Nozaki, H., Suzuki, N., and Yano, K. *The Journal of Physical Chemistry C* **111**(3), 1093–1100 (2007).

[48] Lin, Y.-S., Tsai, C.-P., Huang, H.-Y., Kuo, C.-T., Hung, Y., Huang, D.-M., Chen, Y.-C., and Mou, C.-Y. *Chemistry of Materials* **17**(18), 4570–4573 (2005).

[49] Lu, F., Wu, S.-H., Hung, Y., and Mou, C.-Y. *Small* **5**(12), 1408–1413 (2009).

[50] Ikari, K., Suzuki, K., and Imai, H. *Langmuir* **22**(2), 802–806 (2006).

[51] Lin, Y.-S. and Haynes, C. L. *Chemistry of Materials* **21**(17), 3979–3986 (2009).

[52] Yokoi, T., Sakamoto, Y., Terasaki, O., Kubota, Y., Okubo, T., and Tatsumi, T. *Journal of the American Chemical Society* **128**(42), 13664–13665 (2006).

[53] Möller, K., Kobler, J., and Bein, T. *Advanced Functional Materials* **17**(4), 605–612 (2007).

[54] Tarn, D., Ashley, C. E., Xue, M., Carnes, E. C., Zink, J. I., and Brinker, C. J. *Accounts of Chemical Research* **46**(3), 792–801 (2013).

[55] Li, Z., Nyalosaso, J. L., Hwang, A. A., Ferris, D. P., Yang, S., Derrien, G., Charnay, C., Durand, J.-O., and Zink, J. I. *The Journal of Physical Chemistry C* **115**(40), 19496–19506 (2011).

[56] Kecht, J., Schlossbauer, A., and Bein, T. *Chemistry of Materials* **20**(23), 7207–7214 (2008).

[57] Angloher, S., Kecht, J., and Bein, T. *Chemistry of Materials* **19**(14), 3568–3574 (2007).

[58] Angloher, S., Kecht, J., and Bein, T. *Chemistry of Materials* **19**(23), 5797–5802 (2007).

[59] Vallet-Regi, M. *Chemistry - A European Journal* **12**(23), 5934–5943 (2006).

[60] Kim, H.-J., Matsuda, H., Zhou, H., and Honma, I. *Advanced Materials* **18**(23), 3083–3088 (2006).

[61] Zhao, Y., Trewyn, B. G., Slowing, I. I., and Lin, V. S.-Y. *Journal of the American Chemical Society* **131**(24), 8398–8400 (2009).

[62] Moulari, B., Pertuit, D., Pellequer, Y., and Lamprecht, A. *Biomaterials* **29**(34), 4554 – 4560 (2008).

[63] Lu, J., Liong, M., Li, Z., Zink, J. I., and Tamanoi, F. *Small* **6**(16), 1794–1805 (2010).

[64] `http://apps.webofknowledge.com/CitationReport.do?product=UA&search_mode=CitationReport&SID=T2ZFFTx6Fbiwci5gceL&page=1&cr_pqid=2&viewType=summary`.

[65] Radin, S., El-Bassyouni, G., Vresilovic, E. J., Schepers, E., and Ducheyne, P. *Biomaterials* **26**(9), 1043 – 1052 (2005).

[66] Chia, S., Urano, J., Tamanoi, F., Dunn, B., and Zink, J. I. *Journal of the American Chemical Society* **122**(27), 6488–6489 (2000).

[67] Kortesuo, P., Ahola, M., Karlsson, S., Kangasniemi, I., Yli-Urpo, A., and Kiesvaara, J. *Biomaterials* **21**(2), 193 – 198 (2000).

[68] Coti, K. K., Belowich, M. E., Liong, M., Ambrogio, M. W., Lau, Y. A., Khatib, H. A., Zink, J. I., Khashab, N. M., and Stoddart, J. F. *Nanoscale* **1**, 16–39 (2009).

[69] Vallet-Regi, M., Balas, F., and Arcos, D. *Angewandte Chemie International Edition* **46**(40), 7548–7558 (2007).

[70] Trewyn, B. G., Slowing, I. I., Giri, S., Chen, H.-T., and Lin, V. S.-Y. *Accounts of Chemical Research* **40**(9), 846–853 (2007).

[71] Argyo, C., Weiss, V., Bräuchle, C., and Bein, T. *Chemistry of Materials* **accepted** (2013).

[72] Giri, S., Trewyn, B. G., Stellmaker, M. P., and Lin, V. S.-Y. *Angewandte Chemie International Edition* **44**(32), 5038–5044 (2005).

[73] Patel, K., Angelos, S., Dichtel, W. R., Coskun, A., Yang, Y.-W., Zink, J. I., and Stoddart, J. F. *Journal of the American Chemical Society* **130**(8), 2382–2383 (2008).

[74] Schlossbauer, A., Kecht, J., and Bein, T. *Angewandte Chemie International Edition* **48**(17), 3092–3095 (2009).

[75] Chen, L., Wen, Y., Su, B., Di, J., Song, Y., and Jiang, L. *J. Mater. Chem.* **21**, 13811–13816 (2011).

[76] Schlossbauer, A., Warncke, S., Gramlich, P., Kecht, J., Manetto, A., Carell, T., and Bein, T. *Angewandte Chemie International Edition* **49**(28), 4734–4737 (2010).

[77] Lai, C.-Y., Trewyn, B. G., Jeftinija, D. M., Jeftinija, K., Xu, S., Jeftinija, S., and Lin, V. S.-Y. *Journal of the American Chemical Society* **125**(15), 4451–4459 (2003).

[78] Ferris, D. P., Zhao, Y.-L., Khashab, N. M., Khatib, H. A., Stoddart, J. F., and Zink, J. I. *Journal of the American Chemical Society* **131**(5), 1686–1688 (2009).

[79] Vivero-Escoto, J. L., Slowing, I. I., Wu, C.-W., and Lin, V. S.-Y. *Journal of the American Chemical Society* **131**(10), 3462–3463 (2009).

[80] Nawal, K. M., Masahiro, F., and Yuko, T. *Nature* **421**, 350–353 (2003).

[81] Cauda, V., Argyo, C., Schlossbauer, A., and Bein, T. *J. Mater. Chem.* **20**, 4305–4311 (2010).

[82] Angelos, S., Yang, Y.-W., Patel, K., Stoddart, J. F., and Zink, J. I. *Angewandte Chemie International Edition* **47**(12), 2222–2226 (2008).

[83] Angelos, S., Khashab, N. M., Yang, Y.-W., Trabolsi, A., Khatib, H. A., Stoddart, J. F., and Zink, J. I. *Journal of the American Chemical Society* **131**(36), 12912–12914 (2009).

[84] Liu, J., Jiang, X., Ashley, C., and Brinker, C. J. *Journal of the American Chemical Society* **131**(22), 7567–7569 (2009).

[85] Ashley, C. E., Carnes, E. C., Phillips, G. K., Padilla, D., Durfee, P. N., Brown, P. A., Hanna, T. N., Liu, J., Phillips, B., Carter, M. B., Carrol, N. J., Jiang, X., Dunphy, D. R., Willman, C. L., Petsev, D. N., Evans, D. G., Parikh, A. N., Chackerian, B., Wharton, W., Peabody, D. S., and Brinker, C. J. *Nature Materials* **10**, 389–397 (2011).

[86] Epler, K., Padilla, D., Phillips, G., Crowder, P., Castillo, R., Wilkinson, D., Wilkinson, B., Burgard, C., Kalinich, R., Townson, J., Chackerian, B., Willman, C., Peabody, D., Wharton, W., Brinker, C. J., Ashley, C., and Carnes, E. *Advanced Healthcare Materials* **1**(3), 348–353 (2012).

[87] Schlossbauer, A., Sauer, A. M., Cauda, V., Schmidt, A., Engelke, H., Rothbauer, U., Zolghadr, K., Leonhardt, H., Bräuchle, C., and Bein, T. *Advanced Healthcare Materials* **1**(3), 316–320 (2012).

[88] Mackowiak, S. A., Schmidt, A., Weiss, V., Argyo, C., von Schirnding, C., Bein, T., and Bräuchle, C. *Nano Letters* **13**(6), 2576–2583 (2013).

[89] You, Y.-Z., Kalebaila, K. K., Brock, S. L., and , D. O. *Chemistry of Materials* **20**(10), 3354–3359 (2008).

[90] Fu, Q., Rao, G., Ista, L., Wu, Y., Andrzejewski, B., Sklar, L., Ward, T., and Lopez, G. *Advanced Materials* **15**(15), 1262–1266 (2003).

[91] Fu, Q., Rama Rao, G. V., Ward, T. L., Lu, Y., and Lopez, G. P. *Langmuir* **23**(1), 170–174 (2007).

[92] Liu, R., Zhao, X., Wu, T., and Feng, P. *Journal of the American Chemical Society* **130**(44), 14418–14419 (2008).

[93] Liu, R., Liao, P., Liu, J., and Feng, P. *Langmuir* **27**(6), 3095–3099 (2011).

[94] Mortera, R., Vivero-Escoto, J., Slowing, I. I., Garrone, E., Onida, B., and Lin, V. S.-Y. *Chem. Commun.* , 3219–3221 (2009).

[95] Sauer, A. M., Schlossbauer, A., Ruthardt, N., Cauda, V., Bein, T., and Bräuchle, C. *Nano Letters* **10**(9), 3684–3691 (2010).

[96] Schlossbauer, A., Dohmen, C., Schaffert, D., Wagner, E., and Bein, T. *Angewandte Chemie International Edition* **50**(30), 6828–6830 (2011).

[97] Gao, C., Zheng, H., Xing, L., Shu, M., and Che, S. *Chemistry of Materials* **22**(19), 5437–5444 (2010).

[98] Lu, J., Choi, E., Tamanoi, F., and Zink, J. I. *Small* **4**(4), 421–426 (2008).

[99] Tang, F., Li, L., and Chen, D. *Advanced Materials* **24**(12), 1504–1534 (2012).

[100] Vaupel, P., Kallinowski, F., and Okunieff, P. *Cancer Research* **49**(23), 6449–6465 (1989).

[101] Zhu, J., Tang, J., Zhao, L., Zhou, X., Wang, Y., and Yu, C. *Small* **6**(2), 276–282 (2010).

[102] Sun, W., Fang, N., Trewyn, B., Tsunoda, M., Slowing, I., Lin, V., and Yeung, E. *Analytical and Bioanalytical Chemistry* **391**(6), 2119–2125 (2008).

[103] Varkouhi, A. K., Scholte, M., Storm, G., and Haisma, H. J. *Journal of Controlled Release* **151**(3), 220 – 228 (2011).

[104] Rosenholm, J. M., Meinander, A., Peuhu, E., Niemi, R., Eriksson, J. E., Sahlgren, C., and Linden, M. *ACS Nano* **3**(1), 197–206 (2009).

[105] Kloeckner, J., Boeckle, S., Persson, D., Roedl, W., Ogris, M., Berg, K., and Wagner, E. *Journal of Controlled Release* **116**(2), 115 – 122 (2006).

[106] Nelson, J. M. and Griffin, E. G. *Journal of the American Chemical Society* **38**, 1109–1115 (1916).

[107] Sheldon, R. A. *Advanced Synthesis & Catalysis* **349**, 1289–1307 (2007).

[108] Yiu, H. H. P. and Wright, P. A. *Journal of Materials Chemistry* **15**, 3690–3700 (2005).

[109] Hartmann, M. *Chemistry of Materials* **17**, 4577–4593 (2005).

[110] Kim, J., Grate, J. W., and Wang, P. *Chemical Engineering Science* **61**, 1017–1026 (2006).

[111] Zhao, X. S., Bao, X. Y., Guo, W., and Lee, F. Y. *Materials Today* **9**, 32–39 (2006).

[112] Clark, J. H., Macquarrie, D. J., and Tavener, S. J. *Dalton Transactions* **35**, 4297–4309 (2006).

[113] Vinu, A., Miyahara, M., and Ariga, K. *Journal of Nanoscience and Nanotechnology* **6**, 1510–1532 (2006).

[114] Gill, I. and Ballesteros, A. *Journal of the American Chemical Society* **120**, 8587–8598 (1998).

[115] Brennan, J. D. *Accounts of Chemical Research* **40**, 827–835 (2007).

[116] Yi, Y. Y., Kermasha, S., L'Hocine, L., and Neufeld, R. *Journal of Molecular Catalysis B-enzymatic* **19**, 1381–1177 (2002).

[117] Lee, E. S., Kwon, M. J., Lee, H., and Kim, J. J. *International Journal of Pharmaceutics* **331**, 27–37 (2007).

[118] WEETALL, H. H. *Science* **166**, 615 (1969).

[119] Mureseanu, M., Galarneau, A., Renard, G., and Fajula, F. *Langmuir* **21**, 4648–4655 (2005).

[120] Blin, J. L., Gerardin, C., Carteret, C., Rodehuser, L., Selve, C., and Stebe, M. J. *Chemistry of Materials* **17**, 1479–1486 (2005).

[121] Roy, I. and Gupta, M. N. *Methods in Biotechnology* **22**, 87–95 (2006).

[122] Hudson, S., Cooney, J., and Magner, E. *Angewandte Chemie International Edition* **47**(45), 8582–8594 (2008).

[123] Hudson, S., Magner, E., Cooney, J., and Hodnett, B. K. *Journal of Physical Chemistry B* **109**, 19496–19506 (2005).

[124] Diaz, J. F. and Balkus, K. J. *Journal of Molecular Catalysis B-enzymatic* **2**(2-3), 115–126 (1996).

[125] Deere, J., Magner, E., Wall, J. G., and Hodnett, B. K. *Biotechnology Progress* **19**(4), 1238–1243 (2003).

[126] Hu, X., Spada, S., White, S., Hudson, S., Magner, E., and Wall, J. G. *Journal of Physical Chemistry B* **110**(37), 18703–18709 (2006).

[127] He, J., Song, Z., Ma, H., Yang, L., and Guo, C. *Journal of Materials Chemistry* **16**(44), 4307–4315 (2006).

[128] Feil, F., Cauda, V., Bein, T., and BrÃď uchle, C. *Nano Letters* **12**(3), 1354–1361 (2012).

[129] Takahashi, H., Li, B., Sasaki, T., Miyazaki, C., Kajino, T., and Inagaki, S. *Chemistry of Materials* **12**(11), 3301–3305 (2000).

[130] Takahashi, H., Li, B., Sasaki, T., Miyazaki, C., Kajino, T., and Inagaki, S. *Microporous and Mesoporous Materials* **44**, 755–762 (2001).

[131] Fadnavis, N. W., Bhaskar, V., Kantam, M. L., and Choudary, B. M. *Biotechnology Progress* **19**(2), 346–351 (2003).

[132] Lee, C. H., Lang, J., Yen, C. W., Shih, P. C., Lin, T. S., and Mou, C. Y. *Journal of Physical Chemistry B* **109**(25), 12277–12286 (2005).

[133] Aburto, J., Ayala, M., Bustos-Jaimes, I., Montiel, C., Terres, E., Dominguez, J. M., and Torres, E. *Microporous and Mesoporous Materials* **83**(1-3), 193–200 (2005).

[134] Sasaki, T., Kajino, T., Li, B., Sugiyama, H., and Takahashi, H. *Applied and Environmental Microbiology* **67**(5), 2208–2212 (2001).

[135] Yiu, H. H. P., Wright, P. A., and Botting, N. P. *Microporous and Mesoporous Materials* **44**, 763–768 (2001).

[136] Deere, J., Magner, E., Wall, J. G., and Hodnett, B. K. *Journal of Physical Chemistry B* **106**(29), 7340–7347 (2002).

[137] Vinu, A., Murugesan, V., Tangermann, O., and Hartmann, M. *Chemistry of Materials* **16**(16), 3056–3065 (2004).

[138] Fan, J., Lei, J., Wang, L. M., Yu, C. Z., Tu, B., and Zhao, D. Y. *Chemical Communications* **17**, 2140–2141 (2003).

[139] Qiao, S. Z., Djojoputro, H., Hu, Q., and Lu, G. Q. *Progress In Solid State Chemistry* **34**(2-4), European Materials Res Soc (2006).

[140] Lei, J., Fan, J., Yu, C. Z., Zhang, L. Y., Jiang, S. Y., Tu, B., and Zhao, D. Y. *Microporous and Mesoporous Materials* **73**(3), 121–128 (2004).

[141] Tortajada, M., Ramon, N., Beltran, D., and Amoros, P. *Journal of Materials Chemistry* **15**(35-36), 3859–3868 (2005).

[142] Sun, J. M., Zhang, H., Tian, R. J., Ma, D., Bao, X. H., Su, D. S., and Zou, H. F. *Chemical Communications* **12**, 1322–1324 (2006).

[143] Kisler, J. M., Dahler, A., Stevens, G. W., and O'Connor, A. J. *Microporous and Mesoporous Materials* **44**, 769–774 (2001).

[144] Zhao, D. Y., Huo, Q. S., Feng, J. L., Chmelka, B. F., and Stucky, G. D. *Journal of the American Chemical Society* **120**, 6024–6036 (1998).

[145] Vinu, A., Miyahara, M., and Ariga, K. *Journal of Physical Chemistry B* **109**, 6436–6441 (2005).

[146] Ji, L., Katiyar, A., Pinto, N. G., Jaroniec, M., and Smirniotis, P. G. *Microporous and Mesoporous Materials* **75**, 221–229 (2004).

[147] Katiyar, A., Ji, L., Smirniotis, P. G., and Pinto, N. G. *Microporous and Mesoporous Materials* **80**, 311–320 (2005).

[148] Hernandez, M. C. R., Wejebe, J. E. M., Alcantara, J. I. V., Ruvalcaba, R. M., Serrano, L. A. G., and Ferrara, J. T. *Microporous and Mesoporous Materials* **80**, 25–31 (2005).

[149] Hudson, S., Cooney, J., Hodnett, B. K., and Magner, E. *Chemistry of Materials* **19**, 2049–2055 (2007).

[150] NICHOLLS, A., SHARP, K. A., and HONIG, B. *Proteins-structure Function and Genetics* **11**, 281–296 (1991).

[151] Lei, C. H., Shin, Y. S., Liu, J., and Ackerman, E. J. *Journal of the American Chemical Society* **124**, 11242–11243 (2002).

[152] Lei, C., Shin, Y., Magnuson, J. K., Fryxell, G., Lasure, L. L., Elliott, D. C., Liu, J., and Ackerman, E. J. *Nanotechnology* **17**, 5531–5538 (2006).

[153] Han, Y. J., Watson, J. T., Stucky, G. D., and Butler, A. *Journal of Molecular Catalysis B-enzymatic* **17**(1), PII S1381–1177(01)0072–8 (2002).

[154] Hartmann, M. and Streb, C. *Journal of Porous Materials* **13**, Int Union Mat Res Soc; Mat Res Soc Singapore; Suntec Int Convent &EOLEOLExhibit Ctr (2006).

[155] Iler, R. K. *The Chemistry of Silica.* Wiley, New York, (1979).

[156] Hoffmann, F., Cornelius, M., Morell, J., and Froeba, M. *Angewandte Chemie-international Edition* **45**, 3216–3251 (2006).

[157] Yadav, G. D. and Jadhav, S. R. *Microporous and Mesoporous Materials* **86**, 215–222 (2005).

[158] Han, Y., Lee, S. S., and Ying, J. Y. *Chemistry of Materials* **18**, 643–649 (2006).

[159] Chong, A. S. M. and Zhao, X. S. *Catalysis Today* **93-5**, 293–299 (2004).

[160] Jing, H., Li, X. F., Evans, D. G., Duan, X., and Li, C. Y. *Journal of Molecular Catalysis B-enzymatic* **11**, 45–53 (2000).

[161] Zhang, X., Guan, R. F., Wu, D. Q., and Chan, K. Y. *Journal of Molecular Catalysis B-enzymatic* **33**, 43–50 (2005).

[162] Pandya, P. H., Jasra, R. V., Newalkar, B. L., and Bhatt, P. N. *Microporous and Mesoporous Materials* **77**, 67–77 (2005).

[163] Salis, A., Meloni, D., Ligas, S., Casula, M. F., Monduzzi, M., Solinas, V., and Dumitriu, E. *Langmuir* **21**, 5511–5516 (2005).

[164] Lei, C., Shin, Y., Liu, J., and Ackerman, E. J. *Nano Letters* **7**, 1050–1053 (2007).

[165] Szymanska, K., Bryjak, J., Mrowiec-Bialon, J., and Jarzebski, A. B. *Microporous and Mesoporous Materials* **99**, 167–175 (2007).

[166] Montiel, C., Terres, E., Dominguez, J.-M., and Aburto, J. *Journal of Molecular Catalysis B-enzymatic* **48**, 90–98 (2007).

[167] Lue, Y., Lu, G., Wang, Y., Guo, Y., Guo, Y., Zhang, Z., Wang, Y., and Liu, X. *Advanced Functional Materials* **17**, 2160–2166 (2007).

[168] Schlossbauer, A., Schaffert, D., Kecht, J., Wagner, E., and Bein, T. *Journal of the American Chemical Society* **130**, 12558–12559 (2008).

[169] Xue, P., Lu, G. Z., Guo, Y. L., Wang, Y. S., and Guo, Y. *Journal of Molecular Catalysis B-enzymatic* **30**, 75–81 (2004).

[170] Goradia, D., Cooney, J., Hodnett, B. K., and Magner, E. *Journal of Molecular Catalysis B-enzymatic* **32**, 231–239 (2005).

[171] Kim, M. I., Kim, J., Lee, J., Jia, H., Bin Na, H., Youn, J. K., Kwak, J. H., Dohnalkova, A., Grate, J. W., Wang, P., Hyeon, T., Park, H. G., and Chang, H. N. *Biotechnology and Bioengineering* **96**, 210–218 (2007).

[172] Kao, K.-C., Lee, C.-H., Lin, T.-S., and Mou, C.-Y. *J. Mater. Chem.* **20**, 4653–4662 (2010).

[173] Deere, J., Magner, E., Wall, J. G., and Hodnett, B. K. *Chemical Communications* , 465–466 (2001).

[174] Pisklak, T. J., Macias, M., Coutinho, D. H., Huang, R. S., and Balkus, Kenneth J., J. *Topics In Catalysis* **38**(4), N Amer Catalysis Soc (2006).

[175] Blanco, R. M., Terreros, P., Fernandez-Perez, M., Otero, C., and Diaz-Gonzalez, G. *Journal of Molecular Catalysis B-enzymatic* **30**(2), 83–93 (2004).

[176] Seelan, S., Sinha, A. K., Kato, K., and Yokogawa, Y. *Advanced Materials* **18**, 3001 (2006).

[177] Zheng, L. Y., Zhang, S. Q., Zhao, L. F., Zhu, G. S., Yang, X. Y., Gao, G., and Cao, S. G. *Journal of Molecular Catalysis B-enzymatic* **38**, 119–125 (2006).

[178] Ma, H., He, J., Evans, D. G., and Duan, X. *Journal of Molecular Catalysis B-enzymatic* **30**, 209–217 (2004).

[179] Demchenko, A. *Methods and Applications in Fluorescence* **1**(2), 022001 (2013).

[180] Andreescu, S. and Sadik, O. A. *Pure Applied Chemistry* **76**, 861–878 (2004).

[181] Patel, P. D. *TrAC Trends in Analytical Chemistry* **21**(2), 96 – 115 (2002).

[182] Riu, J., Maroto, A., and Rius, F. X. *Talanta* **69**(2), 288 – 301 (2006).

[183] Gooding, J. J. *Analytica Chimica Acta* **559**(2), 137 – 151 (2006).

[184] Goldman, E. R., Balighian, E. D., Mattoussi, H., Kuno, M. K., Mauro, J. M., Tran, P. T., and Anderson, G. P. *Journal of the American Chemical Society* **124**(22), 6378–6382 (2002).

[185] Fortina, P., Kricka, L. J., Graves, D. J., Park, J., Hyslop, T., Tam, F., Halas, N., Surrey, S., and Waldman, S. A. *Trends in Biotechnology* **25**(4), 145 – 152 (2007).

[186] `http://www.chemgapedia.de/vsengine/vlu/vsc/de/ch/13/vlu/kinetik/affinitaet/affinitaetsreaktionen.vlu/Page/vsc/de/ch/13/pc/kinetik/affinitaet/immunoassay.vscml.html`.

[187] Rall, J. E. *Biographical Memoirs*. National Academy of Sciences, (1990).

[188] `http://en.wikipedia.org/wiki/Immunoassay`.

[189] Tsekenis, G., Garifallou, G.-Z., Davis, F., Millner, P. A., Gibson, T. D., and Higson, S. P. J. *Analytical Chemistry* **80**(6), 2058–2062 (2008).

[190] Janeway, C., Travers, P., Walport, M., and Shlomchik, M. *Immunobiology: The Immune System in Health and Disease*. Garland Science, (2001).

[191] `http://www.darpa.mil/uploadedImages/Content/Our_Work/DSO/Programs/Antibody_Technology_Program/Antibody20Technology20Program20ATP1%5B1%5D.jpg`.

[192] Cole, S., Campling, B., Atlaw, T., Kozbor, D., and Roder, J. *Molecular and Cellular Biochemistry* **62**(2), 109–120 (1984).

[193] Van Weemen, B. K. and Schuurs, A. *FEBS Letters* **15**(3), 232 – 236 (1971).

[194] Engvall, E. and Perlmann, P. *Immunochemistry* **8**(9), 871 – 874 (1971).

[195] `http://www.epitomics.com/images/products/sandwich.jpg`.

[196] `http://upload.wikimedia.org/wikipedia/commons/a/a9/ELISA.jpg`.

[197] Linares, E. *Nanostructured labels for enhanced paper based immunoassays.* PhD thesis, LMU Munich, (2013).

[198] de la Escosura-Muiz, A., Parolo, C., and Merkoi, A. *Materials Today* **13**(7-8), 24–34 (2010).

Chapter 2

Characterization Techniques

2.1 Infrared (IR) and Raman spectroscopy

Analytical infrared studies are based on the absorption of electromagnetic radiation between 200 - 4000 cm^{-1}.[1] Infrared (IR) and Raman vibrational spectroscopy techniques are two of the most common spectroscopic methods used for compound identification. Especially for organic substances, the light absorbed by the sample is characteristic for the contained functionalities, resulting in a form of functional group fingerprinting.[2] Molecules possessing an electric dipole which oscillates with a specific frequency are able to absorb infrared radiation as long as the frequency of the incident light is matching the frequency of the oscillating non-symmetrical bond of the irradiated molecule.[3] In general, photon absorption occurs if the dipole moment of a molecule changes during the vibration even if the molecule itself does not have a permanent dipole. The energy of the absorbed light is converted into energy of molecular vibration, either stretching or bending, while the transmitted light is detected.

In contrast to IR, Raman spectroscopy relies on the inelastic scattering of monochromatic light by interaction with the electron clouds around chemical bonds. The scattered light can show either a shift towards lower frequencies (Stokes shift), that corresponds to an energy loss, or towards higher frequencies (anti-Stokes shift), that

corresponds to an energy gain from the sample (Figure 2.1).[4]

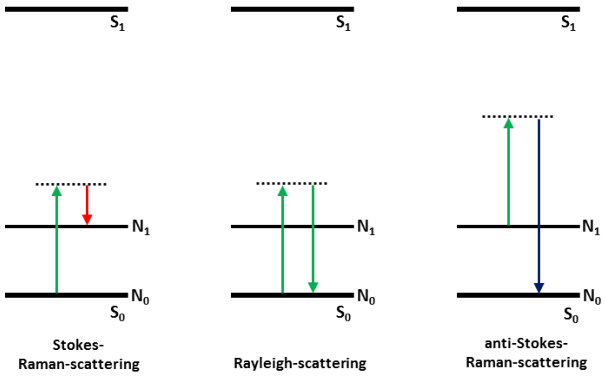

Figure 2.1: Rayleigh-, Stokes-, and anti-Stokes scattering.[4]

To observe a vibrational mode in Raman spectroscopy, the polarizability of the bond has to change during vibration. In IR spectroscopy using an interferometer, a time-dependent signal is detected, which can be decomposed into a frequency-dependent spectrum using Fourier Transformation.[5]

2.2 Dynamic Light Scattering (DLS)

Dynamic light scattering (DLS), which is also known as photon correlation spectroscopy (PCS), is a powerful tool to investigate solution dynamics and to determine hydrodynamic particle diameters in colloidal dispersions.[6] Size information can be obtained ranging from a few nanometers to about 5 micrometers. A DLS setup comprises a laser source, a sample cell, a photodetector and a computer with an autocorrelator (Figure 2.2).[1]

Hydrodynamic particle diameters in colloidal dispersion can be determined by measuring the intensity fluctuations caused by interference of scattered laser light from different particles. The Brownian motion of the particles leads to intensity fluctuations of the laser light. These fluctuations can be mathematically correlated to the particle size. Coherent laser light scattered from small particles suspended in a liquid results in a speckle pattern on the detector due to constructive and

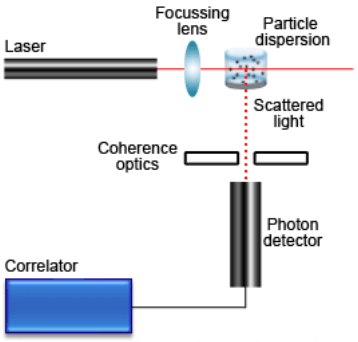

Figure 2.2: Typical instrument arrangement for DLS.[1]

destructive interference of the light resulting from particles at different positions. Without Brownian motion, the speckle pattern would also remain unchanged. In dynamic light scattering, intensity fluctuations are correlated across microsecond time scales by an autocorrelation function. The second order autocorrelation curve can be directly derived from the intensity profile according to equation 2.1.

$$g^2(q;\tau) = \frac{\langle I(t)I(t+\tau)\rangle}{\langle I(t)^2\rangle} \tag{2.1}$$

q: Wave vector

τ: Time delay

I: Intensity

For completely monodisperse samples, an exponential function (2.2; 2.3) is obtained for the decay of the autocorrelation function.

$$g^1(q;\tau) = e^{-\Gamma t} \tag{2.2}$$

$$\Gamma = \frac{D}{\left(\frac{4n_0\pi}{\lambda} sin\left(\frac{\Theta}{2}\right)\right)^2} \tag{2.3}$$

D: Diffusion coefficient

n_0: Refractive index of the solution

λ: Wavelength of the laser

Θ: Angle of the scattering measurement

The diffusion coefficient D of the particles can be determined from the exponent of the fitted curves. The hydrodynamic diameter of an equivalent sphere is calculated using the Stokes-Einstein equation (2.4).[7]

$$D = \frac{kT}{3\pi\eta d} \tag{2.4}$$

D: Diffusion coefficient

k: Boltzmann constant

T: Temperature

η: Solvent viscosity

d: Hydrodynamic diameter

In samples with broad or polymodal size distributions, the interpretation of data based on the particle scattering intensity can be misleading. In order to describe the scattering of particles with a similar or larger size compared to the wavelength of the incoming light, Mie theory has to be applied. For small particles, the scattering intensity in a beam of unpolarized light can be sufficiently described by Rayleigh scattering (2.5).

$$I = I_0 \frac{1 + \cos^2\Theta}{2R^2} \left(\frac{2\pi}{\lambda}\right)^4 \left(\frac{n^2 - 1}{n^2 + 2}\right)^2 \left(\frac{d}{2}\right)^6 \tag{2.5}$$

I: Intensity of the scattered light

I_0: Intensity of the incoming light

Θ: Scattering angle

R: Distance to the particle

λ: Wavelength of the incoming light

n: Refractive index of the particle

d: Particle diameter

In equation 2.5, the scattering intensity is proportional to d^6, which leads to the fact that aggregates or larger particles dominate the distribution curve even if they are only present in a small amount. Therefore, it is common to give the volume-weighted or number-weighted size distributions which are proportional to d^3 and d, respectively.

2.3 Zeta potential measurement

The zeta potential is the electrokinetic potential difference between the dispersion medium and the stationary layer of fluid attached to the dispersed particle.[8] It is a force that mediates interactions between colloidal particles. Basically, dispersed particles in aqueous solutions undergo either ionization of their surface groups or adsorption of charged species, both resulting in a charged particle surface. This surface charge affects the distribution of surrounding ions, generating different layers around the particle with ion concentrations that differ from the bulk solution.[9] Colloidal particles will therefore form an electric double layer in ion-containing media. The liquid layer formed directly at the particle surface is called the Stern layer. Here, the ions are strongly bound to the surface in the first few layers. With further distance to the particle surface, ionic interactions decrease leading to a more diffuse layer (Figure 2.3).[10]

One possibility for zeta potential determination is the measurement of the electrophoretic mobility. The relation between the electrophoretic mobility and the zeta potential is described by the Henry equation 2.6.[10]

$$U_E = \frac{2\epsilon z f(Ka)}{3\eta} \tag{2.6}$$

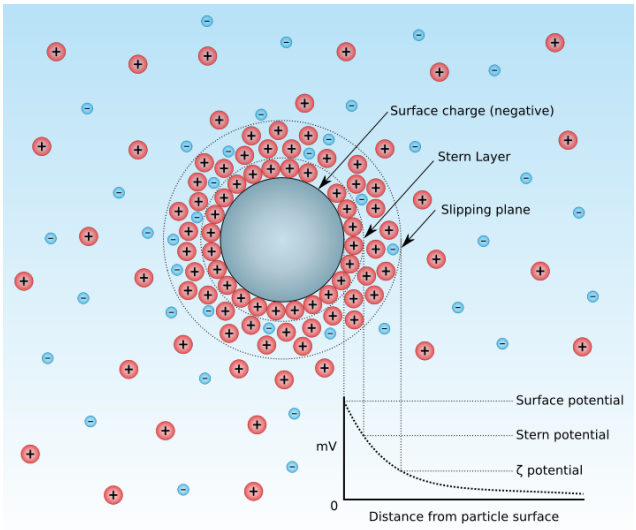

Figure 2.3: Scheme of the electric double layer around a negatively charged colloid.[11]

U_E: Electrophoretic mobility

ϵ: Dielectric constant

z: Zeta potential

$f(Ka)$: Henry's function

η: Viscosity of the solvent

The electrophoretic mobility of colloidal nanoparticles can be determined by the measurement of the particles' velocity through Laser Doppler Velocimetry (LDV).[12] Laser light that is scattered from the moving particles is interfered with a reference beam, resulting in a fluctuating signal intensity due to the Doppler shift. The Doppler shift corresponds to the velocity of the particles. The resulting frequency difference forms beat signals, which are proportional to the speed of the particles between the electrodes in a measurement cell. For very small particles (<200 nm) dispersed in electrolytes containing less than 10^{-3} molar salt, the Hückel approximation is used with $f(Ka) = 1.0$. For larger particles in more highly concentrated solvents, the particle radii are better described by the Smoluchowski approximation with $f(Ka) = 1.5$.

2.4 Nitrogen adsorption

Gas adsorption and desorption analysis is a prominent method to characterize porous materials with respect to the specific surface area, pore size distribution and accessible pore volume.[13] Argon, nitrogen or krypton are the most common adsorptives. In principle, a known amount of sample is placed in the sample cell before the device is evacuated ($p = 0$). The temperature is adjusted to the temperature of the adsorptive - in the case of nitrogen to 77 K. The adsorptive is successively added to the sample cell and the resulting pressure is recorded after equilibration. The upper limit is reached, as soon as the measured pressure p equals the vapor pressure of nitrogen p_0. Plotting the volume of adsorbate on the adsorbent as a function of its relative pressure p/p_0 at a constant temperature T gives an isotherm representing the adsorption process. Subsequent successive removal of the adsoptive leads to the corresponding desorption istotherm.[14] Adsorption isotherms can be classified as one of six different types according to IUPAC nomenclature (Figure 2.4)[15]

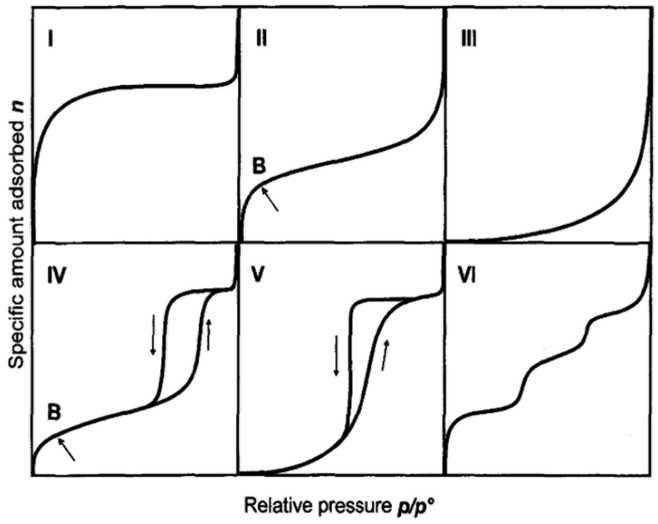

Figure 2.4: Types of physisorption isotherms according to IUPAC nomenclature. B represents a monomolecular adsorbate layer on the material.[15]

Every type of isotherm in Figure 2.4 is characteristic for a certain gas/solid interaction (Table 2.1).

Table 2.1: Classification of adsorption isotherms.[15]

Isotherm Type	Corresponding Material
I	Microporous material, remains static after complete pore filling
II	Nonporous or macroporous material, high adsorption energy
III	Nonporous or macroporous material, low adsorption energy, weak interaction between adsorbate and adsorbent
IV	Mesoporous material
V	Mesoporous material with very weak interaction between adsorbate and adsorbent
VI	Stepwise multilayer adsorption on nonporous, uniform material

The shape of the isotherms is influenced by the phase behavior of fluids in porous materials: usually, physical adsorption of gases on a porous surface occurs via a layer-by-layer mechanism, which means that initially a monolayer is built. In the case of mesoporous materials, the phenomenon of capillary condensation is observed.[16] The latter is a process, during which multilayer adsorption from the vapor phase into a porous medium proceeds until the pores are completely filled with condensed liquid. There exist several different models for describing adsorption isotherms. The two most prominent methods applied for the study of porous materials are the Brunauer-Emmett-Teller (BET) model and the density functional theory (DFT). BET theory is based on the Langmuir model.[17] For small relative pressures in the range $p/p_0 < 0.3$, the linear form of the BET equation is used (equation 2.7).

$$\frac{p/p^0}{n(1-p/p^0)} = \frac{1}{n_m C} + \frac{C-1}{n_m C}(p/p^0) \tag{2.7}$$

p/p^0: Relative pressure

p^0: Saturation pressure of the adsorptive

n: Amount of adsorbate

n_m: Monolayer capacity

C: BET constant

Using this equation together with the known cross-sectional area of an adsorbate molecule, the specific surface area of the material can be calculated from the linear region in the BET plot.

Based on the Kelvin equation, Barret, Joyner and Halenda (BJH) developed a model which allows to calculate pore diameters of mesoporous materials. [18] For mesoporous systems with pores sizes around 4 nm, pore diameters derived from BJH theory are typically decreased by about 1 nm in comparison with pore sizes determined by other techniques like TEM. In BJH theory, assumptions of certain pore condensation and pore filling mechanisms are made, which do not describe the behaviour of micropores and small mesopores accurately. Besides the macroscopic BJH approach, several microscopic models including Monte Carlo simulations, molecular dynamics, statistical mechanics techniques and density functional theory (DFT) have been developed. These models benefit from yielding more realistic results, but specific knowledge about the structure and surface atoms of the investigated systems is required in order to be able to correctly calculate forces and input parameters. Among these theories, DFT techniques use site-wise attractions between surface atoms and the adsorbate molecules. Additionally, adsorbate-adsorbate attractions are taken into account. The minimum in the system's overall free energy is obtained by primarily changing the number density as a function of distance from the surface. Additionally, one has to distinguish between the local and the non-local density functional theory (NLDFT). In local density functional theory, the fluid is assumed to be structureless for calculating the long-range interactions between adsorbate particles. However, the solid pore walls of mesoporous materials have considerable influence on the number density. Therefore, NLDFT has to be used for surface adsorption with strongly interacting boundaries.

2.5 Thermogravimetric Analysis (TGA)

Thermogravimetric analysis (TGA) is a tool to determine the content of organic material in organic-inorganic hybrids.[19] During a TGA measurement, the mass of a sample in a controlled atmosphere is recorded continously as a function of temperature. Usually, the temperature of the sample is increased linearly with time.[20] Since the mass of the analyte is monitored, the provided information is qunatitative, but limited to decomposition or oxidation and to physical processes such as vaporization, sublimation and desorption.[1] A typical setup contains a sensitive thermobalance which is isolated from the furnace and can detect small changes in mass (0.1 μg). The furnace usually covers a range from room temperature to 1200 °C. Inside the sample chamber, a constant laminar gas flow is applied, leading to a removal of desorbed or combusted material. With this method, information about sample stability and quantitative data on the amount of organic material attached to the inorganic core is obtained.

2.6 Transmission electron microscopy (TEM)

Microscopes using light in the visible range (400 to 800 nm) are limited to a resolution in the range of about 0.2 μm. In materials science, it is often required to get visible information down to the atomic level. Through the development of the first electron microscope by Max Knoll and Ernst Ruska in 1931 and the subsequent enormous improvements of the technique, it is possible to get information on samples with a resolution down to 0.05-0.1 nm. The high resolution is obtained by the use of highly accelerated electrons instead of light. The wavelength of these electrons is related to the accelerating voltage U as shown in equation 2.8.

$$\lambda = \frac{hc}{\left[2m_0eU\left(1 + eU/2m_0c^2\right)\right]^{1/2}} \tag{2.8}$$

m_0: Mass

e: Elementary charge of an electron

h: Planck constant

c: Speed of light

In transmission electron microscopy, acceleration voltages between 80 kV and 200 kV are widely used, corresponding to electron wavelength of 15 pm and 2.51 pm respectively. TEM reveals the internal structure of specimens including cystallinity, defects and composition. The electron beam is generated by a tungsten filament or a field emission gun and accelerated by a potential difference between about 40 to 1000 keV. Before and after hitting the specimen, the beam is collimated and focused by electrostatic and/or electromagnetic lenses. After transmission through the specimen, the electron beam carries information on the inner structure of the sample. At the bottom of the setup, a fluorescence screen or a CCD camera detects the final image.

2.7 Ultraviolet-visible (UV-Vis) spectroscopy

UV-Vis spectroscopy uses light in the ultraviolet or visible range. Absorption of light can lead to excitation of valence electrons from the ground state to an excited state. For absorption of light, the energy of the incident light has to match the energy difference between these two states. The concentration of an analyte in the sample can be determined using Lambert-Beer's law (equation 2.9).[2]

$$A = -log\frac{I}{I_0} = \epsilon cd \tag{2.9}$$

A: Absorbance

I: Transmitted intensity

I_0: Intensity of incident light

ϵ: Molar extinction coefficient of the analyte

c: Concentration of the analyte

d: Path length

2.8 Fluorescence Spectroscopy

Fluorescence is the result of a three-stage process in the electron shell of certain molecules (generally polyaromatic hydrocarbons or heterocycles) called fluorophores or fluorescent dyes. The process of fluorescence can be illustrated by a simplified electronic state diagram (Jablonski diagram) in Figure 2.5:[21]

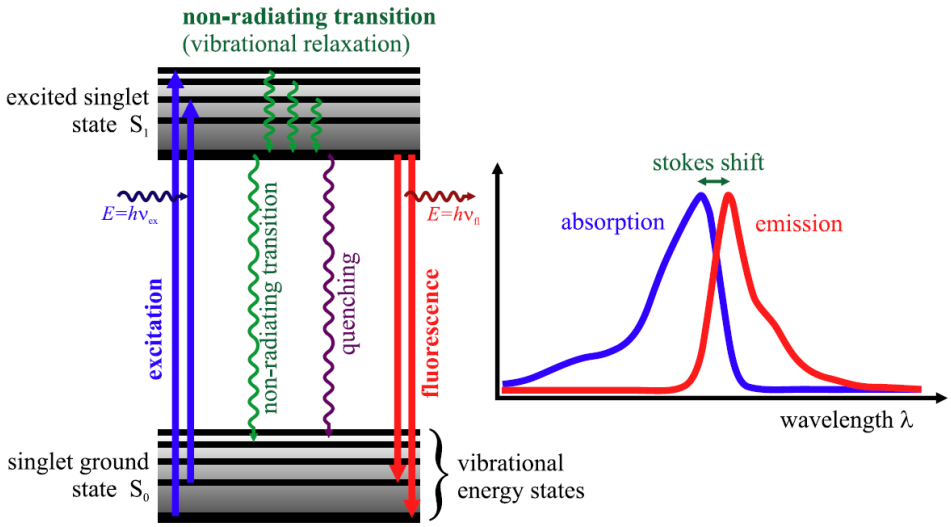

Figure 2.5: Jablonski diagram and spectra, illustrating the processes involved on the creation of an excited state by optical absorption and subsequent emission of fluorescence.[22]

Fluorescence can be divided into three main processes: excitation, Non-radiating transitions and fluorescence emission.

Excitation: A photon of energy $h\nu_{ex}$ is supplied by an external source such as an incandescent lamp or a laser and absorbed by the fluorophore. The energy is used to push an electron from a ground state (S_0) niveau to an excited state (S_1) niveau. The absorption occurs in about 1 fs.

Non-radiating transitions: The electron spends a finite time (typically 1 - 10 ns) in the excited state. During this time, the fluorophore undergoes conformational changes and is subject to a multitude of possible interactions with its environment (collision...). The energy of the initial S_1 state is partially dissipated, yielding a relaxed singlet excited state from which fluorescence emission originates. Not all

molecules that were initially excited by absorption return to the ground state by fluorescence. Other processes such as collisional quenching, fluorescence energy transfer and intersystem crossing may also depopulate S_1 without emitting a photon.

Fluorescence emission: Finally, with a certain probability a photon of energy $h\nu_{fl}$ is emitted, returning the fluorophore to its ground state S_0. Due to energy dissipation during the excited state lifetime (non-radiative relaxation), the energy of this photon is lower, and therefore of longer wavelength, than the excitation photon $h\nu_{ex}$. The energy difference is related to the Stokes shift, which is the wavelength difference between the absorption and emission maximum.[22]

2.9 X-ray diffraction (XRD)

X-ray diffraction (XRD) is a powerful and nondestructive method for the analysis of crystalline and nanostructured materials.[23] XRD can also give information on particle shape and size in the range from a few nm to about 100 nm. Since larger structures go along with small angles of diffraction, an angular range of 0.1 - 10 ° was applied here.[24] Hence, small angle X-ray scattering (SAXS) was used in this work to demonstrate the mesostructure of the synthesized silica materials.

X-rays are typically generated by the bombardment of a metal target with an energetic beam of electrons. This electron beam is produced by heating a metal filament. Emitted electrons are then accelerated towards the metal target by applying a large electrical potential between the filament and the target. When the electron beam hits the target, a rapid deceleration of electrons causes a variety of processes: the emission of X-ray radiation, Auger electrons, photoelectrons and heat. X-ray radiation is emitted in a continuous band of white radiation as well as a series of discrete lines that are characteristic for the target material.[25] In the case of copper, the characteristic wavelength of the X-ray beam is 1.54182 Å.

The wavelength of the X-ray beam lies in the same order of magnitude as the distances of atoms in solid matter. Therefore, information on the atomic structure of the material can be gained by interpreting the constructive and destructive interfer-

ences of X-rays scattered by the lattice planes (Figure 2.6).

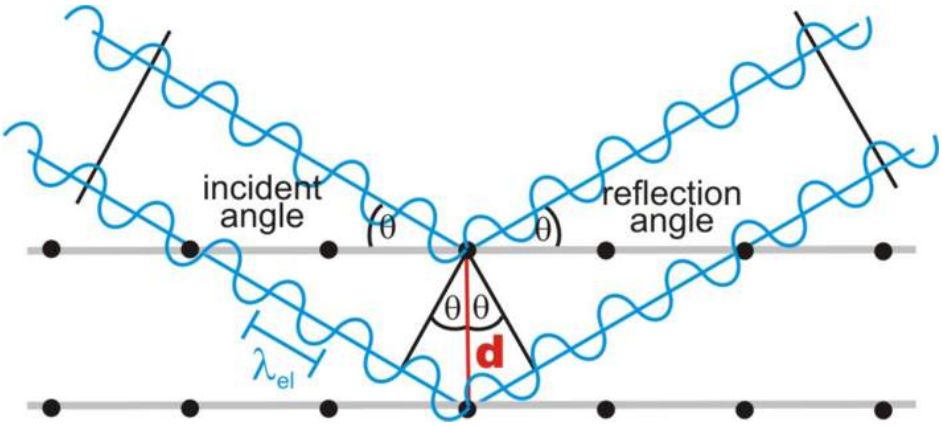

Figure 2.6: Illustration of the Bragg relation. A constructive interference occurs when the path difference is a multiple integer of the X-ray wavelength.[26]

The interplanar spacing d of a structure can be determined from the Bragg equation:

$$n\lambda = 2dsin(\Theta) \tag{2.10}$$

n: Diffraction order

λ: Characteristic wavelength

d: Interplanar spacing

Θ: Angle of incidence

Bibliography

[1] Skoog, D., Holler, F., and Crouch, S. *Principles of Instrumental Analysis.* Thomson/Brooks/Cole, (2007).

[2] Hesse, M., Meier, H., and Zeeh, B. *Spectroscopic Methods in Organic Chemistry.* Thieme, (2008).

[3] Günzler, H. and Gremlich, H. *IR- Spektroskopie: Eine Einführung.* Wiley-VCH, (2003).

[4] `www.raman.de`.

[5] Mermet, J., Otto, M., Kellner, R., and Cases, M. *Analytical chemistry: a modern approach to analytical science.* Wiley- VCH, (2004).

[6] Berne, B. J. and Pecora, R. *Dynamic Light Scattering with Applications to Chemistry, Biology and Physics.* Wiley, New York, (1976).

[7] Edward, J. T. *Journal of Chemical Education* **47**(4), 261 (1970).

[8] Butt, H., Graf, K., and Kappl, M. *Physics and chemistry of interfaces.* Wiley-VCH, (2003).

[9] Xu, R. *Particle characterization: light scattering methods.* Academic, (2000).

[10] Evans, D. F. and Wennerström, H. *The Colloidal Domain: Where Physics, Chemistry, Biology, and Technology meet.* Wiley-VCH, (1999).

[11] `www.malvern.com/labeng/technology/images/zeta_potential_schematic.png`.

[12] *Malvern Instruments, Zetasizer Nano Series - User Manual*, (2003).

[13] d. Boer, J. H. *The Structure and Properties of Porous Materials.* Butterworths London, (1958).

[14] Lowell, S., Shields, J. E., Thomas, M. A., and Thommes. *Characterization of Porous Solids and Powders: Surface Area, Pore Size and Density.* Springer, (2006).

[15] Sing, K. S. W., Everett, D. H., Haul, R. A. W., Moscou, L., Pierotti, R. A., Rouquerol, J., and Siemieniewska, T. *Pure and Applied Chemistry* **57**, 603 (1985).

[16] Cao, G., Zhang, Q., and Brinker, C. *Annual Review of Nano Research.* World Scientific, (2009).

[17] Rouquerol, F., Rouquerol, J., and Sing, K. *Adsorption by Powders & Porous Solids - Principles, Methodology and Application.* Academic Press, (1999).

[18] Condon, J. B. *Surface Area and Porosity Determinations by Physisorption - Measurements and Theory.* Elsevier, Amsterdam, (2006).

[19] Sepe, M. and Limited, R. T. *Thermal analysis of polymers.* Rapra Technology Limited, (1997).

[20] Fifield, F. and Kealey, D. *Principles and practice of analytical chemistry.* Blackwell Science, (2000).

[21] Atkins, P. W. *Physikalische Chemie.* Wiley-VCH, (2001).

[22] (DKFZ), D. K. H.

[23] Fratzl, P. *Journal of Applied Crystallography* **36**, 397 – 404 (2003).

[24] Guinier, A. and Fournet, G. *Small-angle scattering of X-rays.* Wiley, New York, (1955).

[25] Cullity, B. and Stock, S. *Elements of x-ray diffraction.* Prentice Hall, (2001).

[26] http://www.microscopy.ethz.ch/images/bragg_welle.jpg.

Chapter 3

Tuning the Activity of Immobilized Enzymes via Pore-Wall Modifications of Mesoporous Silica Particles with pH-active Functionalities

The following work is based on a project with Marina Ilg, Evelyn Calta, Axel Schlossbauer, and Thomas Bein

3.1 Introduction

Organo-functionalized mesoporous silica materials have attracted much attention as host systems for biomolecules in the field of biocatalysis and drug delivery.[1–6] Having most of their active surface area inside the mesopores, high functionalization densities can be found in these confined nanospaces. Enzymes are versatile biocatalysts with a broad range of industrial applications including synthesis and purification of fine chemicals, due to their high selectivity and activity at moderate temperatures.[7] An important aspect in enzymatic catalysis is the recovery of the catalyst. As a result of extensive studies, the concept of immobilization was developed.[8–12] Encapsulation of enzymes in host materials such as mesoporous si-

lica has proven to be beneficial for resistance against environmental influences like pH, temperature and solvent variations. Often biomolecules have been immobilized *via* physical adsorption or encapsulation.[11–16] Other studies have explored the concept of cross-linking[17] or the covalent attachment of enzymes to solid supports.[10] However, as a consequence of immobilization, a drop in enzymatic activity can be observed in many systems.[18–21] This suggests that local interactions of the enzyme molecules with the pore walls of the host should be further elucidated in order to understand and optimize the performance of bio-inorganic catalyst systems.

Here we present investigations on the impact of different pore-wall modifications of mesoporous silica particles on the internal pH of the pores. These modifications show significant effects on the catalytic activity of immobilized trypsin and hemin molecules. The active site of trypsin consists of aspartic acid, histidine and serine residues, creating the catalytic triad that is a key characteristic of serine proteases. The mechanism of catalytic action depends on protonation and deprotonation steps within this triad.[22] Hence, the local pH value in the neighborhood of the enzyme is critical for the activity of the enzyme. We synthesized mesoporous silica particles with different pore sizes and pore-wall-functionalities Figure 3.1. Furthermore, the impact of amino- and carboxy-moieties on the catalytic activity of covalently attached trypsin and hemin was elucidated.

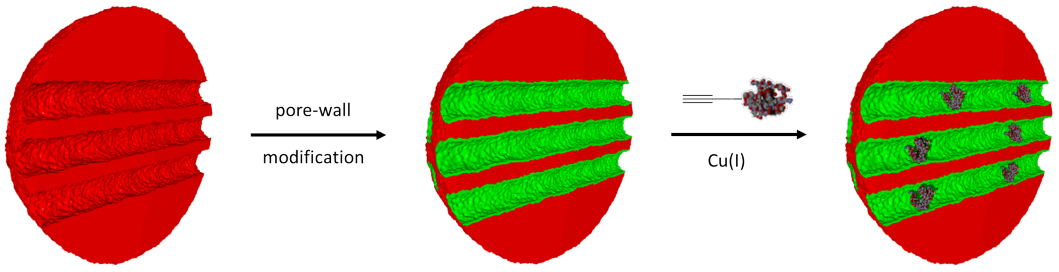

Figure 3.1: Pore-wall modification followed by covalent attachment of a catalyst into the mesoporous system by click chemistry.

3.2 Experimental Section

Chemicals

All reagents were purchased from commercial suppliers: tetraethyl orthosilicate (TEOS, Fluka, >98%), cetyltrimethylammonium bromide (CTAB, Aldrich, 95%), (3-chloropropyl)triethoxysilane (CPTES, Fluka, 95%), (3-cyanopropyl)triethoxysilane (Cyano-PTES, Fluka, 95%), (3-aminopropyl)triethoxysilane (APTES, Fluka, 95%), mesitylene (Aldrich, 98%), sodium azide (Fluka, 99%), 4-pentynoic acid (Fluka, 97%), *N*-(3-dimethylaminopropyl)-*N*-ethylcarbodiimide hydrochloride (EDC, Fluka, 97%), trypsin from bovine pancreas (Sigma, lyophilized, essentially salt free, TPCK treated), *N*-p-tosyl-L-arginine methyl ester hydrochloride (TAME, Sigma), hemin (Sigma, >90%), 4-pentynoic acid (Fluka, 95%), propargylamine (Sigma, 98%), 1-hydroxybenzotriazole hydrate (HOBt, Sigma, >99%), *N*, *N*-diisopropylethylamine (Sigma, 99%), Cu(I)Br (Sigma, 98%), 4-aminoantipyrine (4-AAP, Sigma, >98%), diethylaniline (DEA, Sigma, >99%), hydrogen peroxide (Sigma, 30 wt%). Pluronic P123 was received as a gift from BASF company. (3-azidopropyl)triethoxysilane was synthesized according to a procedure published by Nakazawa *et al.*.[23] Doubly distilled water from a Millipore system (Milli-Q academie A-10) was used for all syntheses and purification steps. All solvents and buffer contents were purchased from Sigma-Aldrich. Unless otherwise noted, all reagents were used without further purification.

Preparation of micrometer sized MCM-41 particles

MCM-41 was synthesized according to a published procedure.[24] To a stirred solution of CTAB (2.39 g), water (125 g), ethanol (12.5 g) and aqueous ammonia (25 wt%, 9.18 g), the amount of 17.56 g TEOS was added. After stirring for 2 h at room temperature, the reaction mixture was filtered off and washed with 50 mL water. The resulting powder was dried at 60 °C for 12 h. Extraction of the organic components was performed by heating the particles for 45 min under reflux (90 °C) in a solution containing 2 g ammonium nitrate in 100 mL ethanol. After filtration,

the particles were fully condensed by calcination at 450 °C for 4 h (heating rate 1 °C/min).

Preparation of large pore SBA-15 particles

SBA-15 was synthesized following a procedure published by Katiyar *et al.*[25] Pluronic P123 (3.0 g) was dissolved in hydrochloric acid (HCl, 60 mL, 1.5 M). In a second reaction vessel CTAB (0.6 g) and mesitylene (0.3 g) were mixed with distilled water (25 mL). Both solutions were combined and ethanol (20 mL) was added under stirring. Subsequently, TEOS (10 mL) was added dropwise. The resulting reaction mixture was vigorously stirred at 35 °C for 45 min before being transferred into a Parr autoclave for hydrothermal treatment at 75 °C for 12 h under static conditions. Subsequently, the reaction mixture was aged at 125 °C for another 12 h. The resulting white powder was filtered off, washed with water (100 mL) and ethanol (100 mL), and dried at 60 °C for 12 h. The template was removed by calcination at 550 °C for 6 h (heating rate 1 °C/min).

General procedure for organo-functionalized SBA-15 (SBA-15-X) and MCM-41 (MCM-41-X) particles

SBA-15 and MCM-41 were functionalized according to a published procedure.[10] Freshly calcined particles (400 mg) were dried at 110 °C under vacuum conditions for 90 minutes. Afterwards, the amount of 6 mL dry toluene was added under nitrogen atmosphere. After addition of 3 mmol of the corresponding functionalized propyltriethoxysilane $X(C_{2-3}H_{4-6})TES$ (X = CN, NH_2, N_3), the reaction mixture was allowed to stir for 4 hours under reflux conditions. The functionalized particles were filtered off and washed with toluene, methanol and water before being dried at 60 °C. For multiple functionalization, two different functionalized propyltriethoxysilanes were used with $n_1 + n_2 = 3$ mmol. In SBA-15 particles prepared for click chemistry, a ratio of NH_2:N_3 = 100:1 or CN:N_3 = 100:1 was used.

General procedure for the conversion of cyano-functionalized into carboxy-functionalized particles

Cyano-functionalized particles (200 mg) were resuspended in concentrated HCl (37%, 15 mL) and stirred for 6 h under reflux conditions. Afterwards, the particles were separated by filtration, washed with water until the filtrate appeared neutral and dried at 60 °C.

Acetylene-functionalization of trypsin (sp-trypsin)

Acetylene-functionalized trypsin was synthesized according to Gole *et al.*[26] A solution containing 10 mg trypsin in 10 mL MES buffer (10 mM, pH 5.5) was prepared. To this solution, 500 μL of an aqueous solution of 4-pentynoic acid (0.1 M) was added. The resulting mixture was stirred for 2 minutes and stored afterwards at 4 °C for 15 minutes. Subsequently, the amount of 9.9 mg EDC hydrochloride was added and the solution was stirred and kept for an additional 4 h at 4 °C. The mixture was dialyzed in a cold room at 6 °C against 10 L sodium phosphate buffer (10 mM, pH 7.4) for a period of 24 h. The resulting acetylene-functionalized trypsin was used for click chemistry without further purification.

Preparation of trypsin-functionalized SBA-15 (SBA-15-NH_2-trypsin, SBA-15-COOH-trypsin)

To a solution containing 3 mg of acetylene-functionalized trypsin (3 mL) in PBS buffer (pH 7.4), the amount of 25 mg SBA-15-NH_2-N_3 or alternatively SBA-15-COOH-N_3 was added. The amount of 1 mg ascorbic acid was added to a freshly prepared aqueous solution of $CuSO_4 \cdot 5\ H_2O$ (1 mM, 5 mL) and the resulting mixture was stirred at room temperature for 10 minutes. Subsequently, 12.5 μL of the copper-containing solution were added to the reaction mixture. The resulting mixture was stirred at 4 °C for 24 h. The trypsin functionalized particles were recovered by filtration and washed extensively with PBS buffer (50 mM, pH 7.4).

Preparation of core-functionalized colloidal mesoporous silica nanoparticles (MSN-N_3)

MSN nanoparticles were synthesized by co-condensation according to Cauda *et al.*[27] A two phase mixture of TEA (14.3 g), TEOS (1.63 g) and 3-azidopropyltriethoxysilane (100 μL) was heated at 90 °C for 20 minutes without stirring. After removal of the oil bath, a preheated (60 °C) solution of CTAC (2.14 mL) and water (21.7 g) was added and stirred afterwards at 500 rpm for 20 min at room temperature. Subsequently, 180 μL of TEOS was added in four steps (45 μL each) every 3 minutes. The resulting solution was stirred overnight at room temperature at 500 rpm. Extraction of the organic template was achieved by heating the ethanol-suspended sample (10 mg/mL) under reflux at 90 °C for 1 h in a mixture of 2 g ammonium nitrate and 100 mL ethanol. Afterwards, the sample was centrifuged for 20 minutes at 19000 rpm (43146 rcf), redispersed in ethanol and heated under reflux at 90 °C in a solution of 8 mL concentrated HCl and 32 mL ethanol for 45 minutes. After centrifugation, the particles were redispersed in ethanol, resulting in a colloidal suspension.

Acetylene-functionalization of hemin (sp-hemin)

In a 50 mL flask, 162 mg hemin and 80 mg HOBt (2 eq.) were dissolved in 6 mL DMF. Subsequently, 42 μL propargylamine (2.5 eq) and 220 μL EDC (4 eq.) were added and the solution was stirred for 12 h at r.t.. DMF was evaporated and the crude product was redissolved in chloroform and washed by extraction with water. The obtained dark green solid was used without further purification.

Preparation of hemin-functionalized colloidal mesoporous silica nanoparticles (MSN-hemin)

100 mg MSN-N_3 were redispersed in 15 mL acetonitrile. Subsequently the amount of 15 mg sp-hemin, Cu(I)Br (12 mg) and N,N-diisopropylethylamine (16 μL) were added to start the click reaction. The mixture was stirred overnight. The sample was washed several times by centrifugation and redispersion in acetonitrile.

pH modification of MSN-hemin by click chemistry with 4-pentynoic acid and propargylamine (MSN-COOH-hemin, MSN-NH_2-hemin)

20 mg MSN-hemin were redispersed in 5 ml acetonitrile. Subsequently, a large excess of the desired alkyne (10 mg), Cu(I)Br (6 mg) and N,N-diisopropylethylamine (8 μL) were added. The mixture was stirred overnight. The sample was washed several times by centrifugation and redispersion in acetonitrile.

Trypsin activity assay

Following a procedure published by Schlossbauer *et al.*,[10] the TAME assay was performed by preparing an aqueous TAME stock solution (0.01 M) and an aqueous enzyme solution with a trypsin concentration of approximately 5 μg/mL. For the activity determination, a 1.5 mL cuvette containing 1325 μL buffer solution and 175 μL of a mixture of TAME and SBA-15-X-trypsin (X = COOH, NH_2) solution was placed in a spectrophotometer. The extinction at 247 nm was acquired at intervals of one minute. Between each acquisition, the reaction mixture was homogenized by shaking. The enzyme activity could be calculated from the slope of the obtained linear equation determined from linear regression of the measured data as follows:

$$\frac{E_{247}}{0.54 \cdot E_w} \cdot 1.5 \tag{3.1}$$

where E_{247} is the increase in extinction at 247 nm per minute (i.e. the slope of the linear regression), 0.54 the extinction of 1 μmol N-p-tosyl-L-arginine, E_w the initial weight of enzyme in mg per 0.1 mL solution and 1.5 the total volume of the sample in mL. Hence, one activity unit is defined as the amount of enzyme releasing 1 μmol $N\alpha$-p-tosyl-L-arginine per minute under the noted conditions.

Hemin activity assay

Stock solutions of 4-AAP (7.5 mM), DEA (7.5 mM) and H_2O_2 (3 wt%) in Mc-Ilvaine buffer solution were prepared. For the activity determination, 148 μL 4-AAP, 252 μL

DEA, 50 μL H_2O_2, 240 μg MSN-hemin (containing 3.7 μg hemin), and buffer solution were mixed. The extinction at 554 nm was acquired at intervals of one second. The catalytic activity could be calculated from the slope of the obtained linear equation determined from linear regression of the measured data as follows:

$$\frac{E_{554}}{16500 \cdot m_{hemin}} \tag{3.2}$$

where E_{554} is the increase in extinction at 554 nm per second, 16500 the molar extinction coefficient of the produced dye[28] and m_{hemin} the initial weight of enzyme in 1 mL test solution.

Preparation of buffer solutions

PBS buffer

The amounts of 8.0 g sodium chloride (NaCl), 0.2 g potassium chloride (KCl), 1.44 g disodium hydrogen phosphate (Na_2HPO_4), and 0.24 g potassium dihydrogen phosphate (KH_2PO_4) were dissolved in 800 mL water. The pH was adjusted to 7.4 using 1 M hydrochloric acid (HCl). The volume was adjusted to 1 L by addition of distilled water.

TRIS buffer

The amounts of 5.57 g tris(hydroxymethyl)aminomethane (TRIS, $C_4H_{11}NO_3$) and 0.169 g calcium chloride dihydrate ($CaCl_2 \cdot 2\ H_2O$) were dissolved in 60 mL of water. The pH was adjusted to 8.1 using 1 M hydrochloric acid (HCl). The volume was adjusted to 100 mL by addition of distilled water.

Mc Ilvaine buffer

0.2 M aqueous solutions of citric acid (9.61 g, 250 mL) and dipotassium phosphate (8.71 g, 250 mL) were prepared. The two solutions were mixed in different ratios in

order to obtain the pH values 4, 5, 6, 7 and 8. Additionally, dilution series of 1:2, 1:20 and 1:200 were prepared for all pH values to give 100 mM, 10 mM and 1 mM solutions.

3.3 Results and Discussion

pH determination inside the meopores of MCM-41 and SBA-15

For pH control in the mesopores, particles with different pore sizes were prepared and modified with cyano-, carboxylic acid- and amino-groups and combinations thereof. Buffers in the reange of pH 4-8 with different ionic strengths were used to ensure a given pH in the external solution. To obtain information on the pH inside of the pores, universal indicator dyes were used. Color changes of differently modified particles allowed inference on the internal pH of the mesopores. The performance of silica supported trypsin was photometrically quantified by the release of $N\alpha$-p-tosyl-L-arginine from $N\alpha$-p-tosyl-L-arginine methyl hydrochloride (TAME).[29] The chromogenic reaction between hydrogen peroxide, 4-aminoantipyrine (4-AAP), and N,N-diethylaniline (DEA) was used for investigation of hemin activity.[28]

For the determination of the pH inside the mesopores, calcined samples of SBA-15 and MCM-41 particles were prepared. Nitrogen sorption experiments showed typical type IV isotherms, with a BET surface area of 1001 m^2/g and an average pore size of 7.9 nm for SBA-15. Sorption measurements of MCM-41 revealed a BET surface area of 811 m^2/g and an average pore size of 3.9 nm (Figure 3.2).

The calcined samples were functionalized by postsynthetic grafting with different organic residues (-NH_2, -CN, -COOH, -CN:NH_2 1:1, -COOH:NH_2 1:1). The successful functionalization was determined by thermogravimetric analysis (TGA, Figure 3.3).

To test the effect of functionalization on the pH inside the mesopores, Mc-Ilvaine

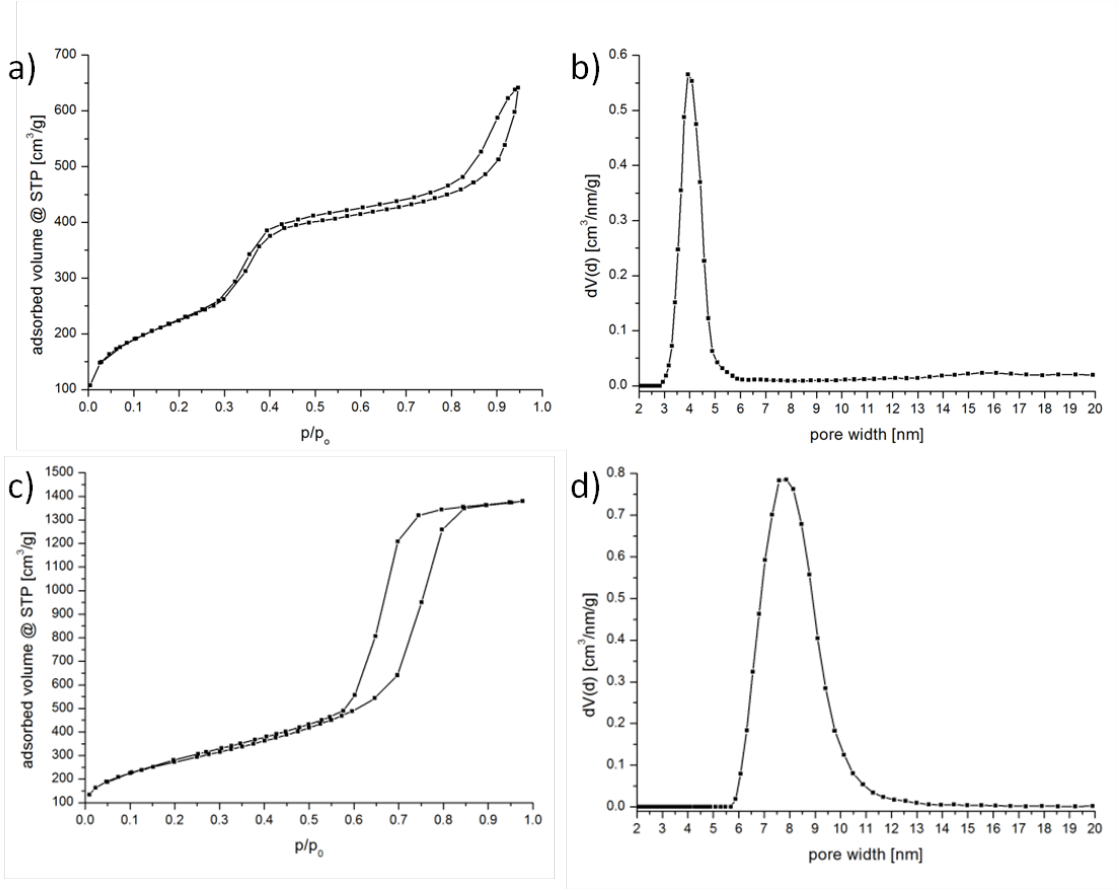

Figure 3.2: Nitrogen sorption isotherms of a) MCM-41 and c) SBA-15. NLDFT pore size distribution of c) MCM-41 and d) SBA-15.

buffer solutions with different pH (4-8) and ionic strengths (1 mM, 10 mM, 100 mM) were prepared. The addition of indicator dye solution to the buffered particle dispersion (10 mg particles, 3 mL buffer, 5 μL indicator) led to differently colored particles for the various modified samples (Figure 3.4) and thus, the internal pH could be obtained through comparison with a color code table.

For calcined MCM-41 particles in a 100 mM buffer (Figure 3.5 a), the high content of silanol groups led to an acidic medium with a pH < 5 inside the pores (black bar in Figure 3.5) even for a 100 mM buffer solution with a maximum pH of 8. The development of the internal pH depending on the pH of the applied buffer can be followed in Figure 3.5 d). Carboxylic groups show similar behavior, but with a less pronounced effect. Cyanide, being a weak Lewis-base, did not show a strong impact

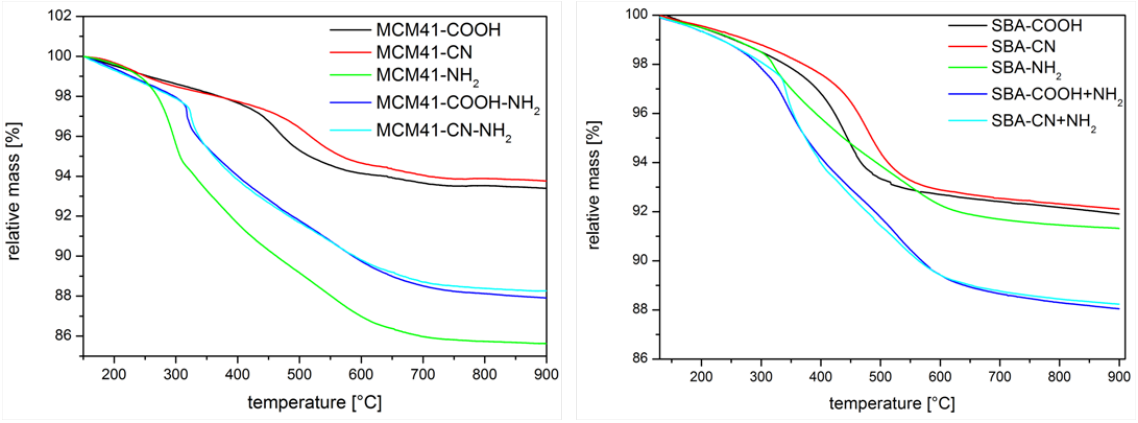

Figure 3.3: TGA curves for differently functionalized samples MCM-41 (left) and SBA-15 (right)

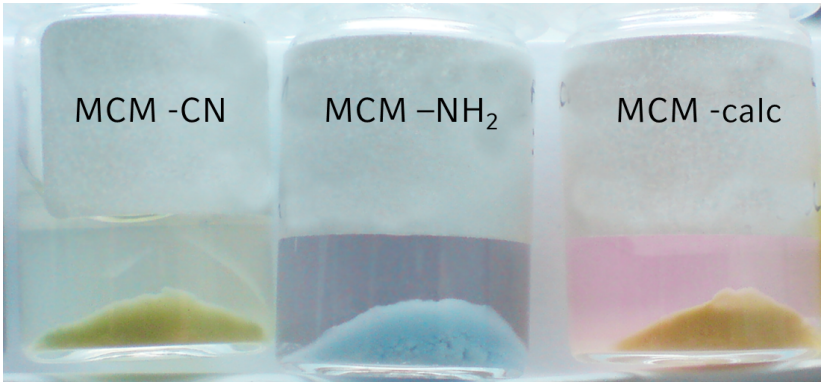

Figure 3.4: Different pore-modifications led to differently colored particles upon indicator dye absorption from water, indicating different internal pore pH values.

on the internal pH. Immobilization of basic amino residues led to opposite effects compared to those observed for carboxylic residues. The slight shift of cyano- and amino-functionalized pores towards acidic pH could be attributed to the presence of silanol groups. Furthermore, the creation of an internal buffer system through the simultaneous incorporation of carboxy and amino functionalities led to a pH region between 5.5 and 7.5. With diminishing ionic strength of the buffer, the effect on the pH in the mesopores decreased (Figure 3.5 b) and e).

Using a 1 mM buffer, almost no response of the internal pore-pH on the variation of buffer-pH could be monitored for calcined, carboxy-, amino- and cyano:amino 1:1-functionalized samples. Only cyano- and carboxy:amino 1:1-modified particles

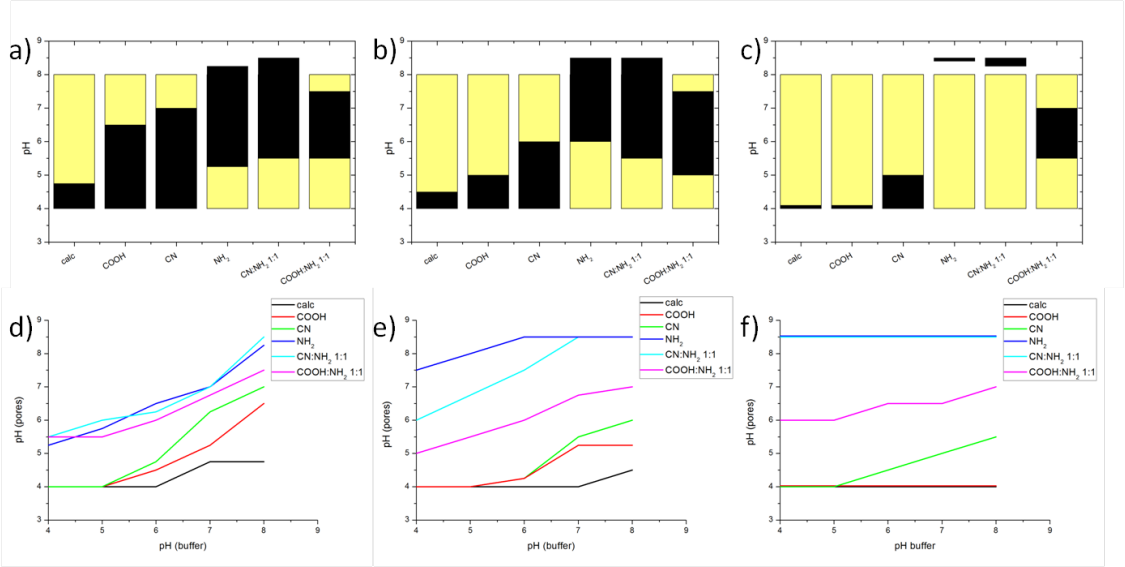

Figure 3.5: Results of the pH determination in MCM-41. a-c: Pore pH regions (black bars, corresponding to ΔpH (pores) in d-f) for different buffer solutions (yellow bars, corresponding to ΔpH (buffer) in d-f, always 4-8). a) Mc Ilvaine buffer 100 mM, b) Mc Ilvaine buffer 10 mM, c) Mc Ilvaine buffer 1 mM, d-f: Precise data of the measurements from which the bar diagrams were prepared. d) Mc Ilvaine buffer 100 mM, e) Mc Ilvaine buffer 10 mM, f) Mc Ilvaine buffer 1 mM.

showed variations in pH. In the latter case, this effect can be explained with the fact that ammonium acetate buffer systems do not show buffer capacity in the region around pH 6. A remarkable effect was observed for amino-functionalized pores, as the internal pH-region was above the pH-region given by the buffer solution. Every trend discovered for different modifications of the narrow pore host MCM-41 can be transferred to SBA-15 (Figure 3.6). The only difference is the spread of the black bars, which indicates that the effect of pore-wall functionalization decreases with increasing pore-size.

Impact of the pore-functionalization on the activity of immobilized catalytic centers

For the immobilization of sp-trypsin, SBA-15 was modified with functional groups at a ratio of -X:N_3 = 100:1 (X = COOH, NH_2). Activity measurements were performed with a previously described photometric assay.[10] The amounts of immobi-

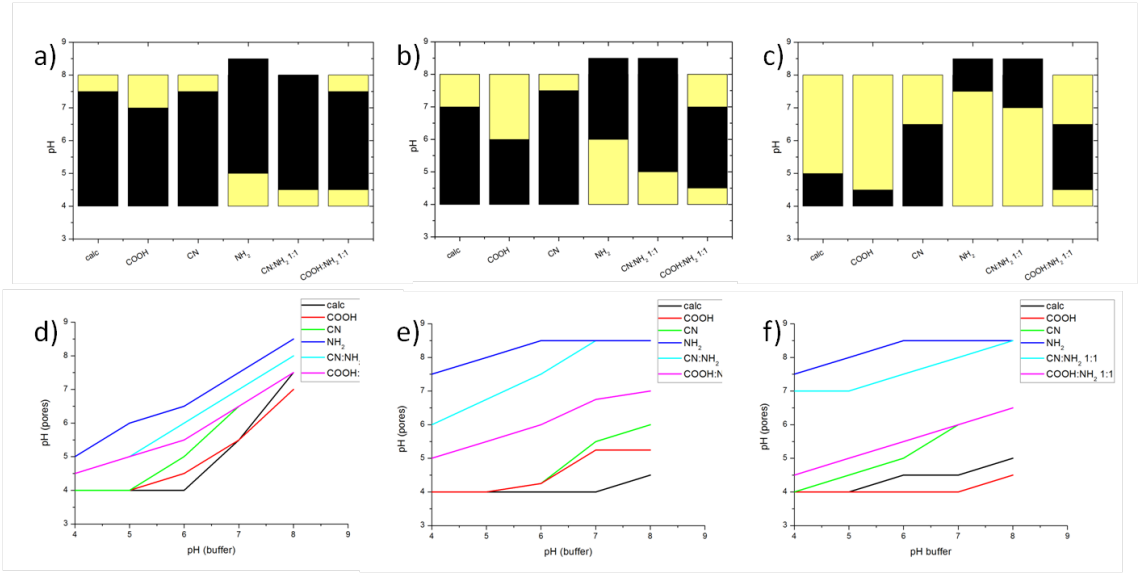

Figure 3.6: Results of the pH determination in SBA-15. a-c: Pore pH regions (black bars, corresponding to ΔpH (pores) in d-f) for different buffer solutions (yellow bars, corresponding to ΔpH (buffer) in d-f, always 4-8). a) Mc Ilvaine buffer 100 mM, b) Mc Ilvaine buffer 10 mM, c) Mc Ilvaine buffer 1 mM, d-f: Precise data of the measurements from which the bar diagrams were prepared. d) Mc Ilvaine buffer 100 mM, e) Mc Ilvaine buffer 10 mM, f) Mc Ilvaine buffer 1 mM.

lized trypsin were determined by TGA measurements (Figure 3.7). Data were taken at 900 °C according to Schlossbauer *et al.*.[10]

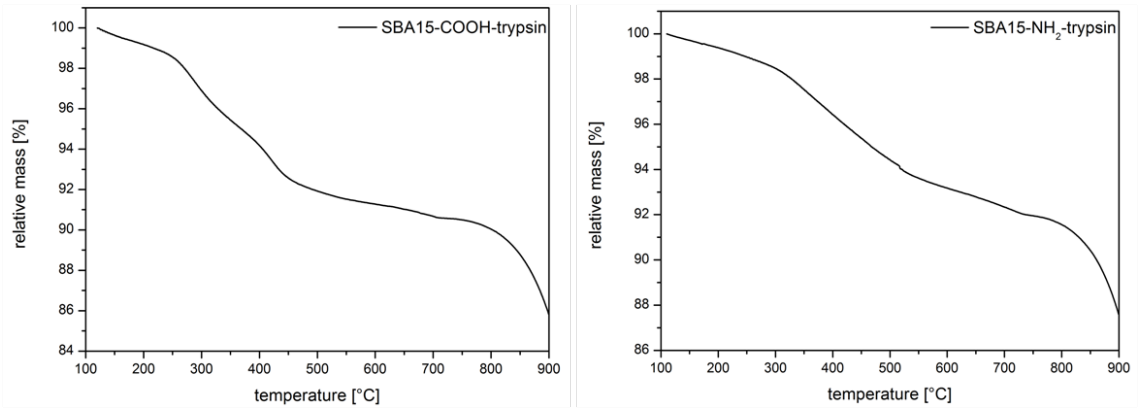

Figure 3.7: TGA data obtained for SBA15-COOH-trypsin (left) and SBA15-NH_2-trypsin (right)

Activity values obtained for differently modified samples are presented in Table 3.1. Activity measurements revealed that the incorporation of acidic groups led to a loss in activity of about 50% compared to unfuntionalized SBA-15-trypsin, whereas an in-

crease by 296% could be obtained through the incorporation of basic amino-moieties. Free trypsin has an optimal operating pH of approximately 8.[30] The internal pH of the mesopores could be increased through the grafting of amino-groups, and thus, enhanced activity was detected. In the case of amino-functionalization, activity measurements showed that maximum activity was obtained for a slightly acidic buffer solution (pH 6), whereas for carboxy-modified particles, even at pH 8, the samples showed very low activity.

Table 3.1: Results of trypsin activity tests.

Sample	Activity [U*/mg trypsin]	pH optimum**
Trypsin	346[10]	7.5
SBA-15-trypsin	65.6[10]	n.d.
SBA-15-COOH-trypsin	32	8
SBA-15-NH_2-trypsin	194	6

* 1 Unit = amount of enzymatic activity releasing 1 μmol of $N\alpha$-p-tosyl-L-arginine per minute

** determined with 100 mM McIlvaine's buffer solutions

To study the impact of pore-wall-modification on the activity of a molecular catalyst, hemin, the catalytic center of horse radish peroxidase, was attached in the pores of azide-functionlized MSN-nanoparticles. In a first step, hemin was reacted with 4-pentynoic acid in an amidation step to give sp-hemin. Sp-hemin was grafted to the pore walls of the particles via click-chemistry (MSN-hemin). MSN-hemin was further functionlized by an additional click reaction with 4-pentynoic acid or propargylamine to give MSN-COOH-hemin and MSN-NH_2-hemin. Activity values obtained for differently modified samples are presented in Table 3.2. Similar results compared to the enzymatic catalyst trypsin were obtained for the molecular catalyst hemin. In the case of hemin, an increase by 30 % in activity could be obtained for

the additional functionalization with acidic moieties, whereas a reduction to 39% residual activity was found for amino-groups, compared to MSN-hemin (Table 2). In contrast to trypsin, no change in the external pH-optimum could be observed. Strikingly through immobilization, the activity of hemin increased 62 times for MSN-COOH-hemin compared with free hemin.

Table 3.2: Results of hemin activity tests.

Sample	Activity $[\Delta n^*/mg\ hemin]\cdot 10^{-5}$	pH optimum**
Hemin	0.3	6
MSN-hemin	14.6	5-6
MSN-COOH-hemin	19.0	5-6
MSN-NH_2-hemin	5.73	5-6

* Δ = amount [mmol] of dye released by 1 mg hemin per second

** determined with 200 mM McIlvaine's buffer solutions

3.4 Conclusions

In summary, we present the impact of pore-wall modifications on the internal pH of mesoporous silica systems. We could show that depending on the nature of inner functionality, the pH inside the pores differs significantly from the pH in an outer buffer solution. In these systems, stronger effects could be observed for smaller pore diameters, as the amount of functionality per pore volume increases. When reducing the ionic strength and thus the buffer capacity of the external buffer solutions, the internal pH controlled through the pore-modifications becomes progressively dominant. The concept of pH-control via pore-wall-functionalization was examined with two different catalytic systems. Both showed strong dependence of the catalytic activity on the pore-modification, whereas an impact on the pH-optimum of the

external buffer could only be observed for the enzymatic catalyst trypsin. Our results lead to a better understanding of catalyst-pore-wall interactions. We conclude that the control of pH-values in confined nanospaces such as mesopores can lead to striking increases in the performance of encapsulated bio-inorganic catalyst systems.

3.5 Appendix

Nitrogen sorption

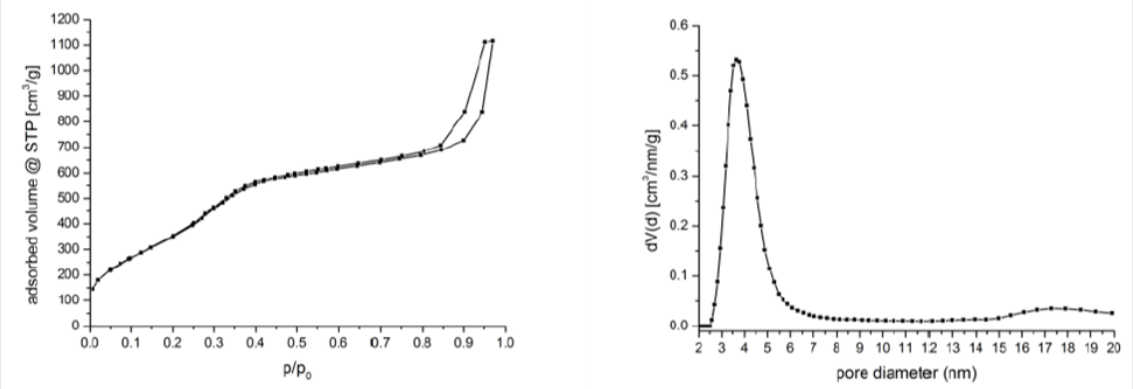

Figure 3.8: Nitrogen sorption isotherm (left) and calculated DFT pore size distribution (right) for MSN-N_3

TGA data of functionalized MCM-41 and SBA-15

Table 3.3: TGA data obtained for MCM-41

Sample	Mass loss [%] at 900 °C	m(org. residue) [mg/g_{MCM-41}]	n(org. residue) [mmol/g_{MCM-41}]
MCM-41-COOH	6.6	70.7	1.0
MCM-41-CN	6.2	66.1	1.2
MCM-41-NH_2	14.4	168	2.9
MCM-41-CN-NH_2	11.7	133	2.3
MCM-41-COOH-NH_2	12.1	138	2.1

Table 3.4: TGA data obtained for SBA-15

Sample	Mass loss [%] at 900 °C	m(org. residue) [mg/g_{SBA-15}]	n(org. residue) [mmol/g_{SBA-15}]
SBA-15-COOH	8.0	87.0	1.2
SBA-15-CN	7.9	85.8	1.6
SBA-15-NH_2	8.7	95.3	1.6
SBA-15-CN-NH_2	11.8	134	2.4
SBA-15-COOH-NH_2	12.0	136	2.0

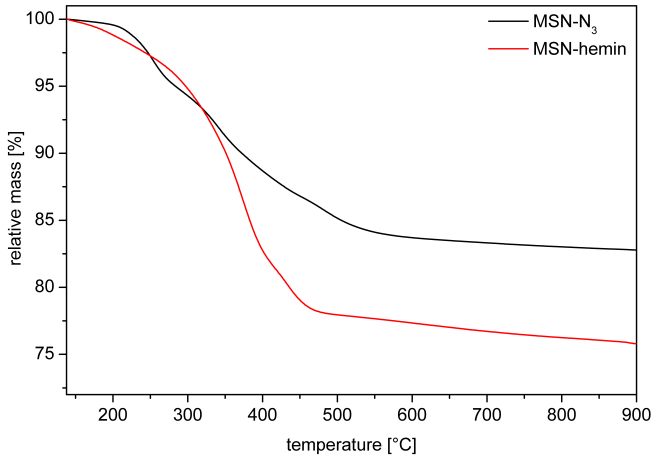

Figure 3.9: TGA data obtained for MSN-N_3 (black) and MSN-hemin (red)

Trypsin activity

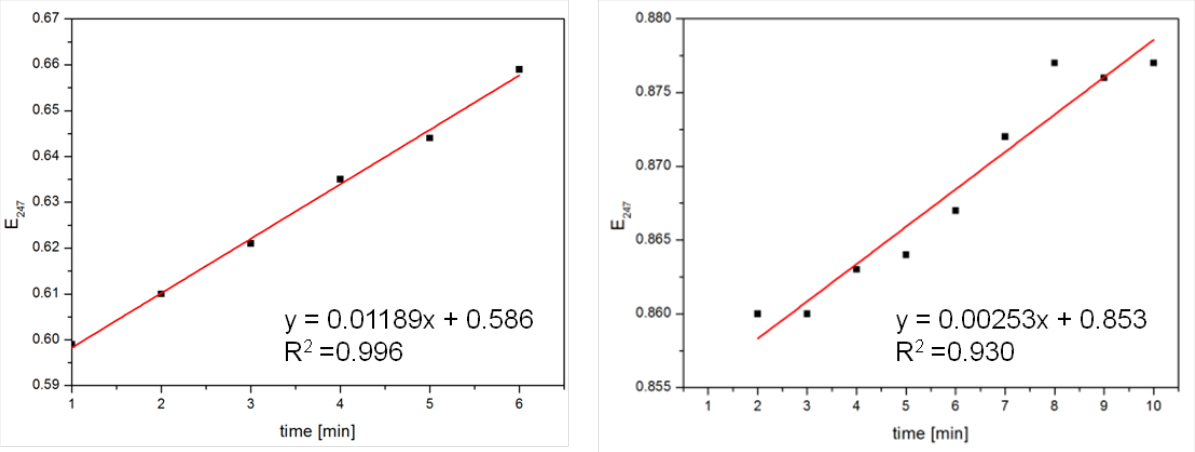

Figure 3.10: Activity determinations of (left) SBA-NH_2-trypsin and (right) SBA-COOH-trypsin.

Table 3.5: Calculation of trypsin activity in functionalized SBA-15

	SBA-15-NH_2-trypsin	SBA-15-COOH-trypsin
ΔE_{247} [1/min]	0.01189	0.00253
E_w [mg]	0.000170	0.000216
$U/mg_{trypsin}$ [μmol/min]	194	32.6

Hemin activity

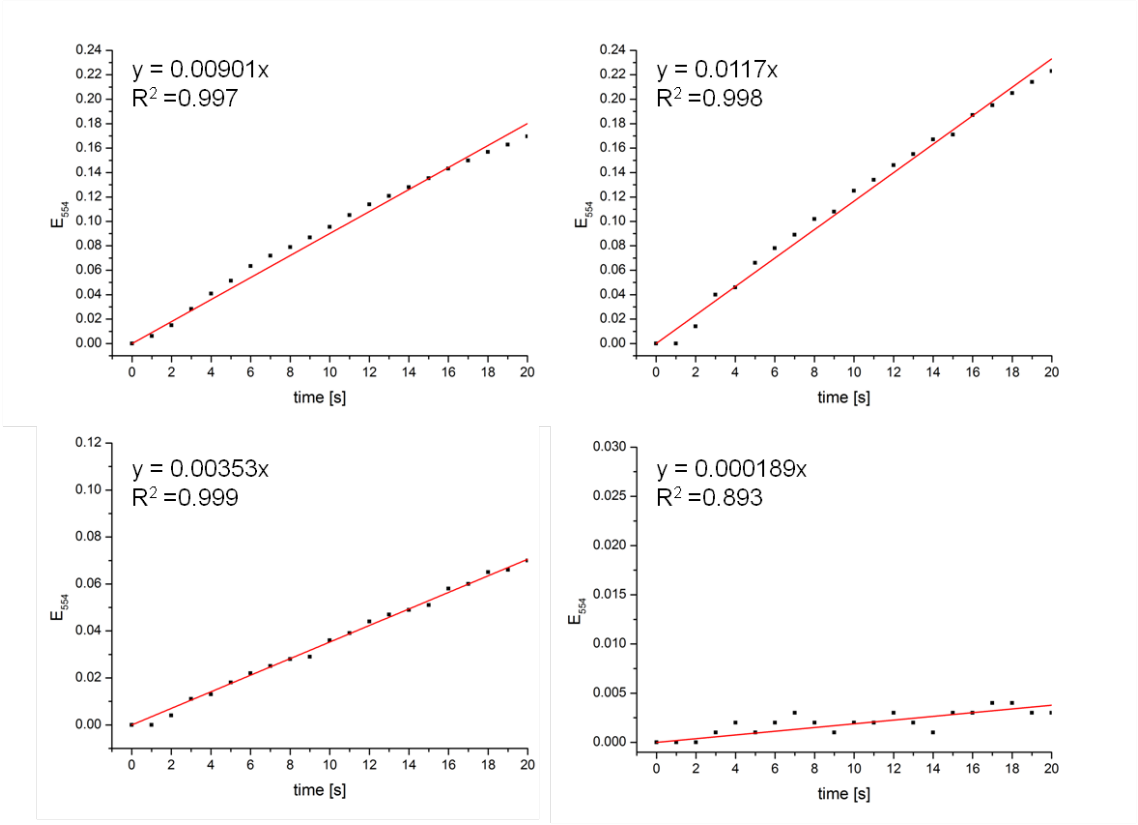

Figure 3.11: Activity determinations of MSN-hemin (top left), MSN-COOH-hemin (top right), MSN-NH_2-hemin (bottom left) and free hemin (bottom right).

Table 3.6: Calculation of hemin activity in functionalized MSNs

	MSN-hemin	MSN-NH_2-hemin	MSN-COOH-hemin	Hemin
ΔE_{554} [1/s]	0.00901	0.00353	0.00117	0.000189
m_{hemin} [μg]	3.7	3.7	3.7	3.7
$\Delta n/mg_{hemin} \cdot 10^{-5}$ [$mmol/s$]	14.6	5.73	19.0	0.307

Bibliography

[1] Argyo, C., Cauda, V., Engelke, H., Rädler, J., and Bein, T. *Chemistry - A European Journal* **18**, 428 (2012).

[2] Hartmann, M. *Chemistry of Materials* **17**(18), 4577–4593 (2005).

[3] Sauer, A. M., Schlossbauer, A., Ruthardt, N., Cauda, V., Bein, T., and Bräuchle, C. *Nano Letters* **10**(9), 3684–3691 (2010).

[4] Schlossbauer, A., Warncke, S., Gramlich, P., Kecht, J., Manetto, A., Carell, T., and Bein, T. C. *Angewandte Chemie International Edition* **49**(28), 4734–4737 (2010).

[5] Ispas, C., Sokolov, I., and Andreescu, S. *Analytical and Bioanalytical Chemistry* **393**, 543–554 (2009).

[6] Li, Z., Barnes, J. C., Bosoy, A., Stoddart, J. F., and Zink, J. I. *Chemical So* **41**, 2590–2605 (2012).

[7] Bornscheuer, U. T. *Angewandte Chemie International Edition* **42**(29), 3336–3337 (2003).

[8] Diaz, J. F. and Balkus Jr, K. J. *Journal of Molecular Catalysis B: Enzymatic* **2**(2), 115–126 (1996).

[9] Lee, C.-H., Lang, J., Yen, C.-W., Shih, P.-C., Lin, T.-S., and Mou, C.-Y. *The Journal of Physical Chemistry B* **109**(25), 12277–12286 (2005).

[10] Schlossbauer, A., Schaffert, D., Kecht, J., Wagner, E., and Bein, T. *Journal of the American Chemical Society* **130**(38), 12558–12559 (2008).

[11] Vinu, A., Murugesan, V., Tangermann, O., and Hartmann, M. *Chemistry of Materials* **16**(16), 3056–3065 (2004).

[12] Yiu, H. H. P., Wright, P. A., and Botting, N. P. *Journal of Molecular Catalysis B: Enzymatic* **1**(13), 81–92 (2001).

[13] Hartmann, M., Vinu, A., and Chandrasekar, G. *Chemistry of Materials* **17**(4), 829–833 (2005).

[14] Jung, D., Streb, C., and Hartmann, M. *Microporous and Mesoporous Materials* **113**(1-3), 523–529 (2008).

[15] Vinu, A. and Hartmann, M. In *Studies in Surface Science and Catalysis,* E. van Steen, M. C. and Callanan, L. H., editors, volume Volume 154, Part C, 2987–2994. Elsevier (2004).

[16] Vinu, A., Murugesan, V., Tangermann, O., and Hartmann, M. *Chemistry of Materials* **16**(16), 3056–3065 (2004).

[17] Kim, M. I., Kim, J., Lee, J., Shin, S., Na, H. B., Hyeon, T., Park, H. G., and Chang, H. N. *Microporous and Mesoporous Materials* **111**(1-3), 18–23 (2008).

[18] Hudson, S., Cooney, J., Hodnett, B. K., and Magner, E. *Chemistry of Materials* **19**(8), 2049–2055 (2007).

[19] Rosales-Hernandez, M., Mendieta-Wejebe, J., Correa-Basurto, J., Vazquez-Alcantara, J., Terres-Rojas, E., and Trujillo-Ferrara, J. *International Journal of Biological Macromolecules* **40**(5), 444 – 448 (2007).

[20] Yang, X.-Y., Li, Z.-Q., Liu, B., Klein-Hofmann, A., Tian, G., Feng, Y.-F., Ding, Y., Su, D. S., and Xiao, F.-S. *Advanced Materials* **18**(4), 410–414 (2006).

[21] Zhang, B. P., Janicke, M. T., Woodruff, W. H., and Bailey, J. A. *The Journal of Physical Chemistry B* **109**(42), 19547–19549 (2005).

[22] Craik, C., Roczniak, S., Largman, C., and Rutter, W. *Science* **237**, 909–913 (1987).

[23] Nakazawa, J. and Stack, T. D. P. *Journal of the American Chemical Society* **130**(44), 14360–14361 (2008).

[24] Grün, M., Unger, K. K., Matsumoto, A., and Tsutsumi, K. *Microporous and Mesoporous Materials* **27**(2-3), 207 – 216 (1999).

[25] Katiyar, A., Yadav, S., Smirniotis, P. G., and Pinto, N. G. *Journal of Chromatography A* **1122**, 13–20 (2006).

[26] Gole, A. and Murphy, C. J. *Langmuir* **24**(1), 266–272 (2008).

[27] Cauda, V., Schlossbauer, A., Kecht, J., Zürner, A., and Bein, T. *Journal of the American Chemical Society* **131**(32), 11361–11370 (2009).

[28] Huang, Y., Cai, R., Mao, L., Liu, Z., and Huang, H. *Analytical Sciences* **15**(9), 889–894 (1999).

[29] Hummel, B. C. W. *Canadian Journal of Biochemistry and Physiology* **37**(12), 1393–1399 (1959).

[30] Sipos, T. and Merkel, J. R. *Biochemistry* **9**(14), 2766–2775 (1970).

Chapter 4

Lipid-bilayer Coated Nanosized Bimodal Mesoporous Carbon Spheres for Controlled Release Applications

The following work is based on a project with Benjamin Mandlmeier, Alexandra Schmidt, Jörg Schuster and Thomas Bein

4.1 Introduction

Colloidal mesoporous carbon particles feature several properties that make them attractive candidates for controlled release and possibly drug delivery applications. These properties include high surface areas and pore volumes resulting in high loading capacities and good dispersibility. Additionally carbon can be equipped with various chemical functionalities, which are often required to create more complex systems. Up to now, important systems explored in targeted drug delivery are based on mesoporous silica,[1] liposomes,[2,3] and polymers.[4–7] Different porous carbon morphologies, such as activated carbon particles,[8,9] carbon nanotubes (CNTs)[9–13] and ordered mesoporous carbon (CMK-3),[14] loaded with certain compounds and

exhibiting good biocompatibility[15,16] have been reported in the context of drug delivery. Combining magnetic properties with carbon nanostructures is also being discussed for medical applications.[17] Nevertheless, certain carbon nanomaterials such as multi-walled CNT, carbon fibers and certain types of particles (carbon black) can lead to cytotoxic effects depending on their size, aspect ratio and surface chemistry.[18] Another study showed that functionalization of CNTs reduced toxic effects to the cytosol.[19] Several reports describe the formation of mesoporous carbon for drug delivery by replicating silica hard templates. Zhu *et al.* showed the functionalization of mesoporous carbon with a thermoresponsive polymer.[14] Based on this work, spherical mesoporous carbon in the size range of 500-800 nm was recently prepared, exhibiting a BET surface area of 1069 m^2/g and high pore volume of 1.49 cc/g, with a pore diameter of 6.0 nm.[19] Many approaches for the preparation of mesoporous carbons are known,[20] and the morphology can be controlled by the dimensions of hard templates. For example, MCM-48 silica particles were used as template for ordered mesoporous carbon (CMK-1).[21] Furthermore mesoporous carbon nanoparticles (MCNs) were applied in drug delivery experiments providing a high BET surface area of 2034 m^2/g and a pore volume of 1.2 cc/g.[22] Also hydrophilic amino-functionalized MCNs in the range of 100 to 150 nm were obtained and their high drug storage capacity was attributed to a BET surface area of 1309 m^2/g and a pore volume of 0.9 cc/g (with small pores below 3 nm).[23] A high biocompatibility was shown for mesoporous carbon nanoparticles hydrothermally derived from resol as carbon source and the block-copolymer Pluronic F127.[16] With this approach particle sizes were obtained from ca. 20 to 140 nm, but the highest BET surface area of 1131 m^2/g was accompanied by a small pore size of 2.6 nm for 90 nm large particles. The influence of the particle size on endocytosis was demonstrated with MCNs having small diameters of around 90 nm.[24] These samples were prepared by a hydrothermal route, using the block co-polymer Pluronic F127 as soft-template, resulting in particles with a BET surface area of 746 m^2/g, a pore volume of 0.76 cc/g, and a pore size of 2.7 nm. A novel general route for ordered mesoporous carbon (OMC) with high porosity involves a concerted co-assembly of

carbon and silica precursors with Pluronic F127 and successive template removal after full carbonization, providing a bimodal pore size distribution.[25] Based on this method, we recently reported dispersible and porous carbon spheres (sized about 330 nm) using macroporous silica as hard template.[26] Those MCNs provided the highest inner pore volumes for mesoporous carbon nanoparticles of 2.32 cc/g and also one of the highest surface areas of 2445 m^2/g with a bimodal pore size distribution of large and small mesopores of 6 nm and 3.1 nm. Those properties make them attractive candidates for drug delivery applications. In this study we report the synthesis of very small mesoporous carbon nanospheres with extremely high porosity and present the first efficient cap system for colloidal mesoporous carbon nanospheres (Figure 4.1).

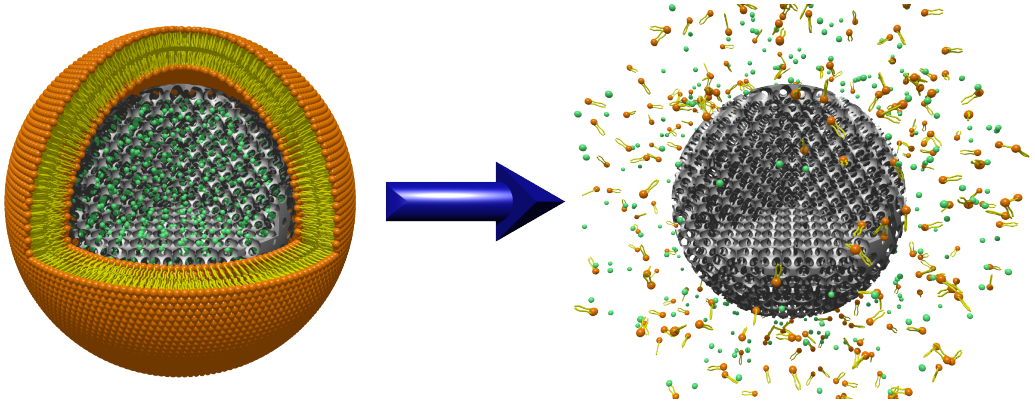

Figure 4.1: Surfactant induced release of calcein (green) from mesoporous carbon nanoparticles encapsulated by a supported lipid bilayer.

We synthesized very small mesoporous carbon nanospheres with diameters ranging from 45 to 70 nm using a macroporous silica hard template providing appropriate dimensions. Our particles feature a very high BET surface area of 2003 m^2/g and a high pore volume of 1.95 cc/g. To the best of our knowledge this is the highest specific pore volume for mesoporous carbon nanoparticles at a size below 100 nm and also one of the highest surface areas. Additionally a bimodal porosity with maxima at 5.9 and 3.1 nm was achieved by removal of F127 from the pores and silica from the walls. Here we combine an extremely high loading capacity and

very suitable particle sizes for an improved cell uptake. The use of supporting lipid bilayers (SLBs) as cap systems has been successfully demonstrated for mesoporous silica nanoparticles.[26–32] Being a very simple imitation of a cell membrane, SLBs can enhance circulation times and accumulation in tumor tissue as reported for the delivery of doxorubicin.[33] Compared to liposomes, the solid nanoparticle core offers two major advantages. First, narrow size distributions and second, enhanced stability in comparison with liposomes can be achieved.[29,30,34,35] Therefore we transferred the concept of SLBs to mesoporous carbon and present the first efficient cap system for colloidal mesoporous carbon nanospheres. Efficient sealing of the mesopores could be obtained by coating each carbon sphere with an SLB. Regarding the lipid formulation, we used a mixture of cationic and neutral lipids (DOTAP and DOPC) and 60 nm NCS. To demonstrate the effectiveness of our cap-system, the controlled release of calcein was studied *in vitro* by fluorescence spectroscopy.

4.2 Experimental Section

Chemicals

Sodium dodecyl sulfate, potassium persulfate, ammonium persulfate, methyl methacrylate (99%), tetraethyl orthosilicate (technical grade), concentrated HCl (37% in water), sodium hydroxide, Pluronic F127, Calcein, Triton X-100, sulfuric acid and organic solvents were obtained from Aldrich and used without further purification. Formalin (37 wt% formaldehyde in water) and phenol was purchased from Merck KGaA and Pluronic F127 from BASF AG. Used lipids: DOPC (1,2-dioleoyl-sn-glycero-3-phosphocholine, Avanti Polar Lipids), DOTAP (1,2-dioleoyl-3-trimethylammonium-propane, Avanti Polar Lipids).

Synthesis of PMMA spheres

PMMA spheres of about 60 nm were prepared by a modified route reported elsewhere.[36] The emulsion polymerization was started by adding a solution of 227.2 mg potassium persulfate ($K_2S_2O_8$, 0.84 mmol) in 2 mL water to a mixture of 27.56 g

methyl methacrylate (MMA, 275.3 mmol), 196 mg sodium dodecyl sulfate (SDS, 0.68 mmol) in 98 mL water at 70 °C. Previously the water was degassed by flushing with nitrogen for 1 h, before SDS and MMA were added and the mixture was then stirred under refluxing conditions for 1 h at 70 °C. After 2 h of polymerization the reaction was stopped by external cooling and applying air to the three-bottleneck flask (250 mL). The resulting colloidal solution was washed three times with water by centrifugation at 20500 rpm (50228 rcf) for 30 min. This solution was dried in plastic petri dishes for several days and the resulting flakes of several mm in size were dried at 80 °C for 2 h.

Synthesis of macroporous silica

For the synthesis of the macroporous silica the obtained PMMA flakes were collected on a filter paper and cast multiple times with a hydrolyzed silica precursor solution. The residual solution was removed by applying vacuum to the Büchner funnel. For the silica solution, 12 mL tetraethyl orthosilicate (TEOS, 53.8 mmol) were added to 8 mL ethanol under stirring. To the clear solution 6 mL water and 1 mL concentrated hydrochloric acid (HCl, 37%) were dropped and stirred for another 10 min at room temperature.[26] Finally, the PMMA/SiOx composite was calcined in air at 550 °C for 5 h (ramp: 1 °C/min).

Synthesis of mesoporous carbon spheres

For this purpose a mixture of resol precursor as carbon source, and silica precursor were used for casting the previously prepared macroporous silica template. The resol precursor was prepared according to Meng et al.[37] Here, 21 g formalin (37 wt% formaldehyde in water, 0.259 mol) was added dropwise at 50 °C to a solution of 12.2 g phenol (0.128 mol) and 2.6 g of 20 wt% sodium hydroxide solution (0.013 mol). The final solution was than heated for 1 h at 75 °C and cooled to room temperature. After neutralizing the basic solution using hydrochloric acid (1 M), water was removed by rotary evaporation. The resulting product was diluted in absolute ethanol to achieve a solution of 20 wt% (resol precursor). For the final

casting solution, 2.0 g of Pluronic F127, 20.0 g of ethanol, and 2.0 g of 0.2 M HCl were mixed well at 40 °C. Then 4.16 g TEOS and 5.0 g of the 20 wt% resol solution were added.[25] The resulting yellow solution was stirred for another 5 h at the same temperature. Typically, 10 g of the solution were cast on 100 mg of the macroporous silica template, and the evaporation of the solvents and self-assembly of the F127 occurred at room temperature in an open Petri dish during 2-3 days. The resulting and filled flakes were collected and thermopolymerized in air at 100 °C for 24 h, followed by carbonization at 900 °C in a stream of nitrogen. Here, the material was heated first to 350 °C (rate: 1 °C/min; dwell time: 3 h), then to 600 °C (rate: 1 °C/min) and finally to 900 °C (rate: 5 °C/min; dwell time: 2 h). The resulting shiny black bulk material was additionally treated with aqueous hydrofluoric acid (10 wt%) for 2 days, to remove silica from the macroporous template and from walls of the mesoporous carbon phase. This treatment was followed by filtering and threefold washing with water (MilliporeQ) and absolute ethanol.

Oxidation of nanosized mesoporous carbon spheres

To obtain a colloidal suspension of carbon spheres, the bulk material was oxidized in a mixture of ammonium persulfate and sulfuric acid.[38] Specifically, 30 mg NCS were added to a mixture of 2.4 g ammonium persulfate in 4 mL sulfuric acid (1 M). The resulting suspension was stirred for 24 h at room temperature. Subsequently, the particles were washed 5 times by centrifugation (14000 rpm, 16873 rcf, 8 min) and redispersion in 5 mL MilliporeQ water.

Preparation of SLB@NCS loaded with calcein

The amount of 1 mg oxidized colloidal mesoporous carbon was dispersed in 500 μL of an aqueous solution of calcein (1 mM) and stirred (500 rpm) for 2 h at room temperature in the dark. After centrifugation (14000 rpm, 16873 rcf, 8 min), 100 μL of a premixed lipid solution (70 μL DOPC + 30 μL DOTAB, each 2.5 mg/mL in a mixture of 40 %v EtOH / 60 %v water) were added. Upon addition of 700 μL of MilliporeQ water, the formation of a supported lipid bilayer on the external surface

of NCS was induced. The SLB@NCS were then centrifuged and redispersed in 800 μL MilliporeQ water, to eliminate unsupported lipids and ethanol.

***In vitro* release experiment**

An amount of 200 μL of the aqueous suspension containing SLB@NCS loaded with calcein was transferred into a tube which could be closed with a dialysis membrane (with a molecular-weight cutoff of 16000 g/mol).[39] This custom made cap fits on the opening of a fluorescence cuvette, filled with MilliporeQ water. Only the fluorescent molecules are able to diffuse through the dialysis membrane, whereas the NCS material stays entrapped in the cap and is not able to enter the cuvette, where the dye molecules are detected by fluorescence spectroscopy. For the delivery experiment, a time-based measurement with an excitation wavelength of 495 nm and an emission wavelength of 517 nm was recorded. The dye-loaded sample was monitored in the closed state up to 4 h, showing no significant release of the dye molecules. After the addition of 5 μL Triton X-100 (1:1000 v/v in H_2O) into the tube containing the SLB@NCS, the lysis of the lipids from the NCS nanoparticles allowed the diffusion of calcein out of the pores through the dialysis membrane and their detection in the cuvette. The release in the open state was monitored for additional 3 h.

4.3 Results and Discussions

Three-dimensionally ordered macroporous (3DOM) silica, which was further used as hard template, was prepared by replicating an array of close-packed PMMA spheres. PMMA spheres were prepared by emulsion polymerization. The washed particles were dried in petri dishes at room temperature to obtain millimeter sized bulk material. Figure 4.2 a represents an SEM image of an ordered domain of packed PMMA spheres with diameters of around 75 - 80 nm. These PMMA templates were collected, and cast several times with a prehydrolyzed TEOS precursor solution, to achieve a complete filling of the interstitial voids. The resulting PMMA/SiO_x

composite was dried for several hours and calcined at 550 °C to solidify the silica precursor and to remove the PMMA template. The resulting pore diameter is ranging between ca. 60 - 70 nm, which is smaller than the initial size of the PMMA spheres and can be attributed to heating-induced shrinkage.[40,41] The bulk material shows a good accessibility of the pores through random interpore connections in the range of about 20 nm. A rough silica surface was attributed to the loose initial packing of the PMMA spheres. The random orientation is also presented by a diffuse ring, obtained by the Fast Fourier Transform (inset) of the rectangular area (white). The diffuse ring indicates a d-spacing of around 70 nm, which is slightly smaller than the lattice spacings of the PMMA template (Figure 4.2 b).

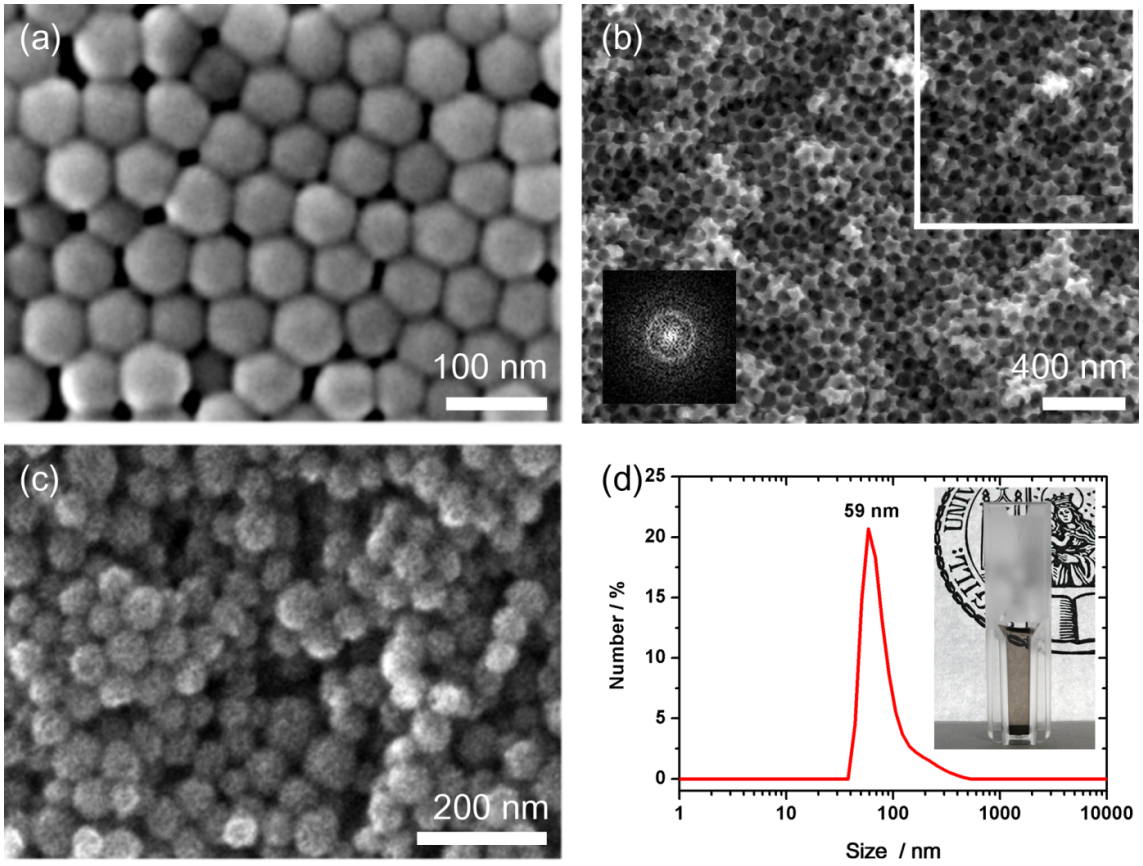

Figure 4.2: SEM images of (a) the PMMA colloidal crystal template before TEOS impregnation, (b) the corresponding randomly ordered (FFT inset) macroporous silica replicate after calcination at 550 °C (inset: a 2D fast Fourier transform (FFT) of the white square) and (c) bimodal mesoporous carbon spheres after carbonization at 900 °C in nitrogen and final removal of silica residues by HF treatment. (d) DLS and photograph (inset) depict a homogeneous size distribution of the spheres in solution.

This macroporous silica was further used as hard template for the synthesis of bimodal mesoporous carbon spheres. As carbon source we used resol, which was co-assembled with two porogen compounds, TEOS and Pluronic F127. This precursor mixture enables a homogeneous dispersion of TEOS within the walls of the carbon mesostructure during an evaporation-induced self-assembly (EISA), occurring during the casting and drying of the precursor within the empty voids of the macroporous silica hard template. Subsequent thermopolymerization at 100 °C for 24 h and carbonization at 900 °C in nitrogen results in full carbonization and conversion of TEOS into silica, dispersed in the walls of the mesoporous network. Simultaneously the total removal of Pluronic F127 is responsible for mesopore formation. All silica residues were successfully etched with hydrofluoric acid (10 wt%), which creates a loose packing of nanosized mesoporous carbon (NCS) particles in the range of 45 to 68 nm (Figure 4.2 c). The particles can be separated either by oxidation with ammonium persulfate or ultrasound treatment, leading to well-dispersed colloidal suspensions (Figure 4.2 d, photograph). The DLS measurement shows a maximum size of 59 nm, which is consistent with the SEM data.
The obtained NCS were also characterized by STEM-HAADF (Figure 4.3 a, b), demonstrating their uniform particle size. The very small carbon spheres feature a rough surface with accessible mesopores and smaller ones that are present in the walls. The pore structure seems to be ordered and regarding the small-angle X-ray scattering (Figure 4.6) a d-spacing of around 8.8 nm for the NCS particles was found. The broad reflection indicates a disturbed long range order, which we attribute to a relatively small confined size within this macroporous template. In contrast, we previously found a pronounced highly ordered hexagonal phase within carbon spheres having diameters of around 330 nm.[26]

From nitrogen sorption measurements (Figure 4.3 c) a type IV isotherm was obtained, showing a wide hysteresis and no defined saturation at high relative pressures. We attribute this to a pronounced textural porosity between the particles. A high BET surface area of 2003 m^2/g and a high total pore volume of 1.95 cc/g were

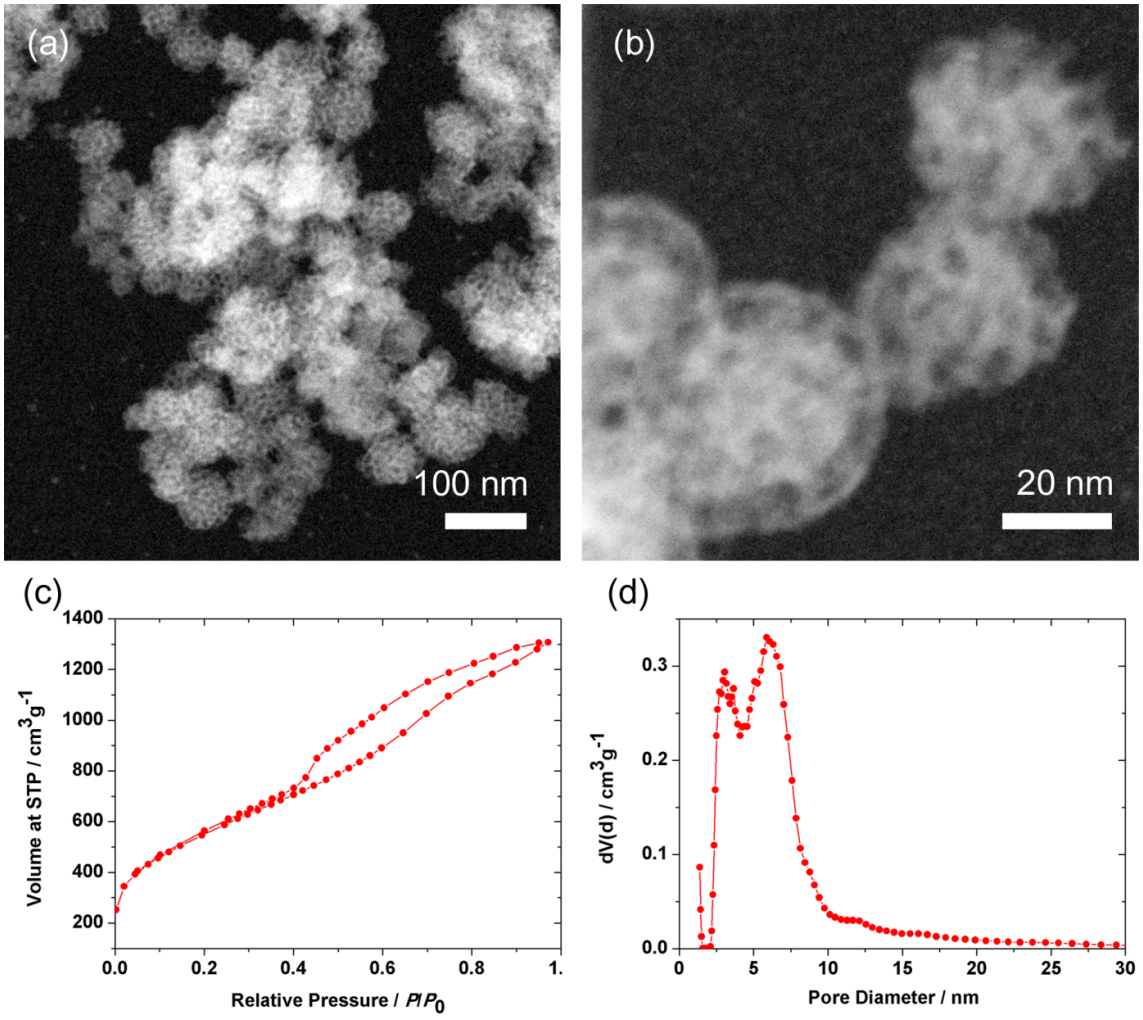

Figure 4.3: (a, b) STEM-HAADF images of mesoporous NCS particles at different magnifications, obtained after HF treatment. Nitrogen sorption measurements reveal a type IV isotherm (c) and a bimodal pore size distribution (b).

achieved. The bimodal porosity, resulting from the removal of F127 and silica from the walls, exhibits two maxima at 5.9 and 3.1 nm, respectively. These properties suggest that these small mesoporous particles are attractive candidates for introducing chemical functionality and for applications as potential drug delivery system. For the creation of an SLB@NCS system, the hydrophobic particle surface had to be oxidized. Here we used a procedure already known in the literature.[38] The successful oxidation of NCS in a solution of ammonium persulfate in sulfuric acid is shown by IR spectroscopy (Figure 4.4). The two peaks arising at 1725 cm^{-1} and 1618 cm^{-1} can be attributed to carbonyl (carboxylic acid and keto-groups)

and hydroxyl groups formed during the oxidation process (black curve). This negatively charged surface can now interact with the positively charged head groups of the phospholipids, which facilitates the formation of an SLB around the NCS. To show the potential of SLB@NCS as a release-on-demand system, we demonstrate that the SLB is able to prevent any premature release of dye molecules out of the mesostructure.

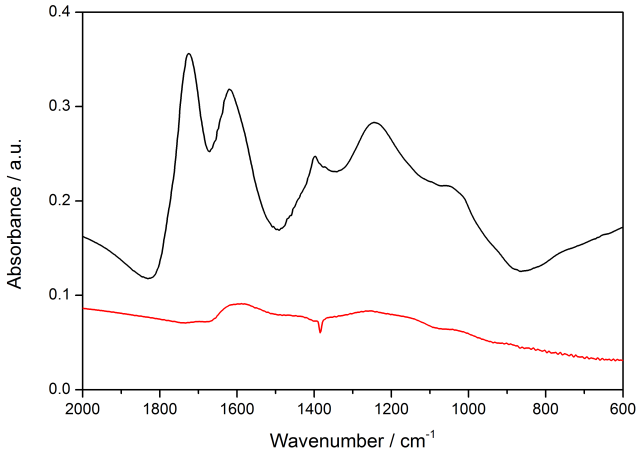

Figure 4.4: Infrared spectroscopy of as synthesized (red) and oxidized NCS (black).

For this purpose, we loaded a fluorescent dye (calcein) as a model for drug molecules into the mesopores of NCS and capped the nanospheres with a lipid bilayer containing DOPC and DOTAP (Figure 4.7). Afterwards, the calcein-loaded SLB@NCS were transferred into a tube sealed with a dialysis membrane (Figure 4.5 a) and mounted on top of a fluorescence cuvette filled with water. The membrane only allows the dye molecules to diffuse into the cuvette, whereas the NCS stay entrapped in the tube. As long as the cap system blocks the release of the dye, no fluorescence signal can be detected (Figure 4.5 b).[28,39]

In this experiment, even after 4 h, no significant release was observed. Only after rupture of the SLB through the addition of the surfactant Triton X-100, dye molecules were able to diffuse out of the bimodal porous carbon particles across the membrane into the cuvette. The entire amount of calcein was released within

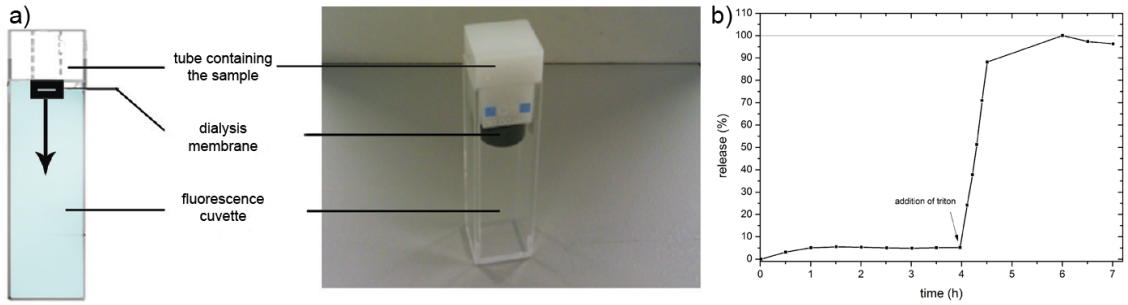

Figure 4.5: (a) Schematic presentation and photo of the release setup. (b) Release profile of calcein in SLB@NCS.

3 h (also see appendix, Figure 4.8). The amount of 121 μg calcein per mg NCS illustrates the very high loading capacity of these highly porous carbon spheres (for calculation, see appendix).

4.4 Conclusions

We present a strategy for the synthesis of 60 nm large and colloidal nanosized carbon spheres (NCS). Their bimodal porosity features a high BET surface area as well as a high pore volume, which makes them attractive candidates for drug delivery agents with high loading capacity. The synthesis is based on the replication of small macroporous silica hard templates, by concerted co-assembly of a mixture of resol, TEOS and Pluronic F127. After successive thermopolymerization, carbonization and silica removal, the bimodal mesoporous carbon spheres can be separated into colloidal NCS by oxidative treatment. The mesoporous nanoparticles were loaded from solution with fluorescent calcein as model drug and efficiently sealed with a stable supported lipid bilayer (SLB) cap system. Molecular release experiments demonstrate the effective closure and release of this system, providing a tight seal until the addition of Triton X-100, which destabilizes the lipid bilayer and initiates a complete and controlled release of the fluorescent dye from the highly porous carbon. Therefore, our results show the ability of SLB@NCS as effective cap system around colloidal mesoporous carbon nanoparticles with enhanced loading capacities for controlled release applications.

4.5 Appendix

SAXS

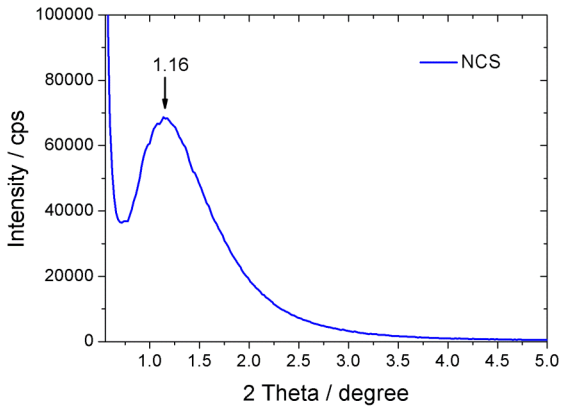

Figure 4.6: Small-angle X-ray scattering of dried NCS particles.

Chemical structures of the used phospholipid (DOPC, Avanti Polar Lipids) and lipid (DOTAP, Avanti Polar Lipids)

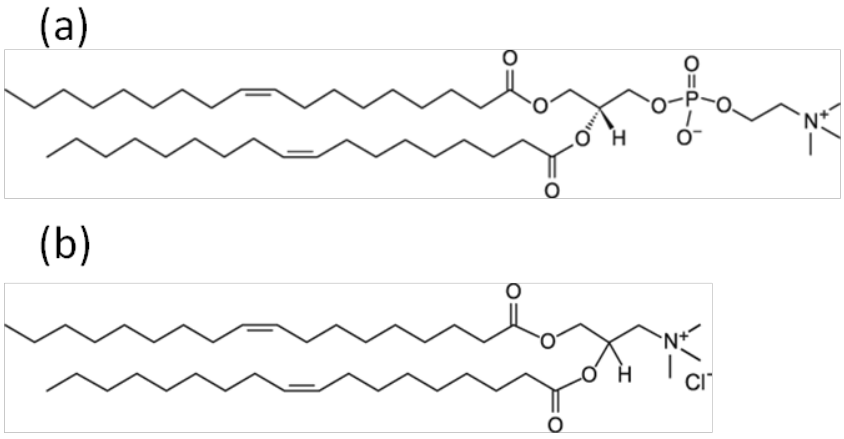

Figure 4.7: Chemical structures of 1,2-dioleoyl-sn-glycero-3-phosphocholine (a, DOPC) and 1,2-dioleoyl-3-trimethylammonium-propane (b, DOTAP).

UV-Vis

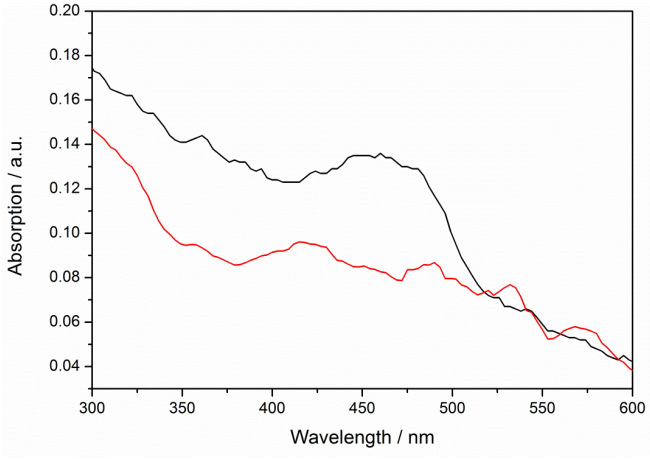

Figure 4.8: UV-Vis spectrum of SLB@NCS dispersion before (black) and after (red) the release experiment.

The black line represents SLB@NCS loaded with calcein. The peak shows the absorption of the loaded calcein. After the release (red line), no peak is visible, indicating complete release of the fluorescent dye out of the porous carbon particles. The absolute amount of calcein released from the sample SLB@NCS was quantified by fluorescence spectroscopy. A calcein calibration curve was recorded in the fluorescence spectrometer (Figure 4.9).

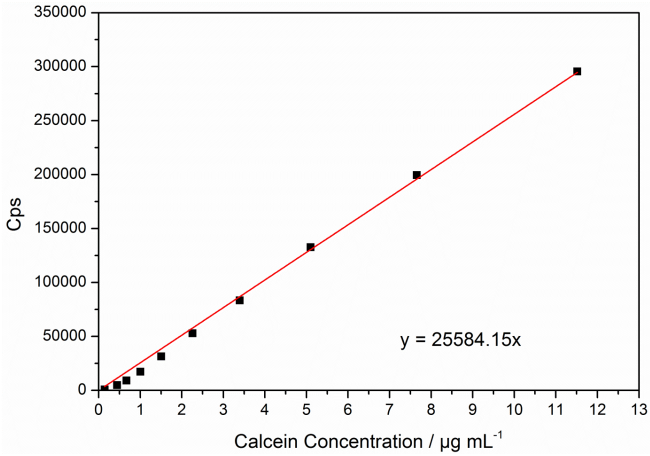

Figure 4.9: Calcein calibration curve.

Calculation of calcein in SLB@NCS

After reaching the plateau at the end of the release experiment, 257826 counts per second were detected. This intensity leads to a calcein concentration of 10.08 μg mL^{-1} by using the linear regression of the calibration curve. The cuvette has a volume of 3 mL which corresponds to an original amount of 30.23 μg calcein.
For the release experiment, only 200 μL of the original 800 μL sample dispersion were used. Thus the original amount of calcein in 1 mg NCS is calculated to 120.93 μg.
For loading the particles, 500 μL calcein stock solution (1 mM) was used corresponding to a total amount of 311 μg calcein.
In total, 120.93/311 (38.9%) of the initial calcein amount of the stock solution was adsorbed by the NCS particles.

Bibliography

[1] Yang, P., Gai, S., and Lin, J. *Chem. Soc. Rev.* **41**, 3679–3698 (2012).

[2] Yang, F., Jin, C., Jiang, Y., Li, J., Di, Y., Ni, Q., and Fu, D. *Cancer Treatment Reviews* **37**, 633–642 (2011).

[3] Tran, M. A., Watts, R. J., and Robertson, G. P. *Pigment Cell and Melanoma Research* **22**(4), 388–399 (2009).

[4] Wagner, E. *Accounts of Chemical Research* **45**(7), 1005–1013 (2012).

[5] Meyer, M., Dohmen, C., Philipp, A., Kiener, D., Maiwald, G., Scheu, C., Ogris, M., and Wagner, E. *Molecular Pharmaceutics* **6**(3), 752–762 (2009).

[6] Matsumoto, S., Christie, R. J., Nishiyama, N., Miyata, K., Ishii, A., Oba, M., Koyama, H., Yamasaki, Y., and Kataoka, K. *Biomacromolecules* **10**(1), 119–127 (2009).

[7] Miyata, K., Oba, M., Nakanishi, M., Fukushima, S., Yamasaki, Y., Koyama, H., Nishiyama, N., and Kataoka, K. *Journal of the American Chemical Society* **130**(48), 16287–16294 (2008).

[8] Hagiwara, A., Takahashi, T., Sawai, K., Sakakura, C., Yamaguchi, M., Osaki, K., Tsujimoto, H., Ohyama, T., Tomoda, H., Yamamoto, A., and Muranish, S. *Anti-Cancer Drugs* **5**, 194 (1994).

[9] Hagiwara, A., Takahashi, T., Sawai, K., Sakakura, C., Hoshima, M., Ohyama, T., Ohgaki, M., Imanishi, T., Yamamoto, A., and Muranishi, S. *Cancer* **78**(10), 2199–2209 (1996).

[10] Liu, Z., Sun, X., Nakayama-Ratchford, N., and Dai, H. *ACS Nano* **4**(12), 7726–7726 (2010).

[11] Ren, J., Shen, S., Wang, D., Xi, Z., Guo, L., Pang, Z., Qian, Y., Sun, X., and Jiang, X. *Biomaterials* **33**(11), 3324 – 3333 (2012).

[12] Liu, Z., Chen, K., Davis, C., Sherlock, S., Cao, Q., Chen, X., and Dai, H. *Cancer Research* **68**(16), 6652–6660 (2008).

[13] Liu, Z., Robinson, J. T., Tabakman, S. M., Yang, K., and Dai, H. *Materials Today* **14**(7-8), 316 – 323 (2011).

[14] Zhu, S., Chen, C., Chen, Z., Liu, X., Li, Y., Shi, Y., and Zhang, D. *Materials Chemistry and Physics* **126**(1-2), 357 – 363 (2011).

[15] Carrero-Sanchez, J. C., Elias, A. L., Mancilla, R., Arrellin, G., Terrones, H., Laclette, J. P., and Terrones, M. *Nano Letters* **6**(8), 1609–1616 (2006).

[16] Fang, Y., Gu, D., Zou, Y., Wu, Z., Li, F., Che, R., Deng, Y., Tu, B., and Zhao, D. *Angewandte Chemie International Edition* **49**(43), 7987–7991 (2010).

[17] Boncel, S., Herman, A. P., and Walczak, K. Z. *J. Mater. Chem.* **22**, 31–37 (2012).

[18] Magrez, A., Kasas, S., Salicio, V., Pasquier, N., Seo, J. W., Celio, M., Catsicas, S., Schwaller, B., and Forro, L. *Nano Letters* **6**(6), 1121–1125 (2006).

[19] Dumortier, H., Lacotte, S., Pastorin, G., Marega, R., Wu, W., Bonifazi, D., Briand, J.-P., Prato, M., Muller, S., and Bianco, A. *Nano Letters* **6**(7), 1522–1528 (2006).

[20] Ryoo, R., Joo, S. H., Kruk, M., and Jaroniec, M. *Advanced Materials* **13**(9), 677–681 (2001).

[21] Lee, J., Kim, J., and Hyeon, T. *Advanced Materials* **18**(16), 2073–2094 (2006).

[22] Kim, T.-W., Chung, P.-W., Slowing, I. I., Tsunoda, M., Yeung, E. S., and Lin, V. S.-Y. *Nano Letters* **8**(11), 3724–3727 (2008).

[23] Gu, J., Su, S., Li, Y., He, Q., and Shi, J. *Chem. Commun.* **47**, 2101–2103 (2011).

[24] Zhu, J., Liao, L., Bian, X., Kong, J., Yang, P., and Liu, B. *Small* **8**(17), 2715–2720 (2012).

[25] Liu, R., Shi, Y., Wan, Y., Meng, Y., Zhang, F., Gu, D., Chen, Z., Tu, B., and Zhao, D. *Journal of the American Chemical Society* **128**(35), 11652–11662 (2006).

[26] Schuster, J., He, G., Mandlmeier, B., Yim, T., Lee, K. T., Bein, T., and Nazar, L. F. *Angewandte Chemie International Edition* **51**(15), 3591–3595 (2012).

[27] Ashley, C. E., Carnes, E. C., Phillips, G. K., Padilla, D., Durfee, P. N., Brown, P. A., Hanna, T. N., Liu, J., Phillips, B., Carter, M. B., Carrol, N. J., Jiang, X., Dunphy, D. R., Willman, C. L., Petsev, D. N., Evans, D. G., Parikh, A. N., Chackerian, B., Wharton, W., Peabody, D. S., and Brinker, C. J. *Nature Materials* **10**, 389–397 (2011).

[28] Cauda, V., Engelke, H., Sauer, A., Arcizet, D., , C. B., Rädler, J., and Bein, T. *Nano Letters* **10**(7), 2484–2492 (2010).

[29] Liu, J., Jiang, X., Ashley, C., and Brinker, C. J. *Journal of the American Chemical Society* **131**(22), 7567–7569 (2009).

[30] Liu, J., Stace-Naughton, A., Jiang, X., and Brinker, C. J. *Journal of the American Chemical Society* **131**(4), 1354–1355 (2009).

[31] Nordlund, G., Sing Ng, J. B., Bergström, L., and Brzezinski, P. *ACS Nano* **3**(9), 2639–2646 (2009).

[32] Schlossbauer, A., Sauer, A. M., Cauda, V., Schmidt, A., Engelke, H., Rothbauer, U., Zolghadr, K., Leonhardt, H., Bräuchle, C., and Bein, T. *Advanced Healthcare Materials* **1**(3), 316–320 (2012).

[33] Torchilin, V. P. *Nature Reviews Drug Discovery* **4**, 145–160 (2005).

[34] Bayerl, T. M. and Bloom, M. *Biophysical journal* **58**, 357–362 (1990).

[35] Duncanson, W. J., Figa, M. A., Hallock, K., Zalipsky, S., Hamilton, J. A., and Wong, J. Y. *Biomaterials* **28**(33), 4991 – 4999 (2007).

[36] Mandlmeier, B., Szeifert, J. M., Fattakhova-Rohlfing, D., Amenitsch, H., and Bein, T. *Journal of the American Chemical Society* **133**(43), 17274–17282 (2011).

[37] Meng, Y., Gu, D., Zhang, F., Shi, Y., Cheng, L., Feng, D., Wu, Z., Chen, Z., Wan, Y., Stein, A., and Zhao, D. *Chemistry of Materials* **18**(18), 4447–4464 (2006).

[38] Vinu, A., Hossian, K. Z., Srinivasu, P., Miyahara, M., Anandan, S., Gokulakrishnan, N., Mori, T., Ariga, K., and Balasubramanian, V. V. *J. Mater. Chem.* **17**, 1819–1825 (2007).

[39] Schlossbauer, A., Kecht, J., and Bein, T. *Angewandte Chemie International Edition* **48**(17), 3092–3095 (2009).

[40] Holland, B. T., Blanford, C. F., and Stein, A. *Science* **281**(5376), 538–540 (1998).

[41] Holland, B. T., Blanford, C. F., Do, T., and Stein, A. *Chemistry of Materials* **11**(3), 795–805 (1999).

Chapter 5

Multifunctional Polymer-Capped Mesoporous Silica Nanoparticles for pH-responsive Targeted Drug Delivery

The following work is based on a joint project with Veronika Weiss, Annika Herrmann, Alexandra Schmidt, Daniel Edinger, Ernst Wagner, Christoph Bräuchle and Thomas Bein

5.1 Introduction

Polymers can be attractive for biological applications due to their biocompatibility, tuneable properties and derivation from sustainable sources.[1–3] Therefore, polymers are widely used as responsive coatings of surfaces for selective ion-permeability,[4] surface structuration[5] and drug delivery with polyplexes,[1,6,7] hybrid dendrimers,[8–10] and other drug-polymer conjugates.[11,12] Possible issues of pure polymer based drug delivery vehicles may arise from low loading capacities, the relatively poor stability, leading to premature release of the drug molecules and an inhomogeneous distribution thereof in the polymer matrix.[13] On the other hand, recently much effort has

been extended towards the development of inorganic nanoparticles, such as mesoporous silica nanoparticles (MSNs) for the delivery of bioactive compounds to cells and tumors.[14–18] MSNs have a high loading capacity and can be functionalized internally and on the external surface.[19] To prevent premature release out of these mesoporous systems, different strategies like covalent attachment of the cargo inside the mesopores[20,21] or complete capping of the whole particle[22–24] have been persued. The release mechanisms include changes in reduction potential,[21] pH,[15,23] temperature,[20] and irradiation with light.[12,17,21,25] A combination of the high loading capacity and stability of mesoporous nanoparticles with the biocompatibility and tuneable properties of polymers offers the possibility to create a stimuli-responsive and reversible delivery system. For instance, You *et al.* showed the release behaviour of poly(*N*-isopropylacrylamide) coated mesoporous silica at different temperatures.[26] Drug delivery vehicles based on nanoparticles in a size range of 100 nm are likely to be taken up by cells via endocytosis.[27] During this process, the endosome is being acidified by the action of proton pumps.[28,29] Therefore, pH-responsive polymer coatings around mesoporous silica nanoparticles offer the possibility to use the changes in pH during endocytosis as trigger for controlled release. For instance, attachment of poly(acrylic acid)[30] or poly(2-(diethylamino)ethyl methacrylate)[31] showed the ability to act as functional polymer coatings around mesoporous silica nanoparticles. Liu *et al.* demonstrated the use of poly(4-vinylpyridine) as pH-responsive capping system for mesoporous silica through multipoint anchoring in a "grafting to" method.[23] Poly(2-vinylpyridine) (PVP) has been widely used for the pH-sensitive functionalization of surfaces, due to the pronounced transition between hydrophilicity and hydrophobicity upon protonation and deprotonation.[5] Atkin *et al.* presented a combination of non-porous silica particles and polyvinylpyridine that could be useful for specific adsorption applications.[32]

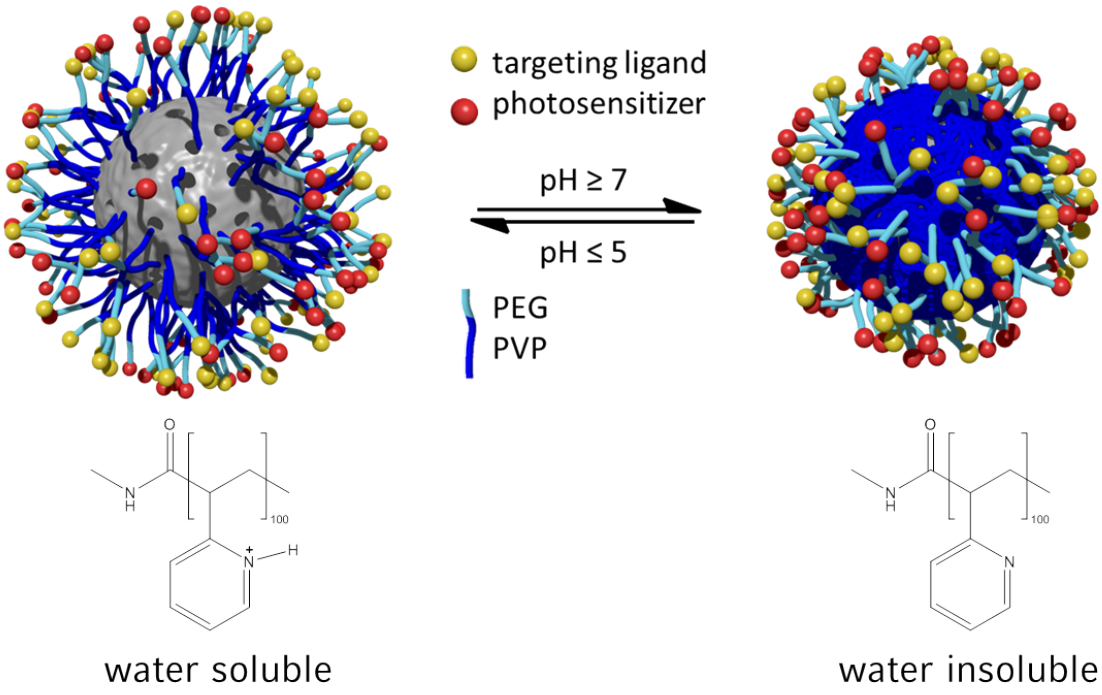

Figure 5.1: Concept of the pH-responsive delivery system. The pores can be reversibly opened and closed through changes in the water solubility of the polymer.

Here, we describe a multifunctional drug delivery vehicle that combines the high loading capacities of a mesoporous silica core and environmental sensitivity of a pH-responsive polymer. As shown in Figure 5.1, at low pH, the protonated polymer is in a hydrophilic state and therefore, cargo molecules are able to diffuse into and out of the mesoporous silica nanoparticle. At pH values of 5.5 or higher, deprotonation of the polymer takes place, producing a hydrophobic state followed by a collapse of the polymer onto the silica surface, preventing premature release of the cargo. Due to the pH-responsive switching behavior of the polymer, a site specific release mechanism is introduced to the delivery vehicle. After endocytic uptake of the particles by a cell, the endosomes are acidified by proton pumps which are present in the endosomal membrane.[28] The change in pH can automatically lead to a switch of the particle into its open state, and therefore trigger the release into the endosomal compartment. A major advantage of this delivery vehicle is offered by the reversibility of the cap system. Once the particles have been excreted by the cell before having released all of their cargo, the cap system is able to return into the closed state due to the environment (pH $>$ 7) outside of the cell.[28] To maintain colloidal dispersibility, even

in the hydrophobic closed state, poly(ethylene glycol) was attached to the end of the PVP cap system. The use of α-,ω-bis-functionalized polymers offers the possibility for anchoring any functionality of interest (photosensitizers, targeting ligands) step by step (Figure 5.1).

5.2 Experimental Section

Chemicals

All reagents were purchased from commercial suppliers: tetraethyl orthosilicate (TEOS, Fluka, >98%), cetyltrimethylammonium bromide (CTAB, Aldrich, 95%), (3-aminopropyl)triethoxysilane (APTES, Fluka, 95%), (3-mercaptopropyl)triethoxysilane (ABCR), *N*-(3-dimethylaminopropyl)-*N*-ethylcarbodiimide hydrochloride (EDC, Fluka, 97%), α-amino-ω-carboxy terminated poly(2-vinylpyridine) (NH_2-PVP-COOH, Polymer source, M_n = 10000, PDI = 1.08), α,ω-polyethyleneglycolbisamine (NH_2-PEG-NH_2, Aldrich, M_n = 2000), Boc anhydride (Aldrich, 95%), folic acid (Sigma, 99%), aluminum (lll) Phthalocyanine chloride tetrasulfonic acid ($AlPcS_{2a}$, Frontier Scientific), *N*-hydroxysulfosuccinimide sodium salt (Sulfo-NHS, Aldrich, 98%). Doubly distilled water from a Millipore system (Milli-Q academie A-10) was used for all syntheses and purification steps. All solvents and buffer contents were purchased from Sigma-Aldrich. Unless otherwise noted, all reagents were used without further purification.

Materials synthesis:

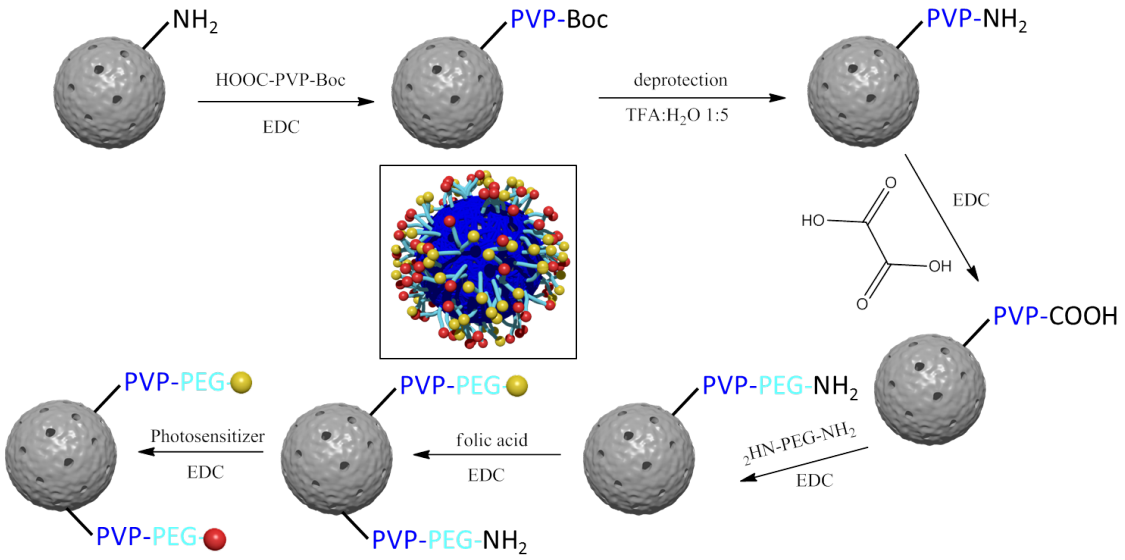

Figure 5.2: Representation of the synthesis strategy.

Preparation of shell-functionalized colloidal mesoporous silica nanoparticles (MSN-NH_2)

MSN nanoparticles were prepared by a delayed co-condensation approach as described earlier by Cauda *et al.*[19] In detail, a two phase mixture of TEA (14.3 g) and TEOS (1.9 g, 9.12 mmol) was heated at 90 °C for 20 minutes without stirring. After removal of the oil bath, a preheated (60 °C) solution of CTAC (2.14 mL, 1.62 mmol, 25 wt% in H_2O) and water (21.7 g) was added and stirred afterwards at 500 rpm for 30 min at room temperature. Subsequently, a mixture of 3-aminopropyltriethoxysilane (22.5 μL, 96 μmol) and TEOS (20.5 μL, 92 μmol) was added. The resulting solution was stirred overnight at room temperature at 500 rpm. The particles were separated by centrifugation (19000 rpm, 43146 rcf) and redispersion in ethanol. Extraction of the organic template was achieved by heating the ethanol-suspended sample (10 mg/mL) under reflux at 90 °C for 1 h in a mixture of 2 g ammonium nitrate and 100 mL ethanol. Afterwards, the sample was centrifuged for 20 minutes at 19000 rpm, redispersed in ethanol and heated under

reflux at 90 °C in a solution of 8 mL concentrated HCl and 32 mL ethanol for 45 minutes. After centrifugation, the particles were redispersed in ethanol, resulting in a colloidal suspension.

Protection of NH_2-PVP-COOH (Boc-PVP-COOH)

To a solution of 500 mg (5 μmol) NH_2-PVP-COOH in 10 mL dry dichloromethane, 15 μL (0.11 mmol) triethylamine and 15 mg (6.9 μmol) Boc anhydride were added. The solution was stirred overnight at room temperature and extracted several times with brine. The organic phase was dried over $MgSO_4$ and evaporated to dryness to afford the Boc protected polymer. The polymer was used without further purification.

General procedure for the attachment of poly(2-vinyl pyridine) to MSN-NH_2 (MSN-PVP-Boc)

To a dispersion of 50 mg MSN-NH_2 in 10 mL tetrahydrofuran (THF), 60 mg (5.6 μmol) polymer dissolved in 1.5 mL THF was added. The amidation was activated by the addition of 10 μL (57.2 μmol) EDC and 1.3 mg (6 μmol) sulfo-NHS. The mixture was stirred at room temperature for 12 h. Afterwards the particles were separated by centrifugation (19000 rpm, 43146 rcf, 20 min) and washed three times by repeated centrifugation and redispersion in 30 mL THF.

Deprotection of MSN-PVP-Boc (MSN-PVP-NH_2)

Deprotection of the polymer was achieved through stirring 10 mg polymer functionalized particles in a mixture of 2 mL trifluoroacetic acid and 8 mL water for 24 h. After deprotection, the particles were extensively washed by centrifugation (19000 rpm, 43146 rcf, 20 min) and redispersion in a mixture of EtOH:water 1:1.

Conversion of MSN-PVP-NH_2 to MSN-PVP-COOH

10 mg MSN-PVP-NH_2 in 2 mL EtOH (taken from a stock solution) were reacted with a large excess of oxalic acid (5 mg, 55 μmol) and EDC (9 μL, 51 μmol) for 1

h. Afterwards the particles were extensively washed by centrifugation (19000 rpm, 43146 rcf, 20 min) and redispersion in a mixture of of EtOH:water 1:1.

PEGylation of MSN-PVP-COOH (MSN-PVP-PEG-NH_2)

To a dispersion 1 mg MSN-PVP-COOH (taken from a stock solution) in 500 μL EtOH, 2 mg (100 nmol) NH_2-PEG-NH_2 in 500 μL bidistilled water was added and the reaction was started through the addition of 0.5 μL (2.8 μmol) EDC. After stirring for 1 h at room temperature, the sample was washed 3 times by centrifugation with a mixture of EtOH:water 1:1.

Attachment of folic acid to MSN-PVP-PEG-NH_2 (MSN-PVP-PEG-NH_2-FA)

The amino functionalities of 1 mg MSN-PVP-PEG-NH_2 in 1 mL EtOH:water 1:1 were partially reacted with 0.44 μg (1 nmol) folic acid. To start the reaction, 0.5 μL (2.8 μmol) EDC and a very small amount ($\approx$0.5 mg) of sulfo-NHS were added. After 1 h, the sample was washed 3 time by centrifugation with a mixture of EtOH:water 1:1.

Attachment of $AlPcS_{2a}$ to residual amino groups of MSN-PVP-PEG-NH_2-FA (MSN-PVP-PEG-FA-$AlPcS_{2a}$)

To the sample MSN-PVP-PEG-NH_2-FA in 1 mL DMSO:water 1:1 was added 20 μL of $AlPcS_{2a}$ (1 mg/mL in DMSO). The resulting mixture was stirred at room temperature in the dark for 24 hours. Subsequently, the sample was washed extensively with DMSO:water 1:1 (centrifugation 19000 rpm) until there was no photosensitizer in the supernatant.

Release experiments:

Drug/dye loading

1 mg MSN-PVP-PEG-NH_2 were dispersed in 500 μL of a 1 mM drug/dye solution in water. To open the pores and enable the uptake, 50 μL of citrate buffer (pH

2) were added. The particles were stirred overnight, centrifuged (19000 rpm), and redispersed in 1 mL SSC buffer (pH 7) to trigger closure of the polymer shell. The particles were washed extensively with SSC buffer until no fluorescence was detected in the supernatant.

In vitro fluorescein release

1 mg fluorescein loaded MSN-PVP-NH_2 or MSN-PVP-PEG-NH_2 were redispersed in 200 μL SSC buffer and transferred to the cap of the fluorescence cuvette. This cap is sealed with a dialysis membrane (molecular weight cutoff of 16000 g/mol) and placed on top of the fluorescence cuvette, which is also filled with 3 mL SSC buffer. The "release" of fluorescein out of the closed particles was monitored for 2 h (λ_{ex} = 490 nm, λ_{em} = 512 nm). Subsequently, the cap was removed and the particles were centrifuged and redispersed in 200 μL citrate-phosphate buffer (pH 5), before being put into the cap of the release setup. The fluorescence cuvette was also filled with citrate-phosphate buffer (pH 5). After reassembling of the release setup, the release of fluorescein was measured for 10 h continuously. For comparison of the obtained curves, calibration curves of fluorescein in SSC buffer (pH 7) and in citrate-phosphate buffer (pH 5) were recorded.

Cell culture and *in vitro* experiments:

Cell culture

KB cells were grown in folic acid deficient Roswell Park Memorial Institute 1640 medium (RPMI 1640, Invitrogen) supplemented with 10% fetal bovine serum (FBS). HeLa cells were grown in Dulbecco's modified Eagle's medium (DMEM):F12 (1:1) (Invitrogen) with Glutamax I medium supplemented with 10% FBS. Tubulin-GFP expressing HuH7 cells were grown in Dulbecco's modified Eagle's medium:F12 (1:1) supplemented with 10% FBS. All cells were cultured at 37 °C in a 5% CO_2 humidified atmosphere. KB cells were seeded on ibidiTreat μ-Slides (IBIDI). HeLa and tubulin GFP expressing HuH7 cells were seeded on collagen A-coated LabTek chambered cover glass (Nunc). For live cell imaging the cells were seeded 48 or 24 h before

measuring, at a cell density of 1x10^4 or 2x10^4 cells / cm^2 respectively.

Spinning disc confocal microscopy

Live-cell imaging was performed on a confocal setup based on the Zeiss Cell Observer SD, utilizing a Yokogawa spinning disc unit CSU-X1. The system was equipped with a 1.40 NA 100x or 63x Plan apochromat oil immersion objective from Zeiss. The exposure time was 0.1 s for all experiments und the frame rate varied between 3 frames / s and 1 frame / 30 s, depending on the experiment. WGA 488 and GFP were imaged with approximately 1.5 W / mm^2 and 7.5 W / mm^2 of 488 nm excitation light. Atto 633 was imaged with approximately 0.06 W / mm^2 of 639 nm excitation light and DAPI with 1 W / mm^2. The photosensitizer $AlPcS_{2a}$ was excited with approximately 0.12 W / mm^2 at 639 nm for imaging and with 1.2 W / mm^2 for photoactivation. In the excitation path a quad-edge dichroic beamsplitter (FF410/504/582/669-Di01-25xx36, Semrock) was used. For the two-color detection of calcein and $AlPcS_{2a}$, WGA 488 and Atto 633 or GFP and Atto 633, a dichroic mirror (660 nm, Semrock) and band-pass filters 525 / 50 and 690 / 60 (both semrock) were used in the detection path. Separate images for each fluorescence channel were acquired using two separate electron multiplier charge coupled devices (EMCCD) cameras (Photometrics Evolve^{TM}).

Uptake studies

The functionality of the folic acid targeting ligand was evaluated in a receptor competition experiment. For this purpose one part of the KB cells was preincubated with 3 mM folic acid (Sigma), to block the receptors, for 2 h at 37 °C under a 5% CO_2 humidified atmosphere. Then the KB cells were incubated with particles (MSN-PVP-PEG-FA, covalently labeled with Atto633; 25 μg/mL) for 2 h at 37 °C under a 5% CO_2 humidified atmosphere. After the incubation the cells were washed three times with PBS (Invitrogen) and 250 μL of 4% paraformaldehyde (PFA, Science Service) were added for 15 min. The PFA was removed and the cells were washed again three times with PBS. For staining the cell membrane, the cells were

incubated with a final concentration of 10 μg/mL wheat germ agglutinin Alexa Fluor 488 conjugate (WGA 488, Invitrogen) for one minute. The cells were washed once with PBS and imaged.

Cargo release experiments

To measure the photoactivated cargo release the cells were incubated with particles (MSN-PVP-PEG-AlPcS$_{2a}$-FA, 25 μg/mL) for 16-20 h at 37 °C under a 5% CO_2 humidified atmosphere. For imaging the medium was replaced by CO_2-independent medium (Invitrogen), during the measurements the cells ware kept on a heated microscope stage at 37 °C. For activation of the photosensitizer the cells were irradiated with 1.2 W / mm^2 of 639 nm light for 1 min. The release of cell-membrane permeable cargo due to pH-dependent opening of the PVP-coating inside the endosomes was also measured. For this purpose tubulin GFP expressing HuH7 cells in the case of colchicine-release were incubated with particles (MSN-PVP-PEG-loaded with colchicine, 100 μg/mL) for 18 h at 37 °C under a 5% CO_2 humidified atmosphere. In the case of DAPI-release HeLa cells were incubated with either particles (MSN-PVP-PEG loaded with DAPI, 25 μg/mL) or the quantitatively equal amount of supernatant of centrifuged particles (14000 rcf, 4 min.). Incubation times of 15 min, 15 h and 46 h under a 5% CO_2 humidified atmosphere were chosen to demonstrate the pH- and therefore time-dependent release of DAPI.

***In vivo* experiments**

For all in vivo experiments female Rj:NMRI-nu (nu/nu) (Janvier, Le Genest-St-Isle, France) mice were housed in isolated ventilated cages with a 12 h day/night cycle and food and water ad libitum. Animal experiments were performed according to guidelines of the German law of protection of animal life and were approved by the local animal experiments ethical committee.

MSN retention in tumors

Human cervix carcinoma cells (KB wild-type) were cultured as described above. Mice were injected with 5x10^6 cells subcutaneously into the nape and tumors were allowed to grow for 14 days. At day 14, mice were anesthetized with 3% isoflurane in oxygen and 100 μg (5 mg/kg) of Cy-7 labeled MSN-PVP-PEG-NH_2 with and without folic acid ligand solved in 50 μL (HBG) were injected intratumorally to test for differential retention in tumors. The near infrared fluorescence signals were recorded by a CCD camera immediately after injection and recording was repeated after 0.25, 0.5, 1, 4, 24 h and daily for one week using the IVIS Lumina system. Data interpretation was done with equalized color bar scales for each trial and pictures were analyzed using the Living Image software 3.2 (Caliper Life Sciences, Hopkinton, MA, USA).

MSN biodistribution

For analysis of MSN, mice were anesthetized with 3% isoflurane in oxygen. A 100 μg (5 mg/kg) dose of Cy-7 labeled MSN-PVP-PEG-NH_2-FA or unfunctionalized MSN solved in 200 μL (HBG) was injected intravenously into the tail vein of tumor-free mice. Near-infrared fluorescence imaging by a CCD camera using the IVIS Lumina system with Living Image software 3.2 (Caliper Life Sciences, Hopkinton, MA, USA) was started immediately after injection and repeated after 0.25, 0.5, 1, 4, 24, 48 and 72 h.

5.3 Results and Discussion

Particle characterization

According to TEM, the shell functionalized mesoporous silica nanoparticles show an average particle diameter of 90 nm with a wormlike pore structure (Figure 5.3 a). Stepwise functionalization with poly(2-vinylpyridine) and PEG was monitored with several methods and will be discussed in the following.

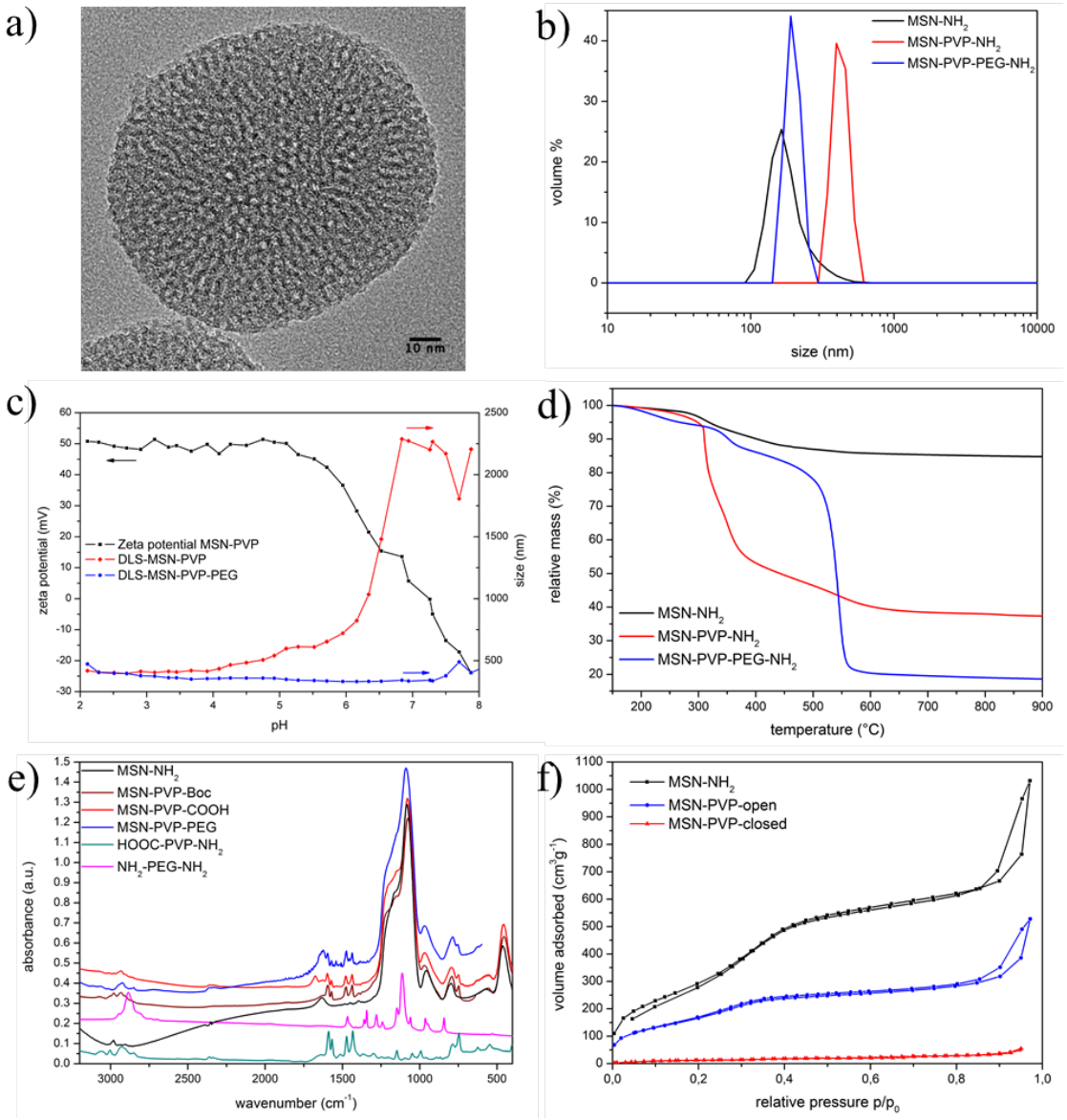

Figure 5.3: Characterization of functionalized MSN. (a) transmission electron microscopy, (b) dynamic light scattering, (c) titration experiments (d) thermogravimetric analysis, (e) infrared spectroscopy, (f) nitrogen sorption.

DLS measurements revealed the need of PEG as stabilizing agent. The hydrodynamic diameter of shell functionalized MSN in water could be determined to 160 nm (Figure 5.3 b). MSN nanoparticles functionalized with PVP show strong aggregation in aqueous media due to its hydrophobicity at pH 7 as can be seen by an apparent size increase to 550 nm (See appendix Figure 5.15). However, the attachment of PEG to the end group of PVP recovers the colloidal nature of the system (DLS reveals a size of around 200 nm again).Titration experiments are shown in Figure 5.3 c. The high zeta potential (+50 mV) of MSN-PVP represents the fully

protonated state of pyridine. Deprotonation of the polymer cap system occurs at a pH value of around 5.5 (close to the pK_a of PVP), leading to a significant drop in zeta potential. Together with the zeta potential, DLS measurements were performed simultaneously at the same pH values. For MSN-PVP the particles showed good colloidal dispersability as long as the polymer remained in its protonated state (Figure 5.3 c). Upon deprotonation, the polymer collapses on the particle surface, forming a hydrophobic shell around the particles which can be observed in the increase in size due to agglomeration. Further attachment of PEG led to the suppression of aggregation as no changes in size were observed over the whole pH-range for MSN-PVP-PEG (Figure 5.3 c).

The functionalization of the mesoporous silica nanoparticles was also monitored with TGA (Figure 5.3 d). While the shell functionalized nanoparticles (MSN-NH_2) show a relative mass loss of 14.6% (2.97 mmol per gram silica), the relative mass loss of 61.6% for MSN-PVP-NH_2 corresponds to 0.14 mmol PVP per gram silica. Only 4.7% of the amino-groups present at the surface have reacted with the polymer. Based on the mass loss of 80.4% in the sample MSN-PVP-PEG, the amount of 1.3 mmol PEG per gram silica could be calculated. This result shows that additional attachment of PEG to the shell of the MSN must have occurred besides the attachment to the end of the polymer cap system. IR spectroscopy serves to follow each step of the synthesis (Figure 5.3 e). The signals at 1590 cm^{-1} and 1570 cm^{-1} correspond to the C=C stretch vibrations of the aromatic pyridine ring and can be found in all spectra after attachment to MSN. Additionally, in these spectra the C=N stretch vibrations of the aromatic ring can be found at 1474 cm^{-1} and 1430 cm^{-1}. After deprotection of MSN-PVP and conversion of the amino group into a carboxy functionality with oxalic acid, a peak at 1677 cm^{-1} appears which can be attributed to the asymmetric C=O stretching vibration of MSN-PVP-COOH. This peak vanishes after the addition of poly(ethylene glycol) bisamine, which underlines the successful attachment of PEG.

In order to show the ability of poly(2-vinylpyridine) to act as a pH responsive cap system, nitrogen sorption measurements were performed (Figure 5.3 f, Table 5.1).

For MSN-PVP$_{open}$, the particles where dried from a 0.01 M HCl dispersion at 60 °C, to keep the PVP functionalized MSN in an open state. The closed state could be realized through drying from a dispersion in Millipore water. It can be seen that in the open state, the pores are accessible, whereas in the closed state, the polymer completely blocks the pores. The BET surface area of 51 m^2/g in the closed state is in very good agreement with an estimated BET surface area of 45 m^2/g of spheres with similar density and diameter. The BET surface area of 51 m^2/g for MSN-PVP$_{closed}$ corresponds to a reduction in surface area of 95% compared with MSNs without polymer cap system (MSN-NH_2), indicating that the surface of the pore walls after blocking is not accessible, even for nitrogen.

Table 5.1: Summary of nitrogen sorption measurements.

Sample	BET surface area [m^2/g]	NLDFT pore size [nm]	NLDFT pore volume [cm^3/g]
MSN-NH_2	1097	3.78	0.79
MSN-PVP$_{open}$	617	3.42	0.36
MSN-PVP$_{closed}$	51	-	-

Release experiments

To verify the release properties of the particle-system several experiments were performed. First the pH dependency was tested *in vial*, in a cuvette system, at pH 7 and pH 5. Second the particles were tested in vitro, therefore they were incubated with cells to clarify if the acidification of the endosome is efficient enough to deliver the cargo. For that purpose the MSN were loaded with membrane-permeable and membrane-impermeable cargos and incubated for several hours with cells. As for membrane-impermeable cargos no endosomal escape could be observed, a photosensitive molecule was introduced to the system in order to trigger the endosomal escape externally.

In vial

The pH-responsive opening of the polymer cap system was demonstrated by quantification of the released calcein molecules with fluorescence spectroscopy (Figure 5.4 a). All intensity values are normalized to the highest obtained fluorescent counts of the respective sample. Therefore, the highest amount released is set to 100% relative release. The pH-dependent release curves show the striking capping effect of the poly(2-vinylpyridine) cap system. At pH 7, the polymer is in its hydrophobic state and thus successfully blocks the pores of the MSN until the release is triggered through decreasing the pH. In acidic media, the polymer changes into its water soluble hydrophilic state through protonation which allows the cargo the diffuse out of the pores. As can be seen in Figure 5.4 a, no significant changes in release kinetics are observed through further attachment of PEG compared with MSN-PVP. The total amount of cargo loaded into the MSNs could be calculated to 20.4 μg dye per mg MSN. Long-term release experiments showed that even after 16 h less than 4% of the initial loading had been released (Figure 5.4 b).

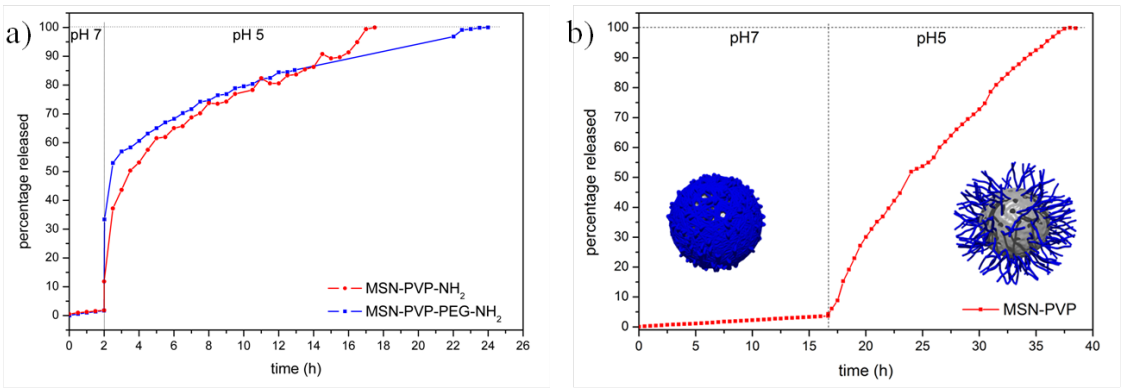

Figure 5.4: Release curves (normalized fluorescence intensity of fluorescein) of (a) MSN-PVP (red) and MSN-PVP-PEG (blue). (b) Long-term release experiments of MSN-PVP.

In vitro

The release of cargo inside the desired tissue is one of the greatest challenges in drug delivery. Many systems have been developed and characterized, like fusion, redox-

sensitive systems and photoactivation.[29] Some of these systems exhibit already a good temporal and spatial control of the cargo-release. But once they are activated, the release of the cargo is unstoppable, even if the particles leave the tissue of interest. One advantage of our newly developed system is the reversibility of the pore opening. If the pH of the environment turns neutral again, PVP will close the pores and the delivery system can safely circulate inside the blood system.

Photoactivated release

In the first experiments, MSN-PVP-PEG particles, loaded with calcein were incubated on HeLa cells for 20 h. The incubation time is long enough to allow the endosomal acidification.[33] But as can be seen in Figure 5.5, the fluorescence colocalization of the membrane-impermeable cargo calcein and the covalently to the particles bound dye Atto 633 remained. Calcein is a membrane impermeable cargo and therefore is not able to exit intact endosomal compartments without external trigger, but it should be released inside the endosomal compartment.

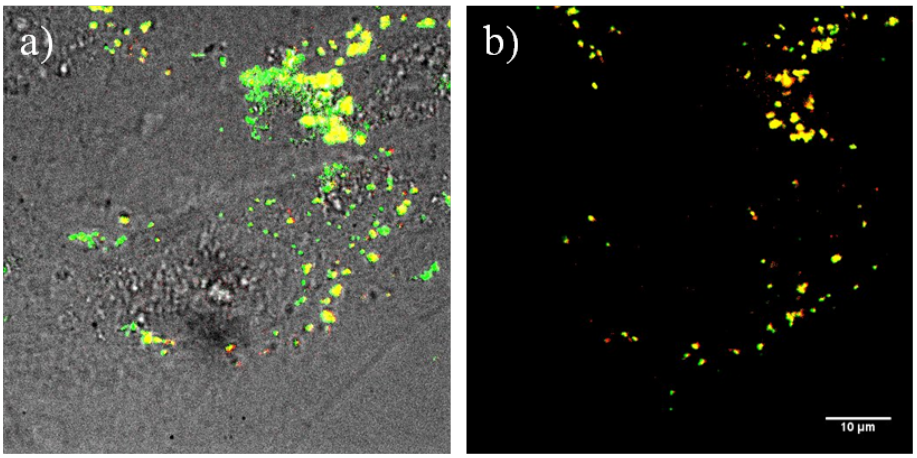

Figure 5.5: Fluorescence microscopy of MSN(Atto633)-PVP-PEG (25 μg/mL) nanoparticles loaded with calcein inside HeLa cells after 20 h incubation. (a) merge of brightfield image and fluorescence image. (b) fluorescence image of calcein (green) and Atto633 (red) are co-localized (yellow), no spreading of calcein can be observed, thus no endosomal escape. The scale bar represents 10 μm.

For membrane-impermeable cargos the system had to be further enhanced to induce endosomal escape. Thus the photosensitizer $AlPcS_{2a}$ (PS) was linked to the

PEG-chains, in addition to the pH-sensitive polymer. Endosomal escape is expected to occur after acidification of the endosomes and activation of the photosensitizer with red light. After activation with red light (639 nm, 1.2 W / mm^2) singlet oxygen is produced and can destroy the endosomal membrane. But as the lifetime of the singlet oxygen is very short (around 2 x 10^{-7} s)[34] the diffusion range is limited and therefore the cargo and also the cell membrane should stay intact, because of the spatial separation of cargo or cell membrane and PS. Also the red activation region of the photosensitizer is in a useful region for medical applications and is already used in photodynamic therapy.[35]

MSN-PVP-PEG-AlPcS$_{2a}$-FA were incubated on HeLa cells for 18 h. As can be seen in Figure 5.6 calcein and PS are co-localized (yellow spots, Figure 5.6 c). Directly after 1 min photoactivation with 1.2 W / mm^2 of 639 nm light calcein-spreading over the whole cell can be observed, and the calcein-fluorescence gets brighter over time due to de-quenching of the dye (Figure 5.6 e, i, m). In comparison to calcein the fluorescence of the photosensitizer stays localized in the same dot-like pattern as before the photo-activation, only the intensity is reduced because of photo-bleaching effects after the activation (Figure 5.6 f, j, n). The intensity profile along the white line, indicated in the merged pictures, depict the fluorescence increase of calcein more clearly (Figure 5.6 d, h, l, p). The cargo release can be also visualized with a constant PS-activation and simultaneous observation of calcein fluorescence (over 8 min; Figure 5.7). Within two minutes a significant part of the cargo seems to be released inside the cell.

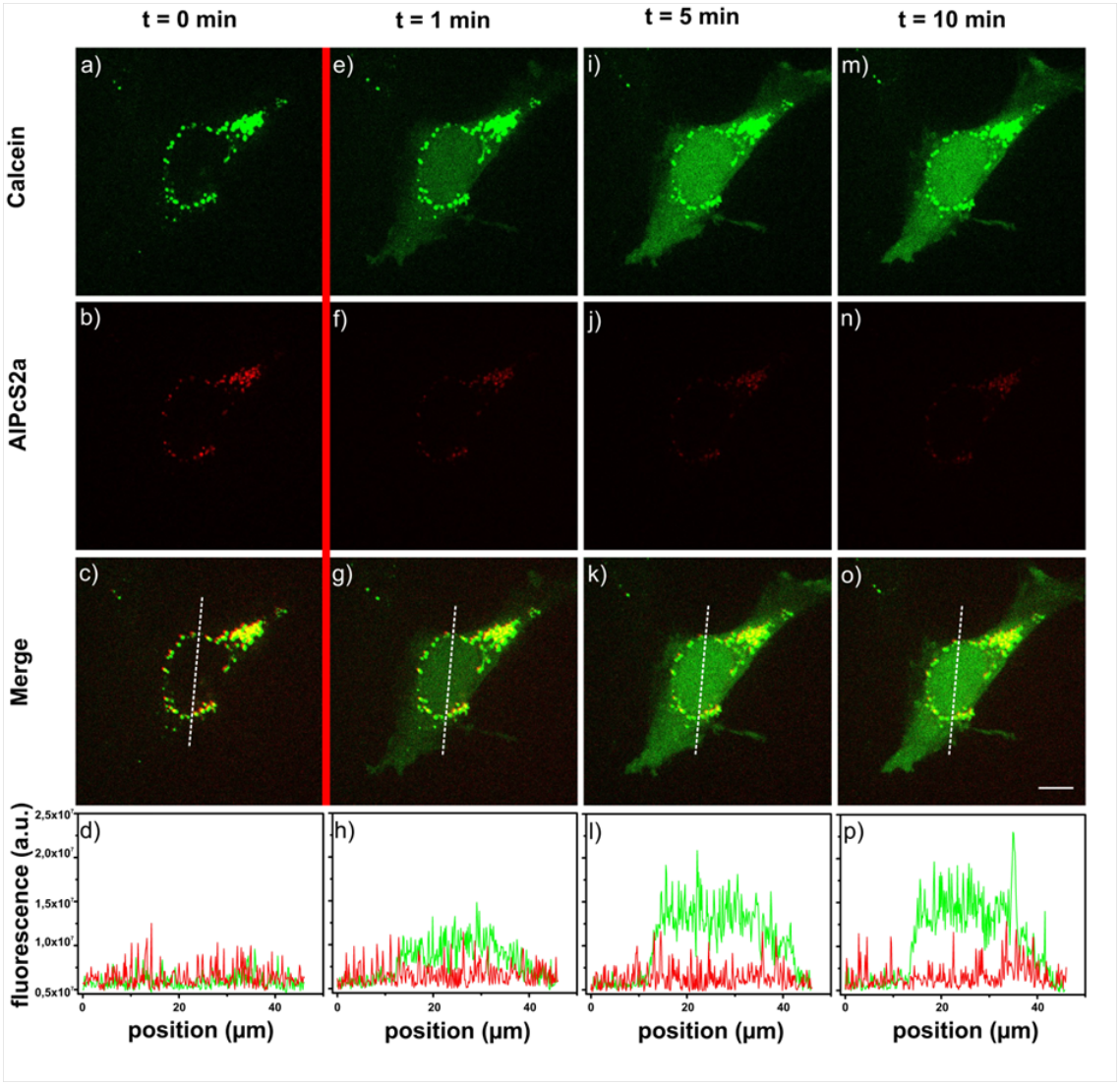

Figure 5.6: Fluorescence microscopy of MSN-PVP-PEG-AlPcS$_{2a}$-FA nanoparticles loaded with calcein after 18 h incubation on a HeLa cell. (a-c) Calcein (green) and AlPcS$_{2a}$ (red) are co-localized (yellow) prior to photoactivation. (d) Intensity profile along the white line in the merged image. The red line indicates photoactivation with 1.2 W / mm^2 of red light (639 nm). (e-h) after 1 min. photoactivation, (i-l) 5 min. after photoactivation, (m-p) 10 min after photoactivation. The scale bar represents 10 μm.

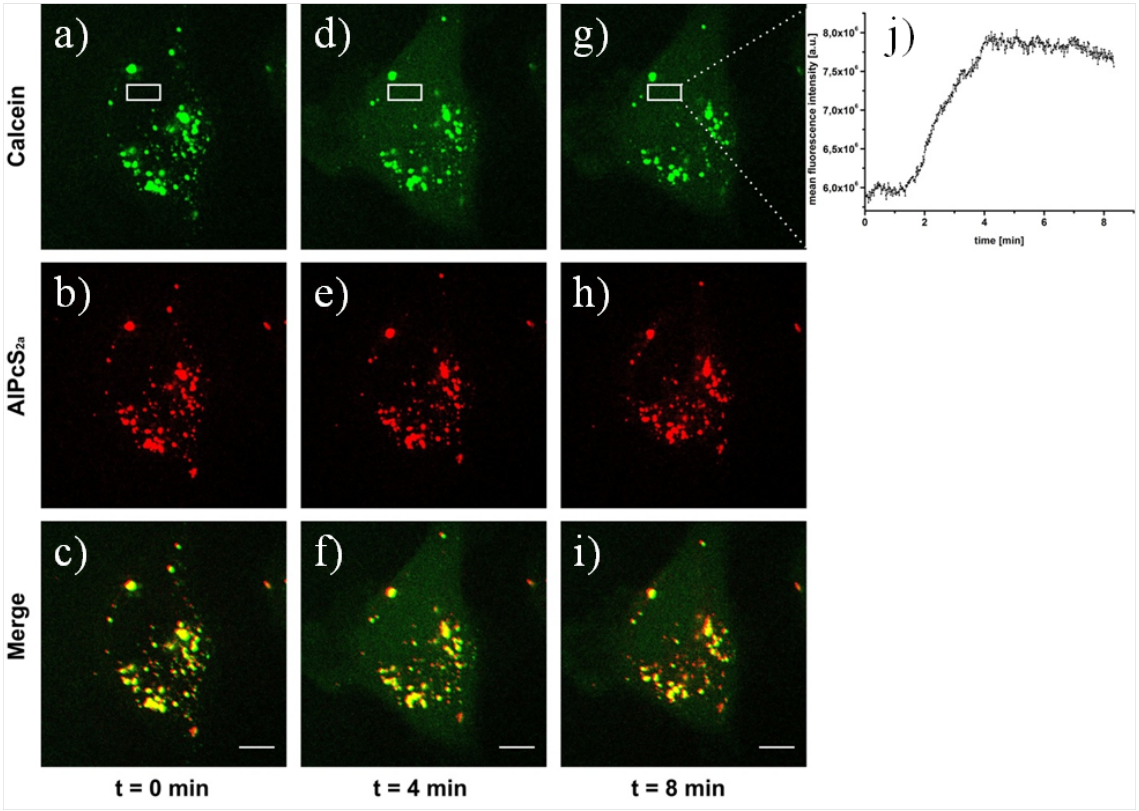

Figure 5.7: Fluorescence microscopy of MSN-PVP-PEG-AlPcS$_{2a}$-FA (25 μg/mL) nanoparticles loaded with calcein inside HeLa cells after 24 h incubation. (a-c) calcein (green) and AlPcS$_{2a}$ (red) are co-localized (yellow) prior to photoactivation. The cell was constantly monitored with a frame rate of 1 frame/s and 0.6 W / mm^2 of red light (639 nm). (d-i) example images after different time points, spreading of calcein can be clearly seen over time, whereas AlPcS$_{2a}$ stays at the same place. (j) intensity of calcein fluorescence inside the cytosol over time in the indicated rectangle, after approximately 2 min. increase can be monitored. The scale bar represents 10 μm.

These results were compared to incubation of cells with a solution of free calcein and PS. As can be seen in Figure 5.8 the amount of internalized calcein is neglible. We also observe that the PS is spreading over the whole cell. If the PS is not covalently bound to an MSN the molecules can diffuse inside the whole cell and can cause much more damage on the cell membrane and other organelles due to the proximity.

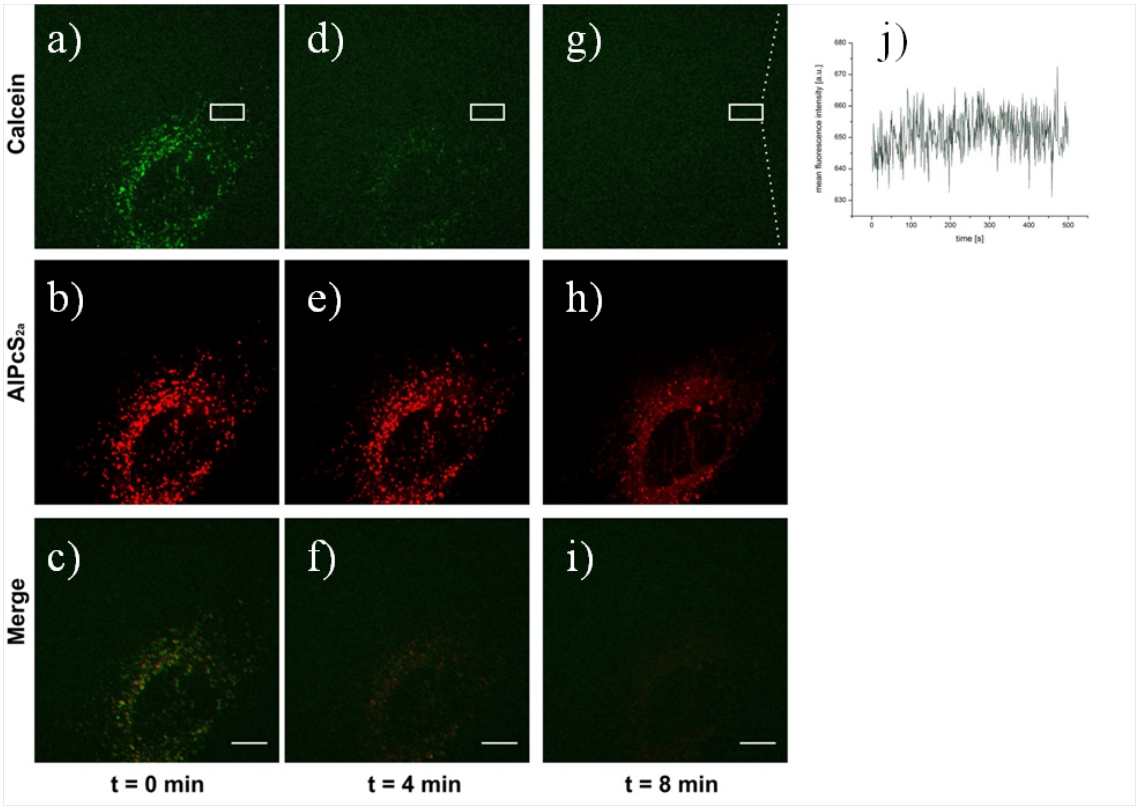

Figure 5.8: Fluorescence microscopy of free calcein and free $AlPcS_{2a}$ (each 2.5 μg / mL) inside HeLa cells after 24 h incubation. (a-c) Calcein (green) and $AlPcS_{2a}$ (red) are co-localized (yellow) prior to photoactivation. The cell was constantly monitored with a frame rate of 1 frame / s and 0.6 W / mm^2 of red light (639 nm). (d-i) example images after different time points, spreading of $AlPcS_{2a}$ can be clearly seen over time, whereas the calcein fluorescence is too weak to be detected after some time. (j) intensity of calcein fluorescence inside the cytosol over time in the indicated rectangle, no increase inside the cytosol can be detected. The scale bar represents 10 μm.

Release of membrane-permeable cargos

To safely deliver membrane-permeable cargos like DAPI[36] or colchicine[37] inside cells with our newly developed system the attachment of other endosomal escape mechanisms is not necessary. It is anticipated that the particles will get uptaken in endosomal compartments and in the following the endosomes get acidified. This drop in pH from around 7 to approximately 5 results in the solvation of poly(2-vinyl pyridine) and thus in release of the cargo out of the pores into the endosome and consequently into the cytosol if it diffuses through the endosomal membrane. On the other hand, if the particles get exocytosed the pH will increase and poly(2-vinyl pyridine) will turn insoluble again. In this case the cargo will stay inside the particles and they can circulate again and possibly find a new target cell. As model

systems to examine the delivery of membrane permeable cargos DAPI or colchicine were used. DAPI preferentially stains dsDNA and thereby produces a fluorescence enhancement of around 20-fold.[38] In Figure 5.9 the staining of the nucleus after several time intervals is shown. Shortly after incubation only a weak staining of the nucleus can be seen, after 15 h the nucleus is clearly visible and after 46 h even the RNA inside the region of the endoplasmic reticulum gets stained. Because of the increasing and very strong DAPI-fluorescence signal after several hours of incubation it could be excluded that the staining is due to free DAPI in the particle solution. Tests with incubation of particle supernatant show only a negligible staining of the nucleus (as can be seen in the appendix in Figure 5.20). In the case of free DAPI in the solution it also would be expected to be detectable shortly after addition, as the proposed incubation time for nucleus staining with free DAPI in solution is between 1-5 minutes.

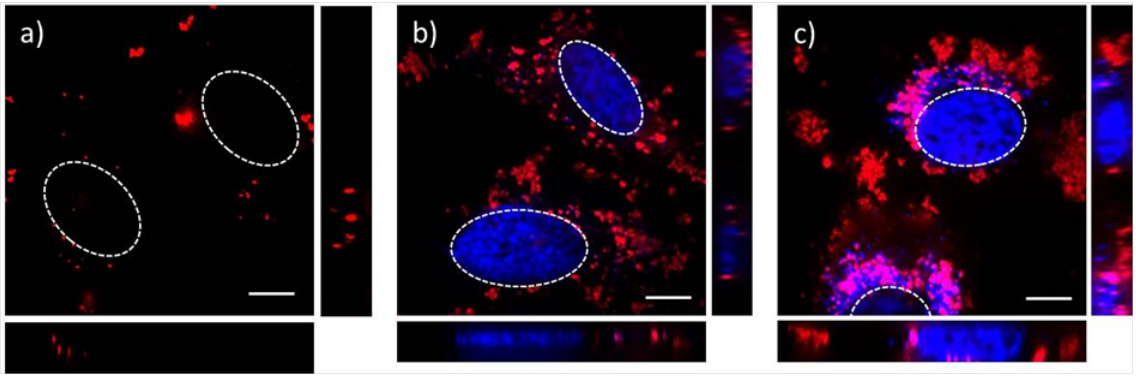

Figure 5.9: Fluorescence microscopy of HeLa cell incubated with MSN-PVP-PEG nanoparticles loaded with DAPI (blue) and labeled with Atto 633 (red) after (a) 15 min (b) 15 h and (c) 46 h incubation on the cells. The nuclear region is indicated with dashed white circles. The scale bar represents 10 μm.

The second cargo colchicine hinders the polymerization of microtubuli as it binds to free tubulin.[37] It is blocking the formation of the mitotic spindle but not the mitosis itself. For this study stable GFP-transfected liver carcinoma cells (HuH7) were used, such that GFP is attached to the tubulin network. In Figure 5.21 b) a picture of untreated HuH7 cells with GFP tagged on the tubulin network is depicted, one can clearly see the fibrous tubulin network. As shown in Figure 5.21 a) MSN-

PVP-PEG (red) particles loaded with colchicine were incubated for 18 h, and as can be clearly seen, the fibrous structure vanished completely, because the new formation of the network is hindered.

Targeting experiments

To achieve an effective drug delivery system, a targeting system is highly desirable. Generally one can distinguish between passive and active targeting. Modifications such as attaching PEG at the surface of the delivery system provide shielding against undesired interactions, and therefore favor the enhanced permeability and retention effect (passive targeting). Active targeting, on the other hand, takes advantage of the overexpression of certain ligands on diseased cells by attachment of the corresponding targeting ligand to the delivery vehicle.[39] Therefore the biocompatibility and effectiveness of the PEGylation procedure was tested further in an in vivo setting in mice. Active targeting was shown in vitro and in vivo using the example of folic acid (FA) receptor targeting on KB-cells.

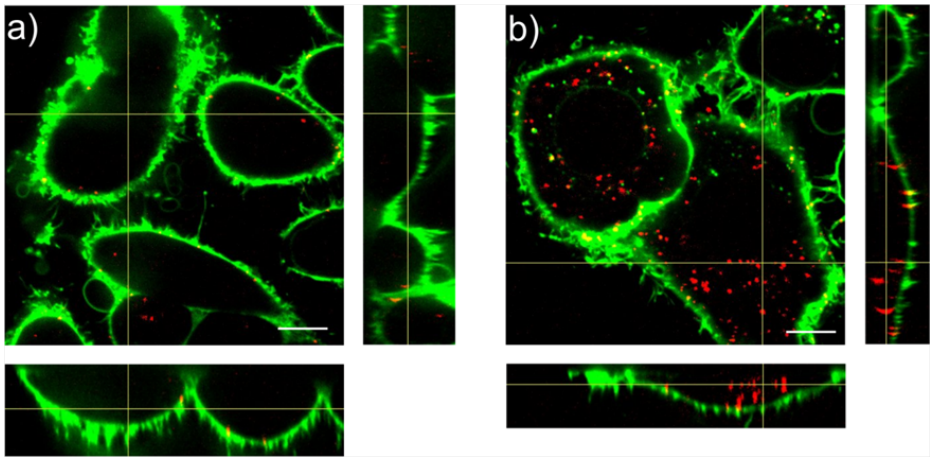

Figure 5.10: Unspecific and receptor-mediated uptake of MSN-PVP-PEG-FA particles by KB cells. (a) Incubation of MSN-PVP-PEG-FA particles with FA pre-incubated KB cells for 2 h at 37 °C. (b) Incubation of MSN-PVP-PEG-FA particles with KB cells, no free FA in cell culture medium, for 2 h at 37 °C. The KB cell membrane is shown in green (WGA 488) and the particles in red (Atto 633). Orthogonal views are given to illustrate the uptake more precisely. The scale bar represents 10 μm.

***In vitro* model.** The attachment of active targeting ligands is important to

achieve a functional drug delivery system.[40] Folic acid was chosen as targeting ligand because it is an ideal model system for targeting with a small molecule and is also believed to be a promising candidate in clinical applications.[41] Furthermore the covalent binding of folic acid to the particles can be achieved with an EDC-mediated coupling and could be easily substituted by other targeting ligands without changing the coupling chemistry. To demonstrate the functionality of the particles, they were incubated on KB-cells, which are known to overexpress FA-receptors.[41] In a competition experiment, with either free folic acid to block the FA-receptors or uninhibited FA-receptors, the uptake of MSN-PVP-PEG-NH_2-FA particles and therefore the targeting abilities were monitored. For the visualization of nanoparticle-uptake, z-stacks of the cells were recorded with a spinning disk confocal fluorescence microscope, which allows us to detect MSNs inside or outside the cell after staining the cell membrane. In Figure 5.10 a, a typical confocal cut through the cells together with the orthogonal projection is shown. In the case of pre-incubation with free folic acid only a few individual particles are present inside the cell (Figure 5.10 a), and also in the full stacks the quasi absence of nanoparticles can be seen, independent of the chosen focal plane. In contrast, incubation of MSN-PVP-PEG-NH_2-FA on KB-cells without pre-incubation of FA resulted in significant uptake of particles (Figure 5.10 b). The particles appear in the representative z-slice as well as in the entire height of the cell as can be seen in the orthogonal views. In the case of blocked receptors there should only occur unspecific uptake, therefore the results indicate the specific folate-receptor mediated endocytosis within two hours with only a minor rate of unspecific uptake.

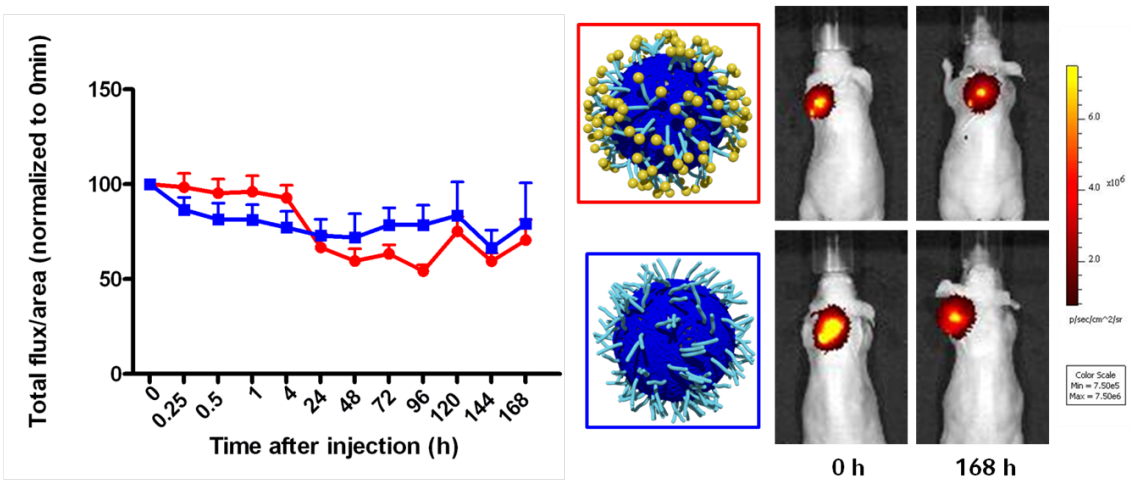

Figure 5.11: Intratumoral administration of MSNs. Left: Retention of MSNs in subcutaneous KB-tumors in mice after intratumoral injection of FA-targeted (red) or untargeted (blue) MSNs over 168 h. Retention was determined by fluorescent signal for the Cy7-labeled MSNs and normalized to 0 min (3 mice per group). Right: Representative pictures of NIR fluorescence imaging of FA-targeted MSNs (top) and untargeted MSNs (bottom).

Prolonged retention in (subcutaneous) tumors of mice. As the multifunctional MSNs have shown to work in vitro, folic acid as targeting ligand was tested further in an *in vivo* setting. For this purpose, Cy7-labeled targeted and untargeted MSNs were injected intratumorally into subcutaneous KB-tumors. Near infrared fluorescence imaging after intratumoral injection revealed that for the first hours the folic acid modification results in a increased retention in the tumor tissue compared to nontargeted particles (Figure 5.11). After more than 24 hours no difference between targeted and untargeted particles is observable. Interestingly, both type of particles show a prolonged retention in tumors for the whole observation period of 7 days (Figure 5.11). This retention in tumors remarkably differs from lower persistence upon intravenous administration (Figure 5.12). The slightly enhanced retention of receptor-targeted over non-targeted MSN particles with cap in the initial phase can be explained by a pronounced washout of non-receptor bound particles into the blood vessel system.

Biodistribution and biocompatibility upon intravenous injection in mice

In a next step, the biodistribution of unfunctionalized MSN and MSN with FA and the cap system was evaluated in vivo. Cy7-labeled MSN were injected in mice (n=3)

via the tail vein. Near infrared fluorescence imaging revealed short circulation times for both particle types. A partial clearance via the kidney detectable due to the bladder signals at 0.5 and 1 hours was observed (Figure 5.12), which is consistent with partial dissociation/disassembly before clearance through the kidneys, as the renal filtration limit is 6 nm in diameter. Preferred accumulation to the liver was observed for several days, with shielded particles having lower signals than unfunctionalized MSN. Importantly, both particle types were well tolerated by the mice and were almost completely excreted after 72 h.

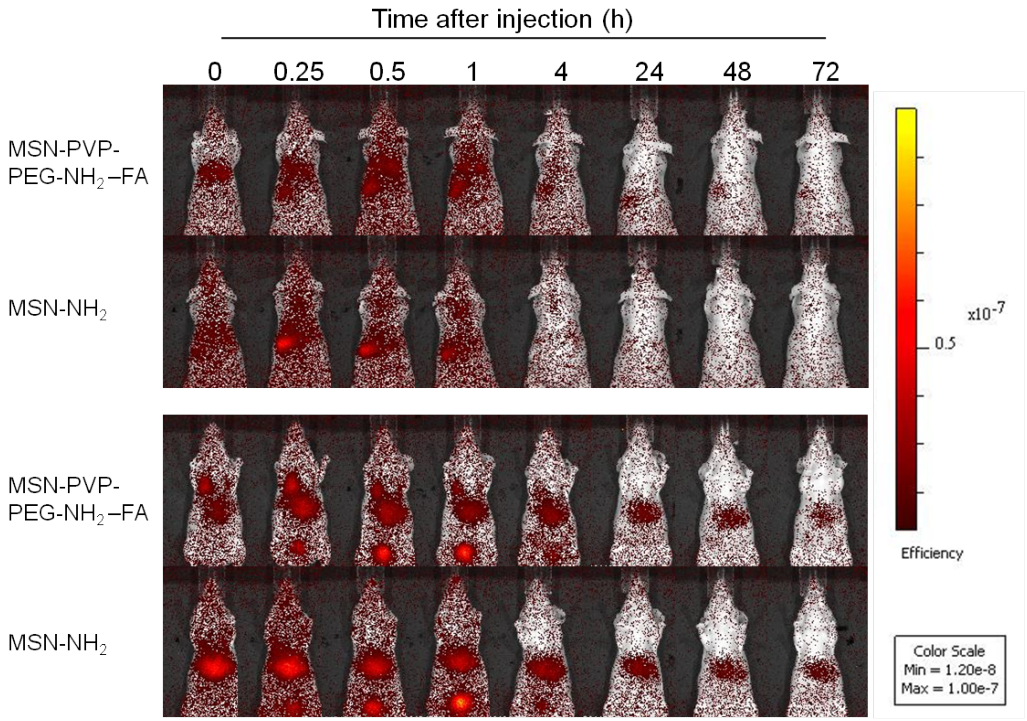

Figure 5.12: Intravenous administration of MSNs. Time dependent distribution of 100 μg per animal Cy7-labeled MSN-PVP-PEG-NH_2-FA or unfunctionalized MSNs over 72 h. Upper panel: ventral position. Lower panel: dorsal position. Experiments were performed in triplicates; a representative mouse of each group is shown.

Stability tests in artificial cell media

To test the ability of the polymer cap system to prevent the mesoporous silica nanoparticles from degradation, biostability assays in Dulbecco's Modified Eagle's Medium (DMEM) at 37 °C and two different pH values (5 and 7) have been per-

formed. As a widely used basal medium for growing many mammalian cells, DMEM contains various amino acids, vitamins and inorganic salts, amongst others, and is used here to simulate a biological environment. Samples were removed after specific times, washed and dried. The nanoparticles were then characterized with transmission electron microscopy and nitrogen sorption. TEM images shown in Figure 5.13 reveal significant degradation of the nanoparticle structure for unfunctionalized MSN after 24 h immersion at pH 7, which is in good agreement with results reported before.[12]

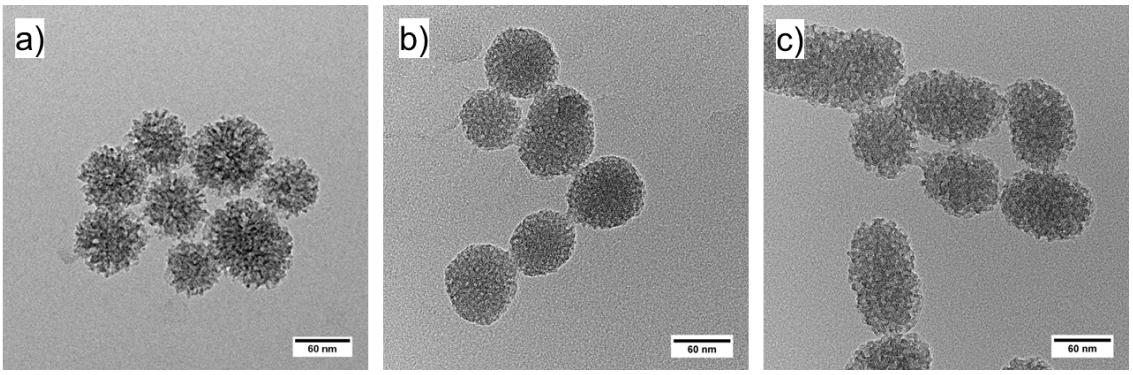

Figure 5.13: TEM images showing MSN after 24 h incubation in DMEM media. (a) MSN pH 7, (b) MSN-PVP-PEG pH 7, (c) MSN-PVP-PEG pH 5.

In contrast, nanoparticles functionalized with PVP offer very good stability in DMEM at pH 7. At this pH, the polymer cap system forms a tight, hydrophobic, and therefore for water, proteins and salts impermeable envelope around the MSN. Additionally, the polymer shell improves the stability of the MSN in DMEM at pH 5, where the cap system is in its open state. In comparison with uncoated nanoparticles, MSN-PVP show less degradation, which was also confirmed by nitrogen sorption experiments (see appendix Figure 5.22). In both cases, the open and the closed state of the cap system, no changes in the pore-size distribution are observed, indicating that the pores are not affected by the media.

Longterm storage stability of loaded MSNs

To demonstrate the good shielding of the silica core by the polymer layer, MSN-PVP-PEG-AlPcS$_{2a}$ particles loaded with calcein were stored at 4 °C without stirring for three weeks. Cell experiments revealed that even after such a long period, the nanoparticles exhibit the same calcein release behaviour as can be seen in Figure 5.14.

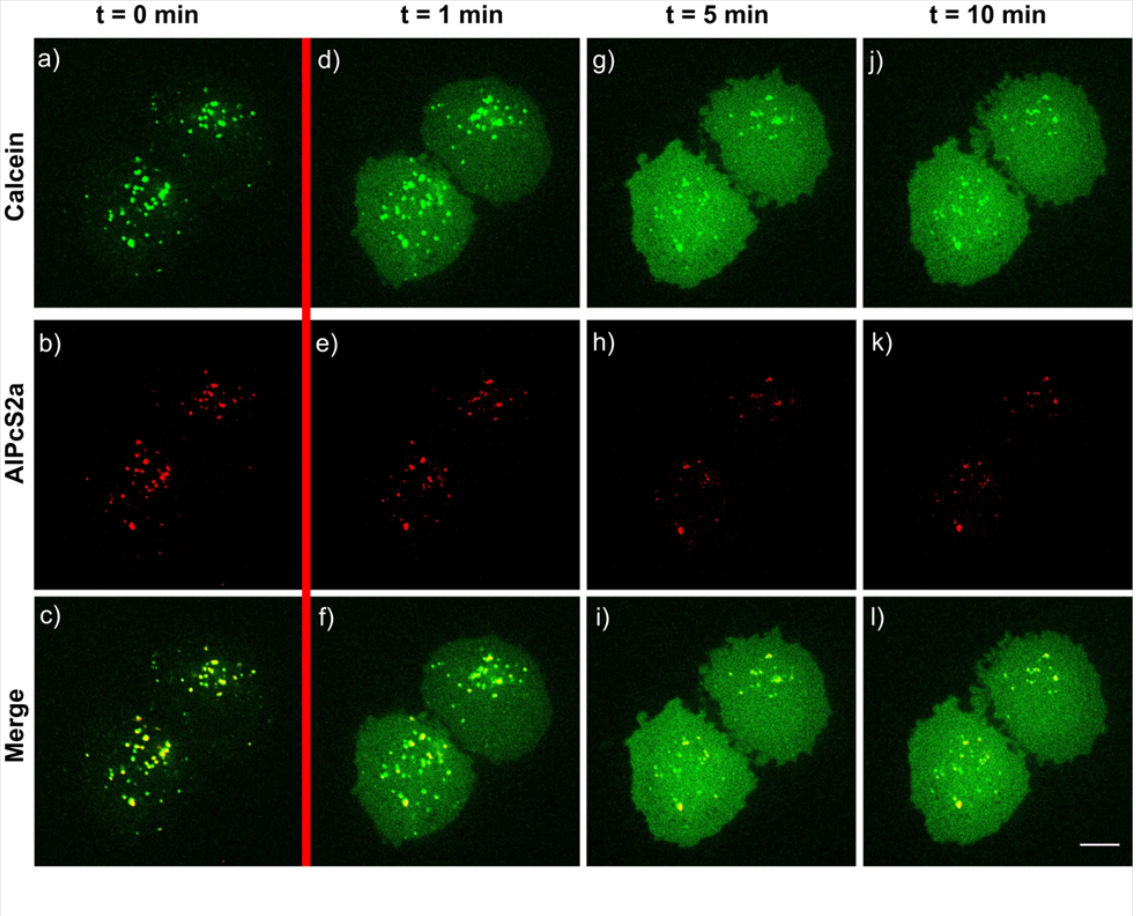

Figure 5.14: Fluorescence microscopy of MSN-PVP-PEG-AlPcS$_{2a}$-FA nanoparticles loaded with calcein inside KB cells, particles have been stored three weeks at 4 °C. (a-c) Calcein (green) and AlPcS$_{2a}$ (red) are co-localized (yellow) prior to photoactivation. The red line indicates photoactivation with 1.2 W / mm^2 of red light (639 nm). (d-f) after 1 min photoactivation, (h-i) 5 min after photoactivation, (j-l) 10 min after photoactivation. The scale bar represents 10 μm.

Conclusions

In this work, we have developed a multifunctional drug delivery vehicle based on polymer-functionalized mesoporous silica nanoparticles. This system combines attractive features such as the high loading capacity of MSNs with the tunable functionality of a polymer. The use of bis-functionalized polymers allowed us to covalently attach step-by-step any functionality of interest. We were able to demonstrate that covalently bound poly(2-vinylpyridine) in combination with a PEG block is able to act as a pH-responsive cap system for MSNs. With this system, we could show the successful delivery of different cargos into cells. Membrane permeable cargos were delivered without any external trigger. Covalent attachment of a red-light-photosensitizer offered the possibility to deliver membrane-impermeable cargos through irradiation with light. Very effective targeting of folic acid receptor expressing cells was enabled by the covalent attachment of folic acid. Stability tests revealed the effectiveness of poly(2-vinylpyridine) not only as cap system, but also as a protecting agent of MSNs against aggressive body fluids. Biodistribution experiments in vivo revealed no agglomeration and an almost complete excretion of the particles within 72 h after intravenous administration in mice. With this new system, we have developed a multifunctional toolbox based on MSNs that is able to open and close its cap depending on the environment. One major advantage of our system derives from the covalent attachment of all components which allows the system to operate for several cycles. We anticipate that the possible integration of almost any functionality of interest as well as the efficient synthesis make this system highly promising for wide-ranging biological and medical applications, especially in cancer therapy.

5.4 Appendix

Dynamic Light Scattering

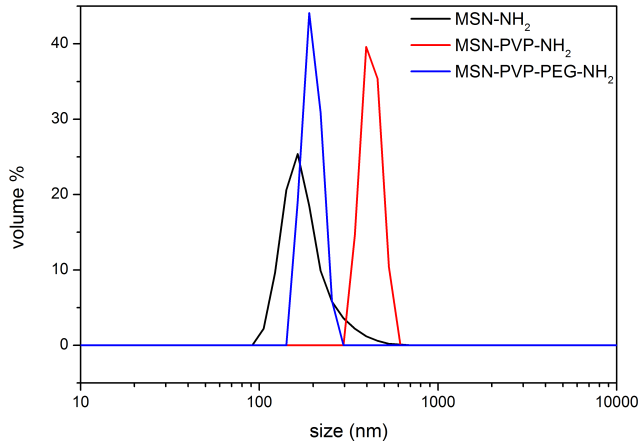

Figure 5.15: DLS data of MSN-NH_2 (black), MSN-PVP-NH_2 (red), MSN-PVP-PEG-NH_2 (blue)

Raman measurements

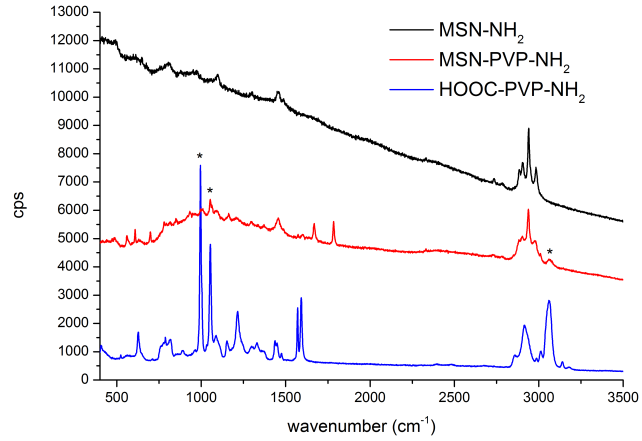

Figure 5.16: Raman spectra of MSN-NH_2 (black), MSN-PVP-NH_2 (red) and HOOC-PVP-NH_2 (blue). Signals from the polymer appearing clearly in the sample MSN-PVP-NH_2 are marked with an asterisc.

Longterm release experiments

Fluorescence spectroscopy

Experimental setup

Fluorescence experiments were performed in order to show the time-dependent release of fluorescein from the mesopores of colloidal mesoporous silica spheres. The measurements were recorded on a PTI fluorescence system featuring a PTI 814 photomultiplier detector and a PTI A1010B Xenon arc lamp driven by a PTI LPS-220B lamp power supply. For temperature settings, a Quantum Northwest TC 125 sample holder was used. Fluorescein was excited with 490 nm and emission was detected at 512 nm (excitation slit 1.0 mm, emission slit 1.0 mm, 1 point per 30 min). For the release experiment, a ROTH Visking Typ 8/32 dialysis membrane with a molecular cut-off of 14000 g/mol was used. An image of this custom made Teflon container can be seen in Figure 5.17.

Figure 5.17: Custom made release experiment setup featuring a 200 μL Teflon tube (a) which is closed by a dialysis membrane (b). This setup is put onto a fluorescence cuvette filled with the desired buffer (c).

1 mg MSN were loaded by redispersing in 500 μL of a 1 mM fluorescein solution and acidified with 50 μL of a citrate/phosphate buffer pH 2. After 12 h, the particles were washed by centrifugation and redispersion in 1 mL SSC buffer pH 7 until no fluorescence was observed in the supernatant. For the release experiment, the particles were redispersed in 200 μL SSC buffer pH 7 and put into a container (see Figure 5.17), which was subsequently closed by a dialysis membrane. The

closed container was then put onto a fluorescence cuvette, which was completely filled with SSC buffer pH 7. The released dye is able to pass through the applied membrane while the relatively larger particles are retained. After 16 h, the particles were centrifuged and redispersed in 200 μL Mc Ilvaine buffer pH 5, put into the container and closed by the dialysis membrane. The closed container was then put onto the fluorescence cuvette, which was completely filled with Mc Ilvaine buffer pH 5. The release was measured every 30 min until no further release was observed. As the fluorescence of fluorescein is strongly dependent on the pH, calibration curves at pH 7 and pH 5 were recorded (Figure 5.18) to be able to compare fluorescence signals in the closed and open state.

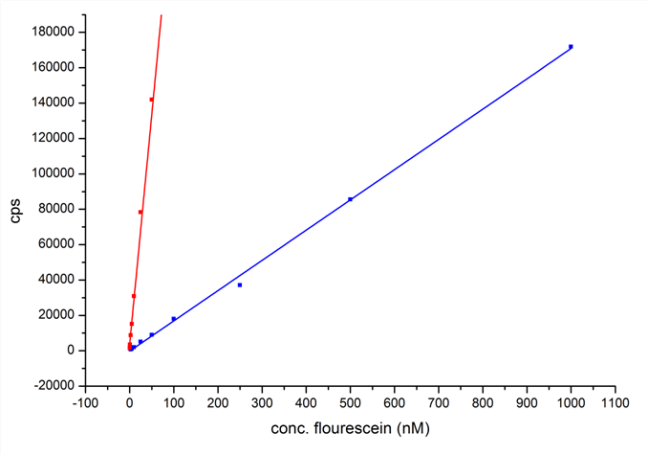

Figure 5.18: Calibration curves of fluorescein at pH 7 (red) and pH 5 (blue).

UV-Vis spectroscopy

The loading capacity of the MSN particles was quantified by UV-Vis spectroscopy. 1 mg particles were loaded with calcein and washed as described above. Afterwards the particles were stirred for 48 h in 1 mL Mc Ilvaine buffer pH 5, centrifuged and the absorption of the supernatant was measured on a Thermo Scientific PeQLab Nanodrop 2000c. For determination of the calcein concentration, a calibration curve of calcein in Mc Ilvaine buffer pH 5 at 495 nm was recorded (Figure 5.19).

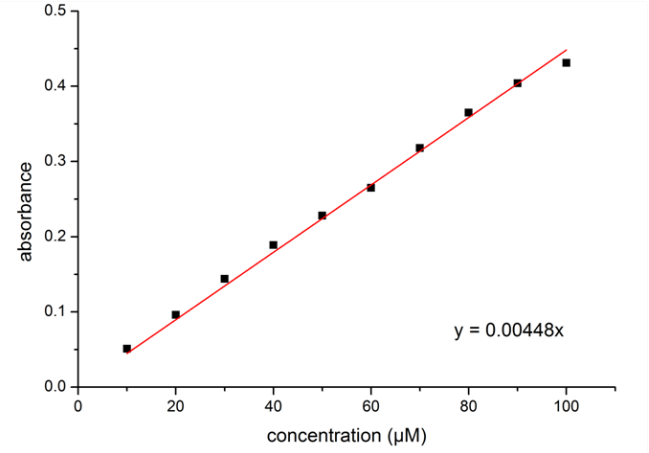

Figure 5.19: Calcein calibration curve.

The measured absorbance at 495 nm of 0.147 leads to a concentration of 32.81 nmol/mL by using a linear regression of the calibration curve. The total amount of calcein released from 1 mg MSN is 0.020 mg.

Release behavior of the membrane permeable cargo colchicine

To show that the entire amount of DAPI was delivered to into the cells by the particles, the supernatant of the sample was tested on cells. The scaling of the pictures within Figure 5.20 is equal, but not the same as for Figure 5.9. Nevertheless it could be clearly observed, that the supernatant alone is not able to stain the nucleus.

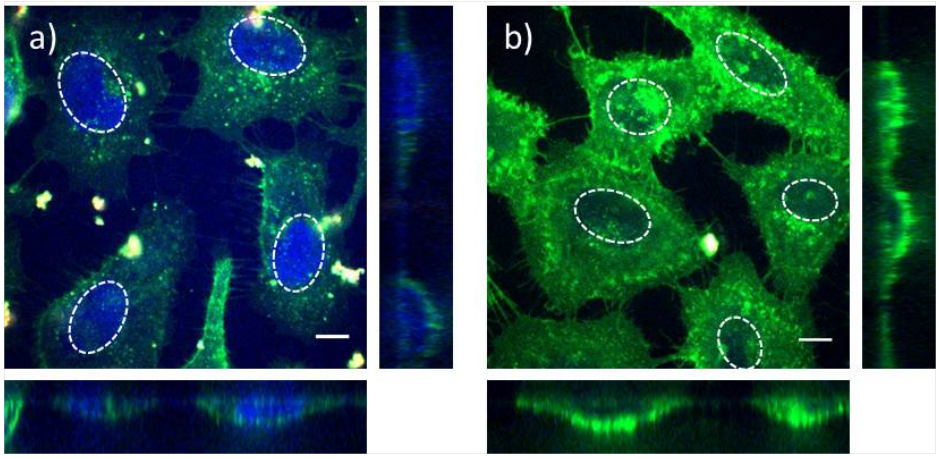

Figure 5.20: Fluorescence microscopy of membrane stained HeLa cells (green) incubated with (a) MSN-PVP-PEG nanoparticles loaded with DAPI (blue) and labeled with Atto 633 (red) after 30 min incubation on the cells and (b) with the supernatant of MSN-PVP-PEG nanoparticles loaded with DAPI. White circles indicate the region of the nuclei. The scale bar represents 10 μm.

Figure 5.21 demonstrates the release of colchicine inside cancer cells. As colchicine hinders the polymerization of the tubulin network, cells with GFP-labeled tubulins were used. In the case of particle addition the tubulin structure is completely destroyed and only a uniform fluorescence across the whole cytoplasm could be detected. In the case of untreated cells the tubulin network can be clearly observed.

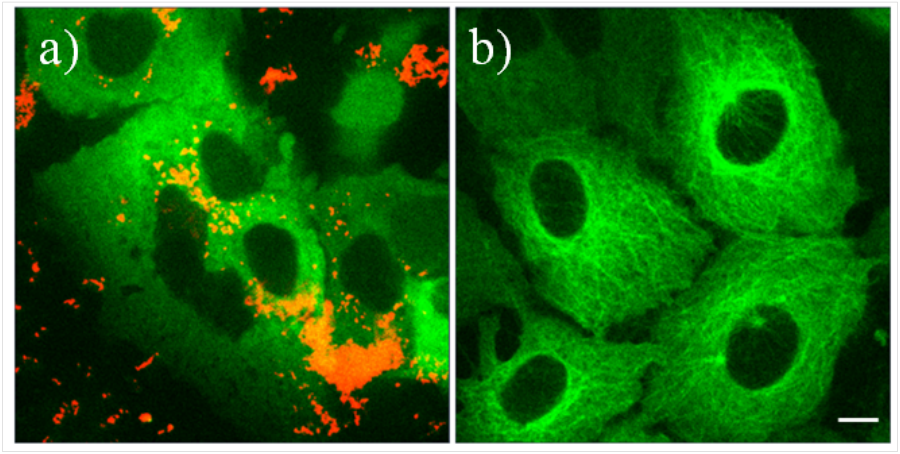

Figure 5.21: Fluorescence microscopy of HuH7 cell expressing tubulin GFP (green). (a)MSN-PVP-PEG nanoparticles loaded with colchicine and labeled with Atto 633 (red) after 18 h incubation on the cells (b) untreated cells. The scale bar represents 10 μm.

Stability tests

Nitrogen sorption

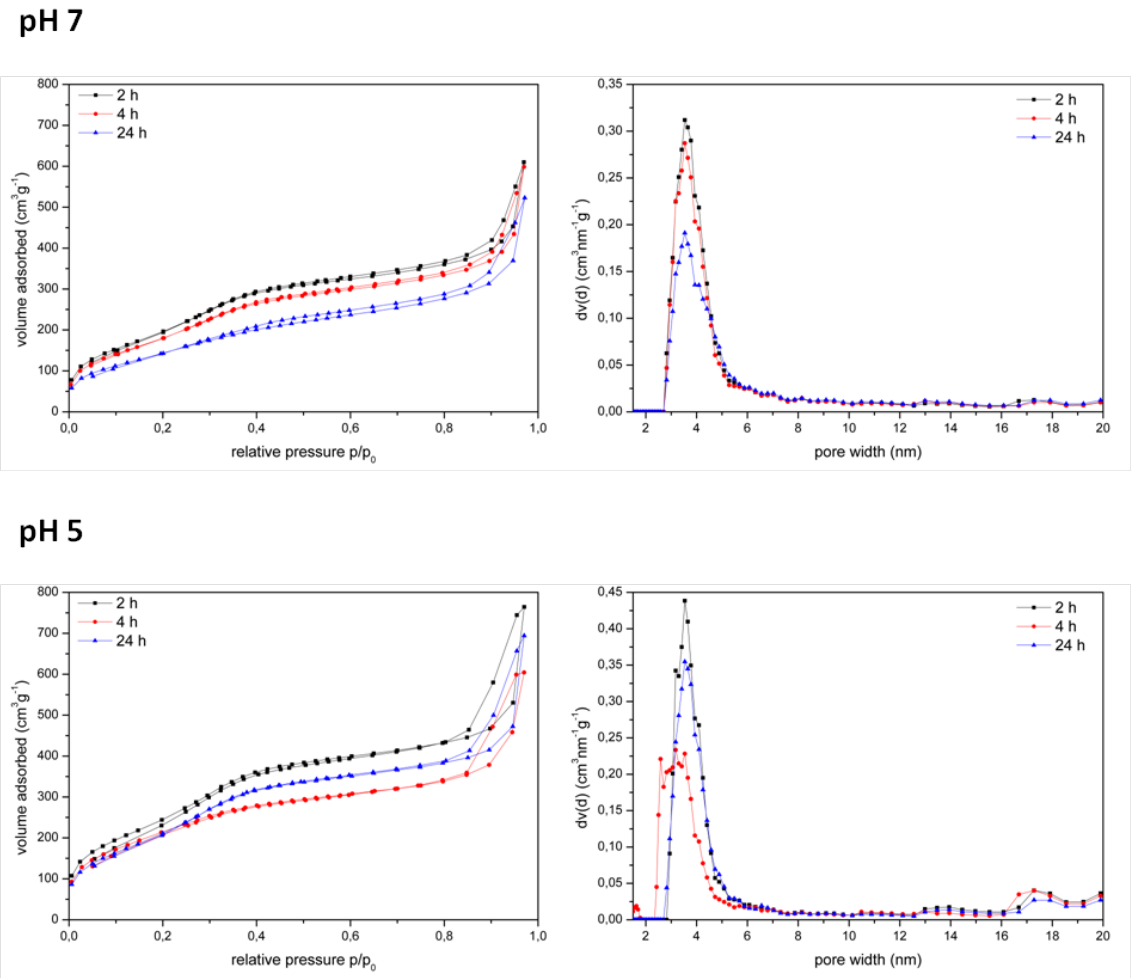

Figure 5.22: Top: Nitrogen sorption isotherms (left) and pore size distributions (right) for different immersion times in DMEM at pH 7. Bottom: Nitrogen sorption isotherms (left) and pore size distributions (right) for different immersion times in DMEM at pH 5.

After immersion of the particles in DMEM for different times at different pH, they were extensively washed and dried from an acidified (some droplets of 0.01 M HCl) aqueous solution at 60 °C to end up with opened particles for sorption experiments. Nitrogen sorption measurements were performed on a Quantachrome Instruments NOVA 4000e at 77 K. It can be seen that all isotherms maintain the shape of a type

4 isotherm. Additionally no significant changes in the NLDFT pore size distribution are observed, which shows that the pore structure is not much affected by the media.

Bibliography

[1] Brewer, E., Coleman, J., and Lowman, A. *Journal of Nanomaterials* , 1 – 10 (2011).

[2] Popat, A., Liu, J., Lu, G. Q. M., and Qiao, S. Z. *J. Mater. Chem.* **22**, 11173–11178 (2012).

[3] Shu, J. Y., Panganiban, B., and Xu, T. *Annual Review of Physical Chemistry* **64**(1), 631–657 (2013). PMID: 23331303.

[4] de Groot, G. W., Santonicola, M. G., Sugihara, K., Zambelli, T., Reimhult, E., Vörös, J., and Vancso, G. J. *ACS Applied Materials & Interfaces* **5**(4), 1400–1407 (2013).

[5] Synytska, A., Stamm, M., Diez, S., and Ionov, L. *Langmuir* **23**(9), 5205–5209 (2007).

[6] Meyer, M., Dohmen, C., Philipp, A., Kiener, D., Maiwald, G., Scheu, C., Ogris, M., and Wagner, E. *Molecular Pharmaceutics* **6**(3), 752–762 (2009).

[7] Mickler, F. M., Möckl, L., Ruthardt, N., Ogris, M., Wagner, E., and Bräuchle, C. *Nano Letters* **12**(7), 3417–3423 (2012).

[8] Albertazzi, L., Mickler, F. M., Pavan, G. M., Salomone, F., Bardi, G., Panniello, M., Amir, E., Kang, T., Killops, K. L., Bräuchle, C., Amir, R. J., and Hawker, C. J. *Biomacromolecules* **13**(12), 4089–4097 (2012).

[9] Vetter, A., Virdi, K. S., Espenlaub, S., Rödl, W., Wagner, E., Holm, P. S.,

Scheu, C., Kreppel, F., Spitzweg, C., and Ogris, M. *Molecular Pharmaceutics* **10**(2), 606–618 (2013).

[10] Minard-Basquin, C., Weil, T., Hohner, A., Rädler, J. O., and Müllen, K. *Journal of the American Chemical Society* **125**(19), 5832–5838 (2003). PMID: 12733924.

[11] Arpicco, S., Stella, B., Schiavon, O., Milla, P., Zonari, D., and Cattel, L. *International Journal of Pharmaceutics* **454**(2), 653 – 659 (2013).

[12] Cauda, V., Argyo, C., and Bein, T. *J. Mater. Chem.* **20**, 8693–8699 (2010).

[13] Zhou, Z., Ma, X., Jin, E., Tang, J., Sui, M., Shen, Y., Kirk, E. A. V., Murdoch, W. J., and Radosz, M. *Biomaterials* **34**(22), 5722 – 5735 (2013).

[14] Coti, K. K., Belowich, M. E., Liong, M., Ambrogio, M. W., Lau, Y. A., Khatib, H. A., Zink, J. I., Khashab, N. M., and Stoddart, J. F. *Nanoscale* **1**, 16–39 (2009).

[15] Schlossbauer, A., Dohmen, C., Schaffert, D., Wagner, E., and Bein, T. *Angewandte Chemie International Edition* **50**(30), 6828–6830 (2011).

[16] Slowing, I. I., Trewyn, B. G., Giri, S., and Lin, V. S.-Y. *Advanced Functional Materials* **17**(8), 1225–1236 (2007).

[17] Mackowiak, S. A., Schmidt, A., Weiss, V., Argyo, C., von Schirnding, C., Bein, T., and Bräuchle, C. *Nano Letters* **13**(6), 2576–2583 (2013).

[18] Schlossbauer, A., Sauer, A. M., Cauda, V., Schmidt, A., Engelke, H., Rothbauer, U., Zolghadr, K., Leonhardt, H., Bräuchle, C., and Bein, T. *Advanced Healthcare Materials* **1**(3), 316–320 (2012).

[19] Cauda, V., Schlossbauer, A., Kecht, J., Zürner, A., and Bein, T. *Journal of the American Chemical Society* **131**(32), 11361–11370 (2009).

[20] Schlossbauer, A., Warncke, S., Gramlich, P., Kecht, J., Manetto, A., Carell, T., and Bein, T. *Angewandte Chemie International Edition* **49**(28), 4734–4737 (2010).

[21] Sauer, A. M., Schlossbauer, A., Ruthardt, N., Cauda, V., Bein, T., and Bräuchle, C. *Nano Letters* **10**(9), 3684–3691 (2010).

[22] Ashley, C. E., Carnes, E. C., Phillips, G. K., Padilla, D., Durfee, P. N., Brown, P. A., Hanna, T. N., Liu, J., Phillips, B., Carter, M. B., Carrol, N. J., Jiang, X., Dunphy, D. R., Willman, C. L., Petsev, D. N., Evans, D. G., Parikh, A. N., Chackerian, B., Wharton, W., Peabody, D. S., and Brinker, C. J. *Nature Materials* **10**, 389–397 (2011).

[23] Liu, R., Liao, P., Liu, J., and Feng, P. *Langmuir* **27**(6), 3095–3099 (2011).

[24] Tarn, D., Xue, M., and Zink, J. I. *Inorganic Chemistry* **52**(4), 2044–2049 (2013).

[25] Vivero-Escoto, J. L., Slowing, I. I., Wu, C.-W., and Lin, V. S.-Y. *Journal of the American Chemical Society* **131**(10), 3462–3463 (2009).

[26] You, Y.-Z., Kalebaila, K. K., Brock, S. L., and , D. O. *Chemistry of Materials* **20**(10), 3354–3359 (2008).

[27] Harush-Frenkel, O., Debotton, N., Benita, S., and Altschuler, Y. *Biochemical and Biophysical Research Communications* **353**(1), 26 – 32 (2007).

[28] Lakadamyali, M., Rust, M. J., Babcock, H. P., and Zhuang, X. *Proceedings of the National Academy of Sciences* **100**(16), 9280–9285 (2003).

[29] Varkouhi, A. K., Scholte, M., Storm, G., and Haisma, H. J. *Journal of Controlled Release* **151**(3), 220 – 228 (2011).

[30] Hong, C.-Y., Li, X., and Pan, C.-Y. *J. Mater. Chem.* **19**, 5155–5160 (2009).

[31] Sun, J.-T., Hong, C.-Y., and Pan, C.-Y. *The Journal of Physical Chemistry C* **114**(29), 12481–12486 (2010).

[32] Atkin, R., Bradley, M., and Vincent, B. *Soft Matter* **1**, 160–165 (2005).

[33] Huotari, J. and Helenius, A. *The EMBO Journal* **30**, 3481–3500 (2011).

[34] Salokhiddinov, K., Byteva, I., and Gurinovich, G. *Journal of Applied Spectroscopy* **34**(5), 561–564 (1981).

[35] Brasseur, N., Ouellet, R., La Madeleine, C., and van Lier, J. E. *British Journal of C* **80**, 1533–1541 (1999).

[36] Zink, D., Sadoni, N., and Stelzer, E. *Methods* **29**(1), 42 – 50 (2003).

[37] Lalande, M. E., Ling, V., and Miller, R. G. *Proceedings of the National Academy of Sciences* **78**(1), 363–367 (1981).

[38] Kapuscinski, J. *Journal of Histochemistry & Cytochemistry* **38**(9), 1323–9 (1990).

[39] Cho, K., Wang, X., Nie, S., Chen, Z. G., and Shin, D. M. *Clinical Cancer Research* **14**(5), 1310–1316 (2008).

[40] Huynh, N. T., Roger, E., Lautram, N., Benoit, J.-P., and Passirani, C. *Nanomedicine* **5**, 1415–1433 (2010).

[41] Salazar, M. D. A. and Ratnam, M. *Cancer and Metastasis Reviews* **26**(1), 141–152 (2007).

Chapter 6

Polymer-Capped Metal-Organic Framework Nanoparticles for Controlled Release Applications

The following work is based on a project with Andreas Zimpel and Stefan Wuttke

6.1 Introduction

Metal-organic frameworks (MOFs) describe a family of porous materials with crystalline architectures created by coordinative bonding between metal ion centers and organic linker molecules.[1] Besides their tremendous structural variety, high porosity and sometimes enormous surface area (up to 6000 m^2 g^{-1}), MOFs contain two further advantages that are useful for bio-applications.[2] One major benefit is the ability of tailoring the pore functionality by incorporation of additional side chains into the linker molecules. By controlling the host-guest interactions in the porous system, it should be possible to precisely regulate drug release kinetics. Another advantage of MOFs is the biocompatibility and biodegradability of so-called "BioMOFs".[3–7] Since the discovery of MOFs with particle sizes in the range of 30 - 200 nm,[8] this class of materials became highly interesting for the development of MOF-based drug delivery carriers. The high loading capacity of MOFs was reported by Horcajada

et al.. They were able to load 1.38 g ibuprofen to 1 g dehydrated MIL-101(Cr) material.[9] Lin *et al.* demonstrated the incorporation of the anticancer drug cisplatin into a Tb^{3+} based metal-organic framework.[10] The covalent attachment of drug molecules to anchoring groups of the linkers in the pores was demonstrated by Taylor-Pashow *et al.*.[11] In this system, the release of the drug relied on the complete degradation of the MOF itself.

In this chapter, we report on the ability of creating a polymer-based cap system around MOF nanoparticles to demonstrate pH-responsive release behavior. It should be noted, that on-demand delivery of molecules (e.g. drugs), encapsulated within a MOF nanocarrier, has not been established to date. Therefore we transferred the concept of the PVP cap system that showed good results for MSNs to MIL-101(Cr) nanoparticles, serving as model system. MIL-101(Cr) consists of Cr^{3+} metal centers that are connected by terephthalic acid linker molecules.[12] This system was chosen due to its outstanding stability of the crystalline porous framework, even if chromium-based materials may not be the best choice for biomedical applications. As the polymer cap system offers the possibility of reversible opening and closure, the nanoparticular core should feature high stability to maintain the covalent attachment of the cap system.

6.2 Experimental Section

Synthesis of MIL-101(Cr) nanoparticles

For the microwave synthesis of MIL-101(Cr) nanoparticles, chromium(III) nitrate nonahydrate (1.48 g, 3.70 mmol) and terephthalic acid (615 mg, 3.70 mmol) were heated in 20 mL H_2O bidest. to 220 °C under solvothermal conditions (p = 18 bar) within four minutes. The mixture was kept at 220 °C for two minutes and the resulting suspension was cooled down to room temperature. The resulting nanoparticles were separated from the additional bulk material by filtration. For purification, the filtrate was washed four times by centrifugation (1^{st}: 20000 rpm (45417 rcf), 60 min; 2^{nd}-4^{th}: 20000 rpm, 45 min) followed by redispersion in ethanol.

Protection of NH_2-PVP-COOH (Boc-PVP-COOH)

To a solution of 500 mg (5 μmol) NH_2-PVP-COOH in 10 mL dry dichloromethane, 15 μL (0.11 mmol) triethylamine and 15 mg (6.9 μmol) Boc anhydride were added. The solution was stirred overnight and extracted several times with brine. The organic phase was dried over $MgSO_4$ and evaporated to dryness to afford the Boc protected polymer. The polymer was used without further purification.

Reaction of MIL-101(Cr) with ethylenediamine (MIL-NH_2)

To convert free standing carboxylic acid functionalities of MIL-101(Cr) into amino groups, the nanoparticles were reacted with ethylenediamine. 150 mg MIL-101(Cr) in 40 mL ethanol were mixed with an excess ethylenediamine (100 μL). Subsequently, 50 μL EDC were added and the mixture was stirred at room temperature. After 1 h, the particles were washed three times by centrifugation (20000 rpm, 45 min) and redispersion in ethanol.

General procedure for the attachment of poly(2-vinyl pyridine) to MIL-NH_2 (MIL-PVP-Boc)

To a dispersion of 100 mg MIL-NH_2 in 10 mL ethanol, 120 mg (10.2 μmol) polymer dissolved in 3 mL ethanol was added. The amidation was activated by the addition of 20 μL (114.4 μmol) EDC and 2.6 mg (12 μmol) Sulfo-NHS. The mixture was stirred at room temperature for 12 h. Afterwards the particles were separated by centrifugation (19000 rpm, 20 min) and washed three times by repeated centrifugation and redispersion in 30 mL ethanol.

Deprotection of MIL-PVP-Boc (MIL-PVP-NH_2)

Deprotection of the polymer was achieved through stirring 10 mg polymer-functionalized particles in a mixture of 2 mL trifluoroacetic acid and 8 mL water for 24 h. After deprotection, the particles were extensively washed by centrifugation (19000 rpm, 20 min) and redispersion in a 1:1 mixture of water and ethanol.

Conversion of MIL-PVP-NH_2 to MIL-PVP-COOH

10 mg MIL-PVP-NH_2 in 2 mL ethanol were reacted with an excess of oxalic acid (5 mg, 55 μmol) and EDC (9 μL, 51 μmol) for 1 h. Afterwards the particles were extensively washed by centrifugation (19000 rpm, 20 min) and redispersion in a 1:1 mixture of water and ethanol.

PEGylation of MIL-PVP-COOH (MIL-PVP-PEG-NH_2)

To a dispersion of 1 mg MIL-PVP-COOH in 500 μL ethanol, 2 mg (100 nmol) NH_2-PEG-NH_2 in 500 μL bidistilled water was added and the reaction was started through the addition of 0.5 μL (2.8 μmol) EDC. After stirring for 1 h at room temperature, the sample was washed three times by centrifugation with a mixture of ethanol:water 1:1.

Release experiments:

Dye loading

The amount of 1 mg MIL-PVP-PEG-NH_2 was dispersed in 500 μL of a 1 mM dye solution in water. To open the pores and enable the uptake, 50 μL of citrate buffer (pH 2) was added. The particles were stirred overnight, centrifuged, and redispersed in 1 mL SSC buffer (pH 7) to trigger closure of the polymer shell. The particles were washed extensively with SSC buffer until no fluorescence was detected in the supernatant.

Fluorescein release

1 mg fluorescein loaded MIL-PVP-NH_2 or MIL-PVP-PEG-NH_2 was redispersed in 200 μL SSC buffer and transferred to the cap of the fluorescence cuvette. This cap is sealed with a dialysis membrane (molecular weight cutoff of 14000 g/mol) and placed on top of the fluorescence cuvette, which is also filled with SSC buffer. The "release" of fluorescein out of the closed particles was monitored for 2 h (λ_{ex} = 490 nm, λ_{em} = 512 nm). Subsequently, the cap was removed and the particles were centrifuged and

redispersed in 200 μL citrate-phosphate buffer (pH 5), before being put into the cap of the release setup. The fluorescence cuvette was also filled with citrate-phosphate buffer (pH 5). After reassembling of the release setup, the release of fluorescein was measured for 10 h continuously. For comparison of the obtained curves, calibration curves of fluorescein in SSC buffer (pH 7) and in citrate-phosphate buffer (pH 5) were recorded.

6.3 Results and Discussions

Particle characterization

MIL-101(Cr) nanoparticles were prepared in a solvothermal microwave-assisted synthesis. After adjustment of the synthetic conditions, MIL-101(Cr) nanoparticles consisting of Cr^{3+} centers conected by terephthalic acid molecules (Figure 6.1) were obtained.

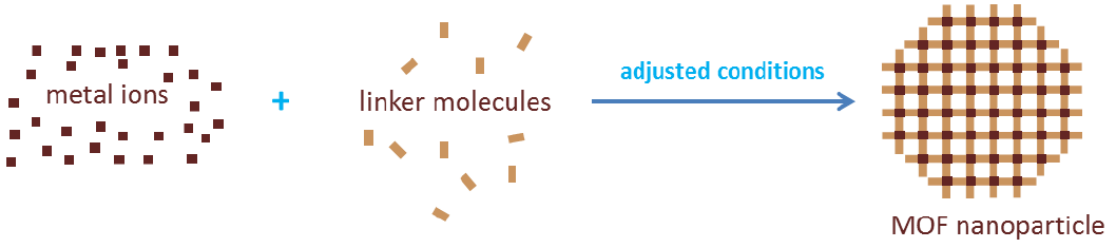

Figure 6.1: Scheme of the nanoparticle synthesis. Figure was taken from the Master thesis of Andreas Zimpel.

DLS measurements of the resulting nanoparticles in ethanol reveal a mean diameter of around 60 nm (Figure 6.2) with some aggregated particles in the sample. These results are in good agreement with data obtained by TEM (Figure 6.6).

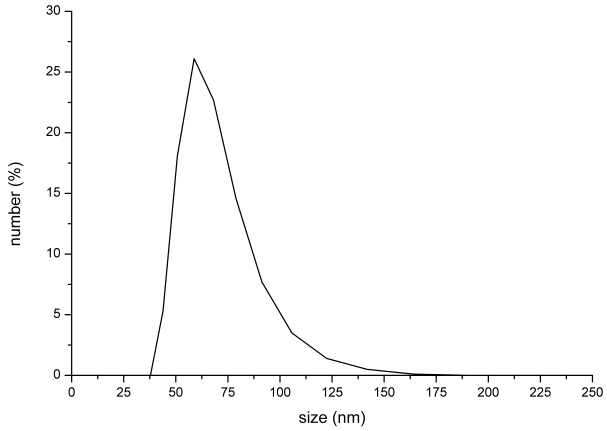

Figure 6.2: DLS data of MIL-101(Cr) nanoparticles in ethanol.

Nitrogen sorption experiments revealed a BET surface area of 2778 m^2/g and a multimodal pore size distribution with maxima at 1.8 nm, 2.5 nm and 3.2 nm, which is in good agreement with the literature.[2]

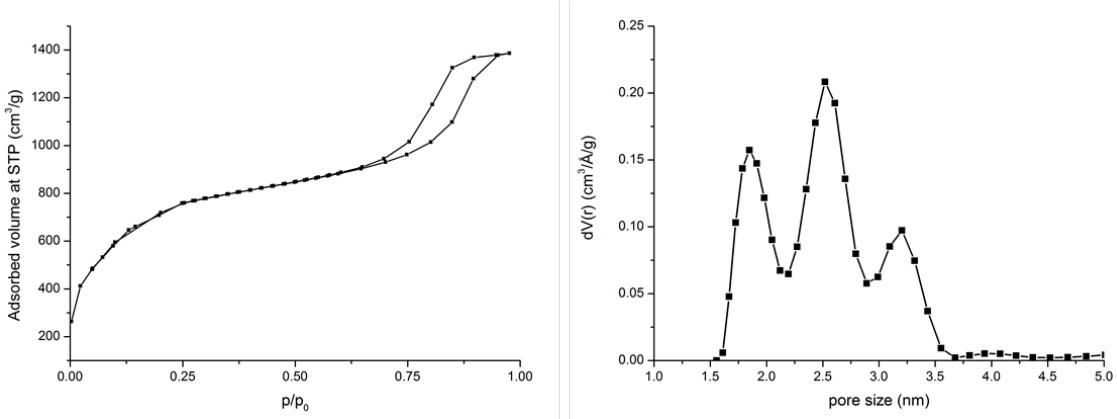

Figure 6.3: Left: Nitrogen sorption data of MIL-101(Cr) nanoparticles. Right: DFT pore size distribution.

For the use of MIL-101(Cr) as drug delivery vehicle, a cap system based on poly(2-vinyl pyridine) was attached. In a first step, the carboxylic acid moieties on the external surface of the nanoparticles were reacted with ethylenediamine to create an anchoring point for PVP (MIL-NH_2). PVP was attached to the amine residues followed by deprotection (MIL-PVP-NH_2). Finally, anchoring of PEG led to a water dispersible drug delivery system (MIL-PVP-PEG-NH_2). Each synthetic step was monitored by IR and zeta potential measurements.

Infrared spectroscopy

The as synthesized MIL-101(Cr) nanoparticles showed a significant signal at 1708 cm^{-1} that can be attributed to the C=O stretching vibration of terminal carboxylic acid moieties (Figure 6.4). After reaction with ethylenediamine a reduced intensity of the C=O vibration was observed. A new signal at 1590 cm^{-1}, corresponding to the N-H deformation vibration of terminal aliphatic amines was found. Additionally, the broadening of the signal between 1660 cm^{-1} and 1520 cm^{-1} points to the successful creation of amide bonds, as these signals appear in this region.

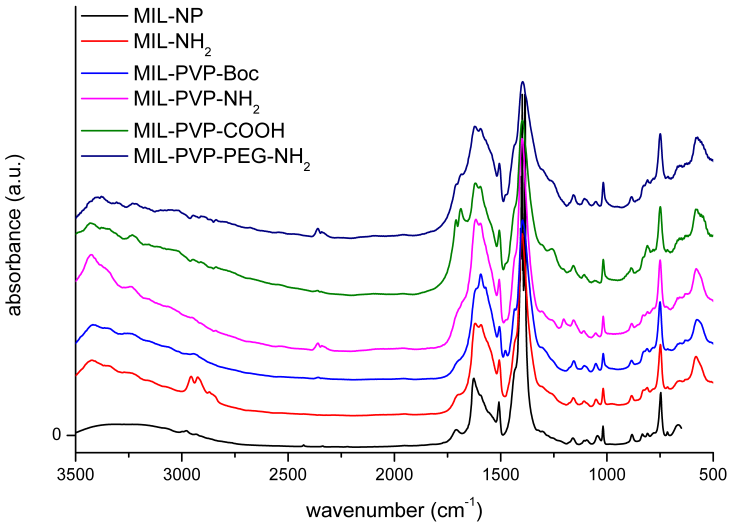

Figure 6.4: IR data of each synthetic step of the MIL based drug delivery vehicle.

Further attachment of PVP to MIL-NH_2 was shown by the rise in intensity of the signals at 1594 cm^{-1} and 1478 cm^{-1} that can be clearly attributed to PVP by comparison with the spectra of the pure polymer. Deprotection of the terminal amino-functionality of PVP did not lead to significant changes in IR. For further attachment of PEG, the terminal amino-functionality was converted into a carboxylic acid by attachment of oxalic acid. The success of the reaction was observed by the appearance of two new peaks at 1712 cm^{-1} for to the C=O stretching vibration of

COOH and 1688 cm^{-1} for the corresponding carboxylate anion. After attachment of PEG, the peaks of the terminal acid groups vanished and thus proving the successful reaction.

Zeta potential

Additionally to IR, each step of the synthesis was also monitored by zeta potential measurements (Figure 6.5). For as synthesized MIL-101(Cr) nanoparticles, a zeta potential of +24 mV was measured at pH 2. An increase in zeta potential was observed after the reaction with ethylenediamine due to the conversion of terminal carboxylic acid- into amino moieties. A significant change in zeta potential up to a value of +39 mV was recorded after attachment of PVP. At pH 2, PVP is present in the fully protonated state resulting in the creation of a highly positively charged particle surface.

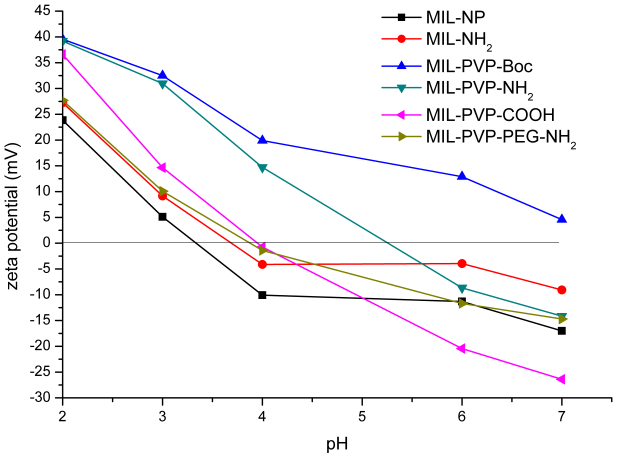

Figure 6.5: Zeta potential data of each synthetic step of the MIL based drug delivery vehicle.

After complete synthesis, the nanoparticles were investigated with TEM and XRD and these data were compared to data obtained after synthesis of MIL-101(Cr) (Figure 6.6). XRD measurements revealed no significant changes in crystallinity. The smoothing of reflexes in MIL-PVP-PEG can be explained by the introduction of a high amount of organic polymers. TEM micrographs were taken to obtain infor-

mation on the crystallinity, morphology and aggregation behaviour of the nanoparticles.

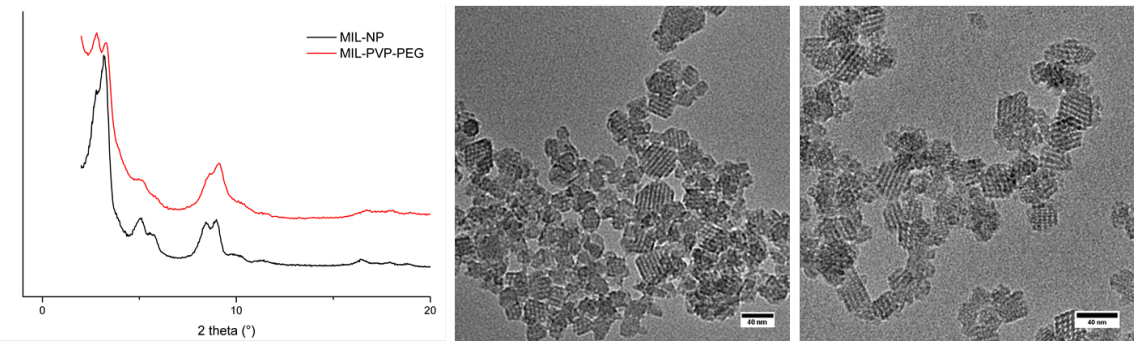

Figure 6.6: Left: XRD pattern of MIL nanoparticles before (black) and after attachment of the polymer cap system. Middle: TEM micrograph of MIL-101(Cr) nanoparticles. Right: TEM micrograph of MIL-PVP-PEG.

In Figure 6.6 it can be seen that after synthesis of MIL-101(Cr) crystalline nanoparticles with sizes in the range of 30 to 60 nm were obtained. These nanocrystals often exhibit an octahedron-like morphology, which is in accordance with the fact that MIL-101(Cr) belongs to the cubic space group. In the TEM image of MIL-101(Cr) no intergrown particles were observed. TEM micrographs of MIL-PVP-PEG-NH_2 yielded similar results compared to MIL-101(Cr), from which we can conclude that the nanoparticles were not affected by the demanding synthesis conditions (e. g. stirring in trifluoroacetic acid for 24 h) for the polymer cap system.

Release experiments

To test the ability of MIL-PVP-PEG nanoparticles to act as a pH responsive drug delivery system, release experiments were performed in the same way as already described in chapter 5. In summary, MIL-PVP-PEG nanoparticles were loaded with a fluorescent dye by stirring in an acidified solution. Closure of the nanoparticles was obtained by centrifugation and redisperion in SSC buffer at pH 7. After washing the nanoparticles, the sample was measured in our release setup in the closed state. The release was triggered by exchanging the buffer to reach a pH of5. Figure 6.7 shows the resulting release curve of MIL-PVP-PEG.

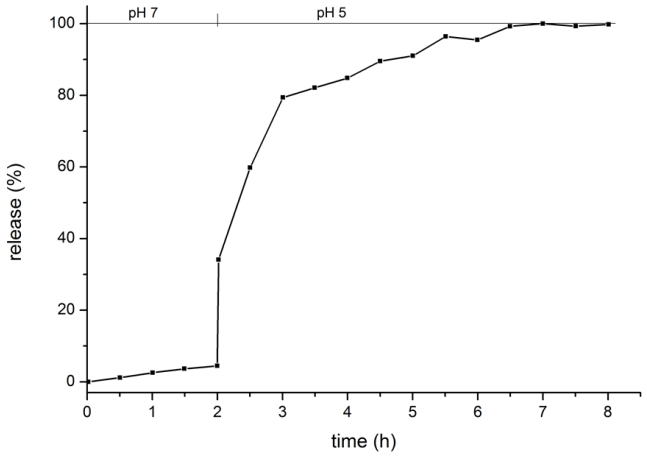

Figure 6.7: Release data obtained for MIL-PVP-PEG nanoparticles.

Analysis of the release data revealed a premature release of fluorescein of 4.5% within 2 h. A burst of release was observed after opening of the cap system leading to a complete release of the dye within 4.5 h. Compared with mesoporous silica nanoparticles capped with PVP, a slightly higher premature release was recorded. This might be due to sharp edges of the MIL nanocrystals leading to incomplete coverage of the particles with a tight polymer layer. Another possible explanation is the relative small amount of accessible anchor molecules at the particle surface, as with terephthalic acid a bifunctional linker bearing only two carboxyl functionalities was used for particle synthesis. However, these first release experiments clearly prove the ability of PVP to act as a cap system for MOF nanoparticles.

6.4 Conclusions

In this chapter a drug delivery system based on MIL-101(Cr) nanoparticles covered with a pH-responsive polymer was reported. We could demonstrate that it is possible to functionalize the nanoparticles with poly(2-vinyl pyridine) without affecting the shape and crystallinity of the nanoparticles. Finally, the ability of the system to act as a potetial drug delivery vehicle was demonstrated by *in vitro* release experiments of a model drug. In comparison with PVP-capped MSN systems, a slightly more pronounced premature release was observed for MIL-MSN-PVP. In future work, it will be examined if the creation of further anchor groups on the surface of the MOF

nanoparticles can lead to the attachment of an increased amount of polymer, and thus, leading to a more effecting sealing of the system.

Bibliography

[1] Chae, H. K., Siberio-Perez, D. Y., Kim, J., Go, Y. B., Eddaoudi, M., Matzger, A. J., O'Keeffe, M., and Yaghi, O. M. *Nature* **427**, 523–527 (2004).

[2] Ferey, G., Mellot-Draznieks, C., Serre, C., Millange, F., Dutour, J., Surble, S., and Margiolaki, I. *Science* **309**(5743), 2040–2042 (2005).

[3] Serre, C., Millange, F., Surble, S., and Ferey, G. *Angewandte Chemie International Edition* **43**(46), 6285–6289 (2004).

[4] Surble, S., Serre, C., Mellot-Draznieks, C., Millange, F., and Ferey, G. *Chem. Commun.* , 284–286 (2006).

[5] Whitfield, T. R., Wang, X., Liu, L., and Jacobson, A. J. *Solid State Sciences* **7**(9), 1096 – 1103 (2005).

[6] Horcajada, P., Surble, S., Serre, C., Hong, D.-Y., Seo, Y.-K., Chang, J.-S., Greneche, J.-M., Margiolaki, I., and Ferey, G. *Chem. Commun.* , 2820–2822 (2007).

[7] Bauer, S., Serre, C., Devic, T., Horcajada, P., Marrot, J., Ferey, G., and Stock, N. *Inorganic Chemistry* **47**(17), 7568–7576 (2008).

[8] Carne, A., Carbonell, C., Imaz, I., and Maspoch, D. *Chem. Soc. Rev.* **40**, 291–305 (2011).

[9] Horcajada, P., Serre, C., Vallet-Regi, M., Sebban, M., Taulelle, F., and Ferey, G. *Angewandte Chemie International Edition* **45**(36), 5974–5978 (2006).

[10] Rieter, W. J., Pott, K. M., Taylor, K. M. L., and Lin, W. *Journal of the American Chemical Society* **130**(35), 11584–11585 (2008).

[11] Taylor-Pashow, K. M. L., Rocca, J. D., Xie, Z., Tran, S., and Lin, W. *Journal of the American Chemical Society* **131**(40), 14261–14263 (2009).

[12] Jhung, S. H., Lee, J.-H., Yoon, J. W., Serre, C., Ferey, G., and Chang, J.-S. *Advanced Materials* **19**(1), 121–124 (2007).

Chapter 7

Mesoporous Silica Nanoparticles for Immunoassay applications

The following work is based on a collaboration with Elisangela Linares and Stefan Thalhammer

7.1 Introduction

In the developing world, there is a lack of convenient and accurate tools that diagnose diseases and other health problems. As a result, many health risks remain undetected or receive inappropriate treatment. Among the diseases, dengue fever (DF) is classified as a neglected disease, and has emerged as a rapidly spreading vector-borne disease mainly in developing countries.[1] DF results from infection with a virus transmitted mainly by *Aedes aegypti*, a species of mosquito with a global distribution. Over 2.5 billion people are now endangered by dengue. The World Health Organization estimates 100 million cases of dengue fever and 500 thousand cases of dengue hemorrhagic fever (DHF) with 2.5% of annual mortality from DHF.[2] The disease is now endemic in more than 100 countries in Africa, America, Eastern Mediterranean, South-east Asia and Western Pacific. For DHF, medical care can save numerous lives, decreasing mortality rates from more than 20% to less than 1%.[3]

For DF, as for many other diseases, numerous barriers exist for early diagnosis in impoverished environments, including poor laboratory infrastructure, low financial support, harsh environmental conditions and unskilled people. The current techniques used in laboratories suffer from problems, starting from the storage. The high temperatures and the large variations in humidity limit the shelf life and the efficiency of the available assays. Some diagnostic devices based on dried chemicals have been used as an alternative to the conventional assays, but they still show limitations in sensitivity, reproducibility, and may require expensive readers. Lateral flow immunoassays are a promising alternative, but the lack of sensitivity and the difficulties to quantify analytes limit its application as substitute for more common techniques. Among the current diagnostic tools, enzyme linked immunosorbent assay (ELISA) is the most commonly used serological technique for diagnosis. The method is based on the principle of a solid phase enzyme-linked immunosorbent assay with colorimetric detection. The detection signal is based on the reaction between an enzyme-labeled antibody and a substrate, whose product is colorful and where the intensity is (inversely) proportional to the analyte concentration, depending on the used arrangement. ELISA offers a sensitive and specific approach with typical detection limits in the low ng/ml range. In some applications, ELISA shows superior performance than virus isolation and real-time polymerase chain reaction (RT-PCR).[4] Analogous to ELISA principles, an immunospotting assay (ISA) has been used for diagnosis. A low volume of serum sample is applied onto a nitrocellulose membrane and a labeled antibody is used for detection. The possibility of applying the sample directly to a high surface area nitrocellulose membrane allows the use of low sample volume and avoids the necessity of two antibodies for capture and detection. Generally, the immunospot test allows diagnoses in less than one hour with high specificity and sensitivity, low complexity and by using conventional apparatus in clinical analysis laboratories. Although these techniques have many advantages, their application is limited in environments where storage and use conditions are not well controlled. The use of ELISA at high temperatures can cause significant loss of enzymatic acitivity or even denaturation of the enzyme, which de-

creases the sensitivity or excludes its application due to unreliable results. Several strategies have been described to overcome the limitations of ELISA, e.g., replacing the detection label by nanoparticles.[5–8]. However, the sensitivity of these novel approaches is still not comparable with the high sensitivity of colorimetric reactions catalyzed by enzymes. A step forward towards the use of enzymes in harsh conditions has been made with the incorporation of enzymes or prostetic groups into nanoparticles.[9,10] The encapsulation increases the stability, thus avoiding unfolding and destabilization of the native conformation. This approach allows the development of more robust assays based on enzymes.[11] As already described in section 1.6, enzymes have also been successfully incorporated into mesoporous silica particles. Thus, the use of mesoporous silica particles can provide enzyme stabilization for applications that require operations in relatively harsh conditions.

Motivated the necessity to enhance the stability of enzyme-based assays in unfavorable environments, we have developed ELISA and immunospotting assays for DF detection based on mesoporous silica nanoparticles loaded with hemin groups in the core and selective binding sites on the outer shell (Figure 7.1). For early stage detection, a highly conserved viral non-structural glycoprotein (NS1) of the Dengue virus has been used as a high potential analyte target for early DF detection, which is developed in the first day after the onset of symptoms.[12,13]

The detection system is based on core-shell functionalized mesoporous silica nanoparticles. The pores of the MSNs are functionalized with high amounts of hemin molecules. This catalyst is able to convert specific substrates into dye molecules that enable optical read out. To the outer surface, PEG is attached as spacer molecule to ensure diffusion into and from the pores. BSA molecules are attached to PEG for enhanced solvation of the particles. Finally, streptavidin is covalently bound to BSA for the creation of selective binding sites for biotin functionalized antibodies from the ELISA test.

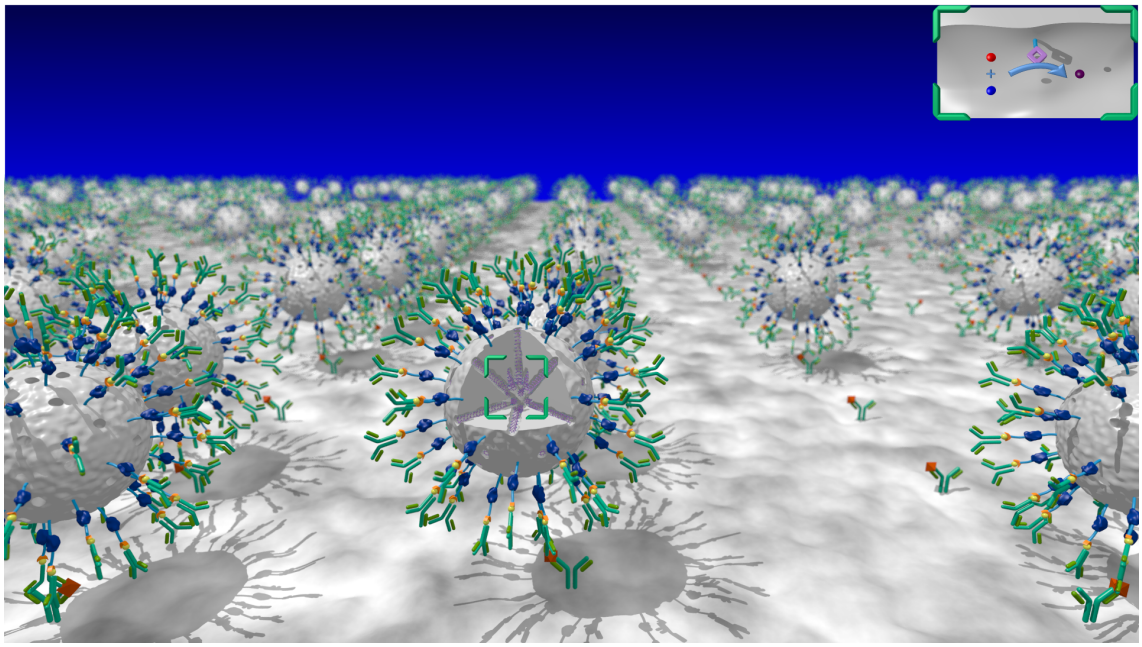

Figure 7.1: Schematic representation of MSNs developed for enhanced NS1 detection. The system consists of MSNs (grey), hemin (purple), PEG (light blue), BSA (dark blue), streptavidin (yellow) and NS1 antibodies (green).

7.2 Experimental Section

Chemicals

Bovine serum albumin (BSA) powder, streptavidin, *N*-(3-Dimethylaminopropyl)-*N*'-ethylcarbodiimide hydrochloride (EDC), biotin-NHS, Tween 20, Tris-HCl, potassium phosphate mono- and dibasic were purchased from Sigma-Aldrich (Milwaukee, USA). Dengue NS1 Ag ELISA was obtained from Standard Diagnostics (Hagal-dong, Korea). Dengue Virus NS1 glycoprotein mouse monoclonal antibody (supernatant) was obtained from Abcam (Cambridge, United Kingdom). Hitrap protein G HP column for affinity chromatography and the PD10 desalting column were purchased from GE Healthcare (Uppsala, Sweden). Nitrocellulose membrane, pore size 5 μm, and Nunc microplate 96-well were purchased from Whatman (Dassel, Germany) and Fisher Scientific (Schwerte, Germany). Backing card was provided by Lohmann (San Jose, USA). For particle synthesis, triethanolamine (TEA, AppliChem, >99%), tetraethyl orthosilicate (TEOS, Fluka, >98%), cetyltrimethylammonium chloride (CTAC, 25 wt% in water), 3-mercaptopropyltriethoxysilane (ABCR, 92%), sodium azide (Fluka, 99%), *N*-(3-dimethylaminopropyl)-*N*'-ethylcarbodiimide hydrochlo-

ride (EDC, Fluka, 97%), hemin (Sigma, >90%), propargylamine (Sigma, 98%), 1-hydroxybenzotriazole hydrate (HOBt, Sigma, >99%), *N*, *N*-diisopropylethylamine (Sigma, 99%), Cu(I)Br (Sigma, 98%), maleimid-PEG(8)-COOH (Iris Biotech), 3-azidopropyltriethoxysilane was synthesized according to a procedure published by Nakazawa *et al.*[14] Doubly distilled water from a Millipore system (Milli-Q academie A-10) was used for all syntheses and purification steps. All solvents and buffer contents were purchased from Sigma-Aldrich. Unless otherwise noted, all reagents were used without further purification.

Preparation of small core-shell-functionalized colloidal mesoporous silica nanoparticles ($\mathbf{MSN}_{100nm}$-$\mathbf{N}_{3core}$-$\mathbf{SH}_{shell}$)

MSN nanoparticles were prepared by a delayed co-condensation approach as described earlier by Cauda *et al.*.[15] Specifically, a two phase mixture of TEA (14.3 g), TEOS (1.63 g, 7.82 mmol) and azidopropyltriethoxysilane (100 μL, 475 μmol) was heated at 90 °C for 20 minutes without stirring. After removal of the oil bath, a preheated (60 °C) solution of CTAC (2.14 mL, 1.62 mmol, 25 wt% in H_2O) and water (21.7 g) was added and stirred afterwards at 500 rpm at room temperature. After 20 min 172 μL (772 μmol) TEOS were added in four steps (43 μL each) every three minutes and the mixture was stirred for 30 min. Subsequently, a mixture of 3-mercaptopropyltriethoxysilane (2.2 μL, 9.4 μmol) and TEOS (40.8 μL, 183 μmol) was added. The resulting solution was stirred overnight at room temperature at 500 rpm. Extraction of the organic template was achieved by heating the ethanol-suspended sample (10 mg/mL) under reflux at 90 °C for 1 h in a mixture of 2 g ammonium nitrate and 100 mL ethanol. Afterwards, the sample was centrifuged for 20 minutes at 19000 rpm (43146 rcf), redispersed in ethanol and heated under reflux at 90 °C in a solution of 8 mL concentrated HCl and 32 mL ethanol for 45 minutes. After centrifugation, the particles were redispersed in ethanol, resulting in a colloidal suspension.

Preparation of large core-shell-functionalized colloidal mesoporous silica nanoparticles (MSN_{300nm}-N_{3core}-SH_{shell})

MSN nanoparticles were prepared by a modified delayed co-condensation approach as described earlier by Cauda *et al.*.[15] Specifically, a two phase mixture of TEA (14.3 g), TEOS (1.63 g, 7.82 mmol) and azidopropyltriethoxysilane (100 μL, 475 μmol) was heated at 90 °C for 20 minutes without stirring. After removal of the oil bath, a preheated (60 °C) solution of OTAB (0.724 g, 1.99 mmol) in water (24.1 g) was added and stirred afterwards at 700 rpm at room temperature. After 20 min 172 μL (772 μmol) TEOS were added in four steps (43 μL each) every three minutes and the mixture was stirred for 30 min. Subsequently, a mixture of 3-mercaptopropyltriethoxysilane (2.2 μL, 9.4 μmol) and TEOS (40.8 μL, 183 μmol) was added. The resulting solution was stirred overnight at room temperature at 700 rpm. Extraction of the organic template was achieved by heating the ethanol-suspended sample (10 mg/mL) under reflux at 90 °C for 1 h in a mixture of 2 g ammonium nitrate and 100 mL ethanol. Afterwards, the sample was centrifuged for 20 minutes at 19000 rpm (43146 rcf), redispersed in ethanol and heated under reflux at 90 °C in a solution of 8 mL concentrated HCl and 32 mL ethanol for 45 minutes. After centrifugation, the particles were redispersed in ethanol, resulting in a colloidal suspension.

Acetylene-functionalization of hemin (sp-hemin)

In a 50 mL flask, 162 mg hemin and 80 mg HOBt (2 eq.) were dissolved in 6 mL DMF. Subsequently, 42 μL propargylamine (2.5 eq.) and 220 μL EDC (4 eq.) were added and the solution was stirred for 12 h at r.t.. DMF was evaporated and the crude product was redissolved in chloroform and washed by extraction with water. The obtained dark green solid was used without further purification.

Each of the following steps was carried out identically for both types of particles:

Preparation of hemin-functionalized colloidal mesoporous silica nanoparticles (MSN-hemin$_{core}$-SH$_{shell}$)

100 mg MSN-N$_{3core}$-SH$_{shell}$ were redispersed in 15 mL acetonitrile. Subsequently the amount of 20 mg sp-hemin, Cu(I)Br (12 mg) and N,N-diisopropylethylamine (16 μL) were added to start the click reaction. The mixture was stirred overnight. The sample was washed several times by centrifugation and redispersion in acetonitrile.

PEGylation of MSN-hemincore-SHshell (MSN-hemin$_{core}$-PEG-COOH$_{shell}$)

10 mg MSN-hemin$_{core}$-SH$_{shell}$ were redispersed in a mixture of 2.5 ml ethanol and 2.5 ml SSC-buffer. Subsequently the amount of 2 mg maleimide-PEG(8)-COOH was added and the mixture was stirred at room temperature. After 3 h the sample was washed several times by centrifugation and redispersion in ethanol/water 1:1.

Attachment of BSA to MSN-hemin$_{core}$-PEG-COOH$_{shell}$ (MSN-hemin$_{core}$-BSA$_{shell}$)

To a dispersion of 1 mg MSN-hemin$_{core}$-PEG-COOH$_{shell}$ in 1 ml citrate-phosphate buffer (0.1 M, pH 6.5), 0.3 mg BSA was added. After 30 min incubation at 4 °C, BSA was covalently attached by the addition of 0.5 μl EDC. The mixture was stirred for 30 min and washed afterwards by centrifugation and redispersion in citrate-phosphate buffer (0.1 M, pH 6.5) at 4 °C.

Attachment of streptavidin to MSN-hemin$_{core}$-BSA$_{shell}$ (MSN-hemin$_{core}$-BSA-streptavidin$_{shell}$)

To a dispersion of 1 mg MSN-hemin$_{core}$-BSA$_{shell}$ in 1 ml citrate-phosphate buffer (0.1 M, pH 6.5), 0.1 mg streptavidin was added. After 30 min incubation at 4 °C, streptavidin was covalently attached by the addition of 0.5 μl EDC. The mixture

was stirred for 30 min and washed afterwards by centrifugation and redispersion in citrate-phosphate buffer (0.1 M, pH 6.5) at 4 °C.

Serum samples

Serum samples infected with Dengue virus type 2 from the epidemic in Santos (2002) were obtained by the Sao Paulo Institute of Tropical Medicine, University of Sao Paulo, Brazil. The tests were approved by the ethics committee of the university. The samples were analyzed for NS1 using the commercial kit Platelia^{TM} NS1 (Biorad Laboratories, Marnes-La-Coquette, France).

Conjugation of anti-NS1 monoclonal antibodies with peroxidase

The conjugation was performed adapting the protocol described by Wisdom.[16] An aliquot of 0.1 mg of anti-NS1 was added to 20 μL of phosphate buffer saline, PBS, containing 20 mmol/L of phosphate buffer and 0.15 mol/L of sodium chloride (pH 7.2). Subsequently, 0.3 mg of peroxidase was added to the antibody solution. After mixing the solution, glutaraldehyde was added to a final concentration of 0.2% and the solution was stirred for 2 h at 20 °C. The solution was then diluted by adding 200 μL of PBS and dialyzed overnight against PBS at 4 °C. Afterwards, 2 mL of Tris-HCl buffer (50 mmol/L containing 1 mmol/L of $MgCl_2$ and 2% of BSA) was added.

Biotinylation of anti-NS1 monoclonal antibodies

The amount of 0.1 mg of anti-NS1 antibody was diluted in 1 mL of phosphate buffer and 4 mg of biotin-NHS was added to the antibody solution. The mixture was stirred for 2 h at room temperature. Subsequently, the solution was dialyzed overnight against phosphate buffer (0.01 mol/L, pH 7.4) at 4 °C. The antibodies were freshly biotinylated before their use in the immunoassay.

Sandwich enzyme linked immunosorbent assay

An aliquot of 100 μL of sample (NS1 protein solution or infected serum) was added to a microplate well previously coated with anti-NS1 antibodies (0.83 $\pm$ 0.16 μg of antibody per well). The samples were diluted in phosphate buffer saline (9% containing 2% BSA and 0.01% Proclin 300, as described by the kit company). The microplate was incubated for 60 min at 37 °C. Subsequently, the wells were washed five times with washing buffer (9% phosphate buffer saline, 2% Tween 20, 0.01% Proclin 300) from the commercial kit. Then, 100 μL of 0.001 μg of anti-NS1 antibodies (peroxidase or biotin coated) in phosphate buffer saline (9% containing 2% BSA and 0.01% Proclin 300) was added to the well and kept for 60 min at 37 °C. Then the wells were washed five times with washing buffer. For the assay using streptavidin coated particles, 100 μL of 0.001 mg of particles in phosphate buffer (0.01 mol/L, pH 7.4) were added and incubated for 30 min at 37 °C. After that, the microplate was washed five times with washing buffer and 100 μL of the substrate (0.05% Tetramethylbenzidine, 0.05% chloridric acid, 1.3% sodium acetate and 0.01% hydrogen peroxide) was added. The peroxidase based assay was incubated for 15 min and then 50 μL of sulfuric acid (5 mol/L) stopped the reaction. For the particle based assay, the incubation was kept for 20 min. The positive control consisted of recombinant Dengue NS1 protein and the negative control consisted of a Dengue NS1 protein negative human serum.

Immunospotting assay

A piece of nitrocellulose membrane (7mm x 7mm) was supported on a backing card and fixed on a plastic stick. An aliquot of 6 μL containing the NS1 protein was deposited on the nitrocellulose membrane and dried at ambient conditions. After drying, 20 μL of 5% BSA solution was deposited on the dried droplet. After 2 minutes, the membrane was immersed in a well containing 50 μL of 0.001 μg of biotinylated anti-NS1 previously mixed with 1 μg of particles for 30 min. The membrane was then washed with TRIS-HCl (0.05 mol/L of containing 0.5% of Tween 20) during 3 min. Subsequently, the membrane was immersed in TMB substrate (0.05%

Tetramethylbenzidine, 0.05% chloridric acid, 1.3% sodium acetate and 0.01% hydrogen peroxide) from the commercial ELISA kit. After 20 min, 25 μL of sulfuric acid (5 mol/L) was added to stop the reaction. The whole procedure took approximately 1 h. The membrane was removed and the absorbance of the immersion liquid was measured at 450 nm using a reference wavelength at 620 nm.

7.3 Results and Discussions

Mesoporous silica nanoparticles with azide-functionalized core and thiol-functionalized shell were synthesized by a delayed co-condensation approach. A reaction mixture containing tetraethyl orthosilicate (TEOS), 3-azidopropyl-triethoxysilane (5 mol% of total silica), surfactant (CTAC or OTAB), and triethanolamine (TEA) results in the spontaneous generation of seeds that grow further radially. After 20 min, TEOS was added and the mixture was stirred for 30 min. Finally, a 1:1 mixture of 3-mercaptopropyltriethoxysilane (0.1 mol% of total silica) and TEOS was added to the reaction to yield thiol functionality only at the outer surface of the nanoparticles. Depending on the used surfactant, nanoparticles with sizes of 100 nm (CTAC, MSN_{100nm}) and 300 nm (OTAB, MSN_{300nm}) were obtained. DLS measurements of both samples can be found in Figure 7.2. These data show a fairly narrow size distribution without observeable aggregation for both types of particles.

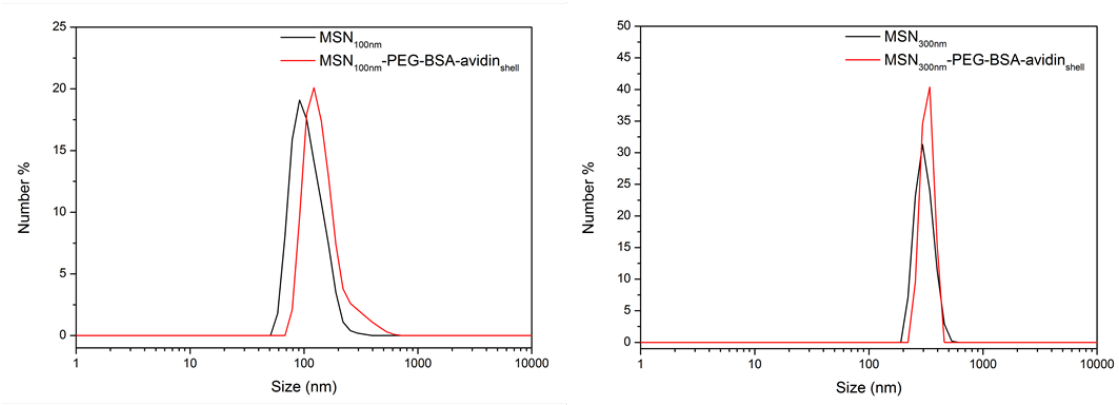

Figure 7.2: DLS data of MSNs synthesized with CTAC (left) and CTAB (right).

The porous properties of the samples were characterized by nitrogen sorption measurements (Figure 7.3). Both particle types resulted in type IV isotherms, typical for MSNs. Brunauer-Emmett-Teller surface areas of 1133 m^2g^{-1} for MSN_{100nm} and 869 m^2g^{-1} for MSN_{300nm} were obtained. Pore sizes of 3.8 nm for MSN_{100nm} and 4.1 nm for MSN_{300nm} were calculated with nonlocal density functional theory. Pore volumes were determined to 0.76 cm^3g^{-1} for MSN_{100nm} and 0.75 cm^3g^{-1} for MSN_{300nm}.

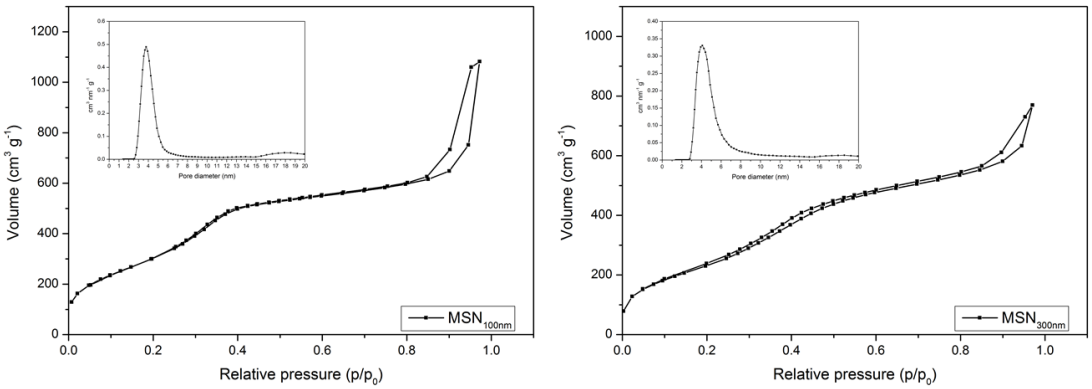

Figure 7.3: Nitrogen sorption isotherms of MSN_{100nm} (left) and MSN_{300nm} (right). Insets show NLDFT size distributions calculated from the isotherms.

In a first step, the cores of the MSNs were functionalized with sp-hemin using a copper-catalyzed click chemistry approach resulting in dark green particles. Subsequently, the outer surface was reacted with PEG to avoid pore clogging through further attachment of the bulky proteins bovine serum albumin and streptavidin. The progress of functionalization was monitored by infrared spectroscopy, thermogravimetric analysis and zeta potential measurements. As the characterization of both particle types featured similar results, only data of MSN_{100nm} will be discussed in the following.

Infrared spectroscopy

The as-synthesized particles show a characteristic azide vibration at 2105 cm^{-1} that almost vanishes after attachment of hemin, confirming the successful click reaction

(Figure 7.4). The next synthesis step was the attachment of PEG to the outer surface of MSNs. This reaction was confirmed by the emerging carbonyl vibrations at 1699 cm^{-1} that can be attributed to the terminal carboxylic acid group of PEG. After attachment of BSA to PEG, the carbonyl vibrations disappear. Additionally, amide signals arising at 1656 cm^{-1} and 1546 cm^{-1} can be assigned to BSA, confirming the successful attachment. In a last step, streptavidin was anchored to BSA. This reaction is indicated by in the further increase of the amide signals at 1656 cm^{-1} and 1546 cm^{-1}.

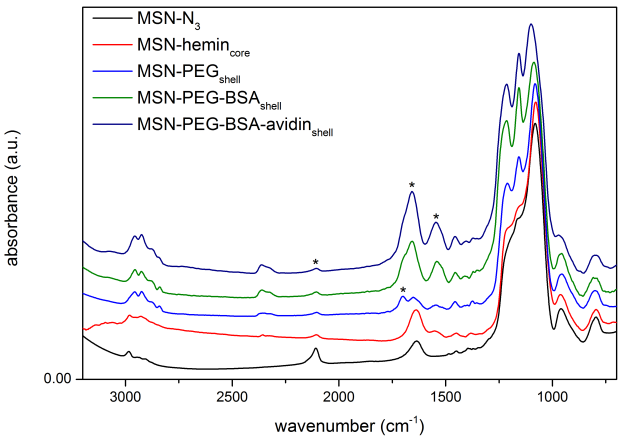

Figure 7.4: Infrared data obtained for each step of the particle synthesis. Signals discussed in the text are marked with an asterisc.

Thermogravimetric analysis

Additionally, all synthesis steps were monitored with TGA (Figure 7.5). The relatively high mass loss for MSN-hemin$_{core}$-SH$_{shell}$ of 13.4% at 600 °C, corresponding to 155 mg hemin per gram particles, reveals the high degree of functionalization of the internal core of the particles. After attachment of mal-PEG-COOH, a further mass loss of 6.2% corresponds to the addition of 66.0 mg PEG per gram particles, confirming a successful reaction. The additional mass loss of 24% of the sample MSN-hemin$_{core}$-PEG-BSA$_{shell}$ corresponds to the attachment of 300 mg BSA per gram particles, confirming an almost 100% reaction efficiency. For streptavidin, the additional mass loss of 8.71% (94.0 mg per gram particles) corresponds to the

attachment of 94% of the inital amount of streptavidin.

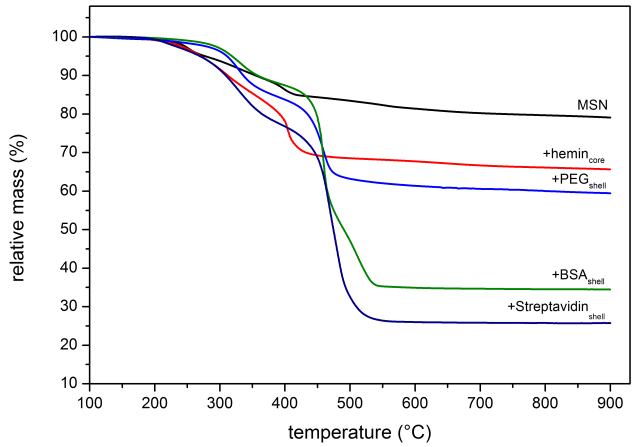

Figure 7.5: TGA data obtained for each step of the particle synthesis.

Zeta potential measurements

Zeta potential data are shown in Figure 7.6. For the as-synthesized MSNs, a zeta potential of +8.5 mV was recorded at pH 2. The attachment of carboxylic acid terminated PEG led to a slight decrease of the zeta potential to +7.5 mV, whereas the attchment of the high molecular weight proteins BSA and streptavidin led to a significant increase in zeta potential up to +30 mV, confirming the successful modification of the particles.

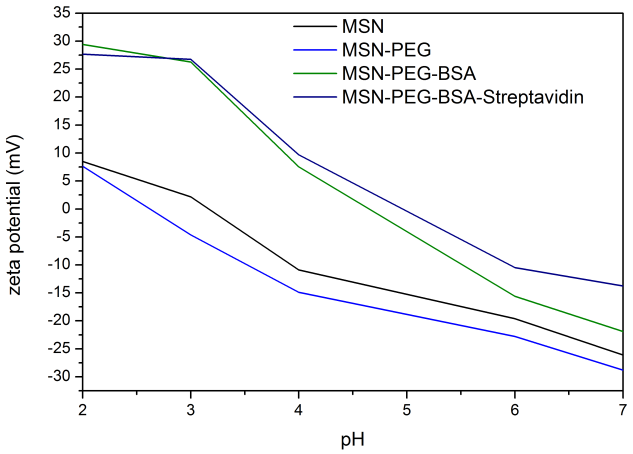

Figure 7.6: Zeta potential data obtained for each step of the surface modification of MSNs.

Finally, the fully synthesized samples were again characterized with DLS (Figure 7.2). For both particle types, the colloidal nature could be maintained. The increase in diameter of around 30 nm corresponds approximately to the size of the attached functionalities. Additionally, the data show no aggregation of the particles, which is essential for a good performance in immunoassays. The need of PEG for the prevention of pore clogging by BSA was shown by the color reaction already applied for hemin in chapter 3 (Figure 7.7). For samples using PEG as spacer molecules, much faster reaction kinetics were observed compared with samples where BSA was directly attached to the surface of MSN.

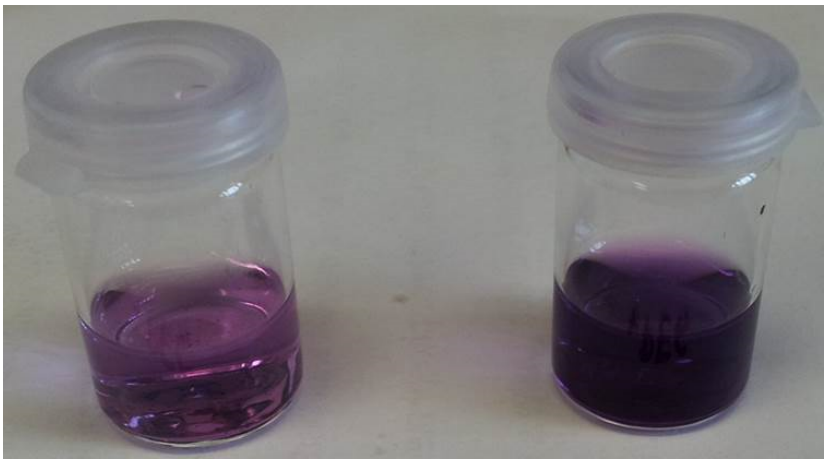

Figure 7.7: Comparison of catalytic activity of hemin for MSNs without (left) and with PEG acting as spacer molecule (right).

Performance of MSNs in immunosorbant assays

In order to investigate the potential of the mesoporous silica particles as labels for diagnostic purposes, an enzyme linked immunosorbent assay was performed for Dengue fever detection and compared to conventional assay using peroxidase labeled antibodies. The analytical curves are depicted in the Figure 7.8 a. Two sizes of particles, 100 nm and 300 nm, were used and compared in terms of absorbance intensity. The results indicate that the hemin groups incorporated into the particles, are a better label in comparison to the bare peroxidase for NS1 protein concentrations below 0.1 μg/mL. Above this concentration, the bare enzyme produces higher signal intensity. This behavior can be related to a particle hindrance effect on the binding sites of the antibody coated well. This means that for higher NS1 concentrations, the distance between the NS1 molecules are too small to be addressed by two seperate MSN particles. The 100 nm particles showed better performance than the bigger particles with a diameter of 300 nm.

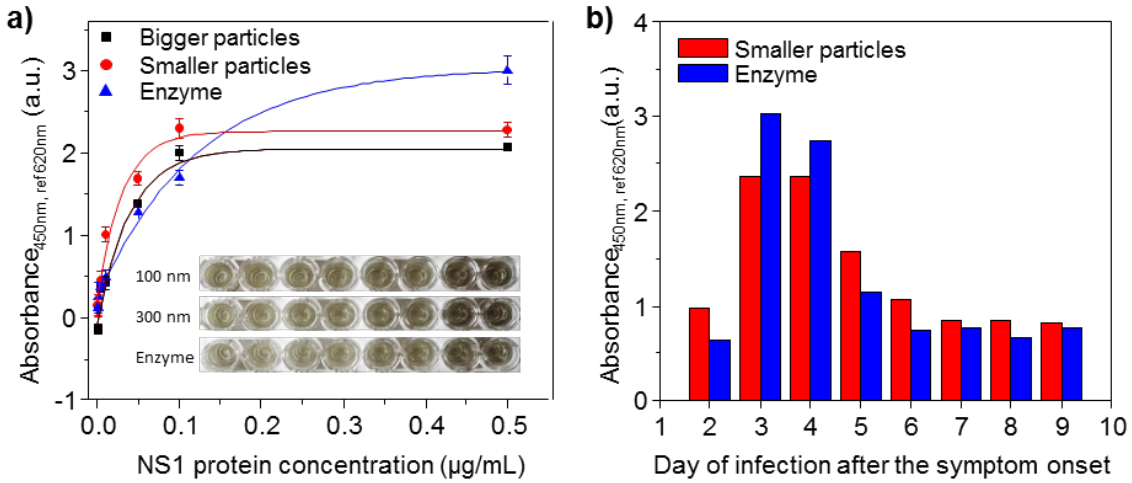

Figure 7.8: Analytical curves (a) for Dengue NS1 protein detection using particles and bare enzyme and a picture of the immunoassay microplate. Comparison of the NS1 protein detection signal (b) of serum samples from the 2^{nd} to the 9^{th} day of the infection after the onset of the symptoms.

The highest sensitivity is observed when using the particles at lower concentrations, this indicates the potential of this system for early Dengue fever detection. Libraty *et al.* showed that plasma levels of free Dengue-2 virus secreted NS1 protein

by day of illness vary between 0.15-0.25 μg/mL for the second day of the disease for patients infected with secondary infections and Dengue hemorrhagic fever.[17] This means that the assay using the MSN particles is able to provide a more realiable diagnosis in the first day of the infection in comparison to the conventional ELISA. The assay based on the particles was also used to examine infected serum samples after different days of the infection after the onset of the symptoms from the Dengue type-2 virus epidemic in Santos, Brazil, from 2002. The Figure 7.8 shows that the conventional assay provides higher signal in the second and third day of the infection, when the NS1 protein release reaches its highest concentration in the patient blood. The graph follows the same behavior described by Libraty and colleages and the maximum coincides with the viremia peak. On the other hand, for the first day of the infection, and from the fifth day on, the immunoassay using particles provided higher signals than the bare enzyme.

Based on these results, the immunoassay using MSNs does not only provide a more stable label by using a molecular catalyst instead of a protein catalyst, but also provides more reliable results for early (before second day) and late (after 5^{th} day) detection. To benefit from these characteristics, an immunoassay to be used in impoverished environments and providing more reliable and fast results was developed based on immunospotting principles. The Figure 7.9 a shows a scheme of the assay that includes the addition of only 6 μL of serum on a nitrocellulose membrane.

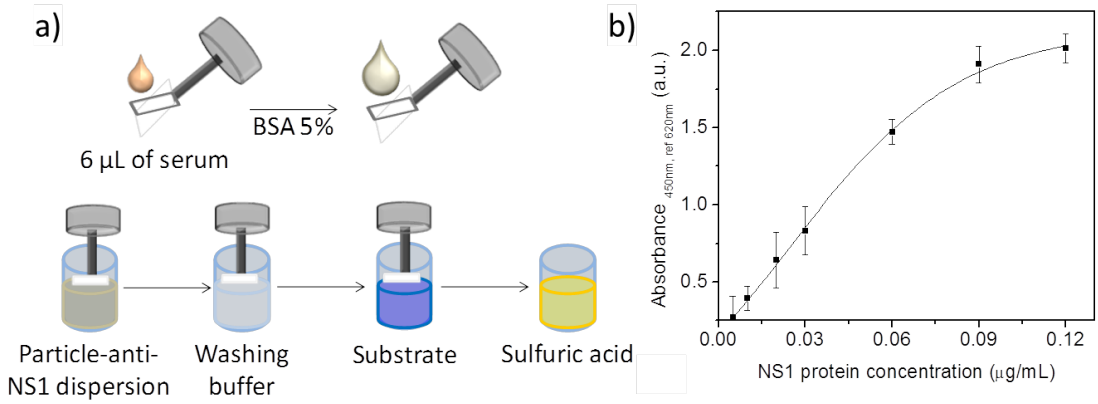

Figure 7.9: (a) Scheme of the immunospotting assay steps using a nitrocellulose membrane. Analytical curve (b) for the NS1 protein detection using nitrocellulose membrane.

After blocking with BSA, the membrane is immersed in particle-anti-NS1 dispersion. The membrane, previously washed with Tween 20, is added into a tetramethylbenzidine (TMB) solution and the reaction is stopped after 15 min by the addition of sulfuric acid. Subsequently the absorbance of the solution can be measured. This assay is cheaper than the above described one, because less chemicals are used and only one antibody is necessary, avoiding the necessity to find antibodies that bind to different epitopes of the protein. The possibility of applying the sample directly to a high surface area nitrocellulose membrane also allows the use of low sample volumes and avoids the necessity of two antibodies for capture and detection. Furthermore, the immunospotting assay allows diagnosing Dengue fever in less than one hour, instead of 3 h for the conventional ELISA, with high specificity and sensitivity, less complexity and using conventional apparatus in clinical analysis laboratories.

7.4 Conclusions

To conclude, we have shown the successful synthesis of MSN-hemin$_{core}$-PEG-BSA-streptavidin$_{shell}$ nanoparticles. These particles were tested regarding their ability to act as a diagnostic label for the early stage detection of Dengue fever. Results obtained for sandwich ELISA experiments revealed the high potential of these nanoparticles for the detection of very low NS1 protein concentrations. When comparing particle types with different sizes, better performance was obtained for smaller par-

ticles with a mean diameter of 100 nm. In comparison to conventional enzyme-based ELISA, these new particles showed better performance for low NS1 protein concentrations, whereas for higher concentrations the conventionals enzyme based ELISA results higher signals. We attribute these observations to a particle hindrance effect on the binding sites of the antibody coated well. Furthermore, the particles were tested in a nitrocellulose-based detection approach where the ability to detect NS1 proteins could also be demonstrated.

Bibliography

[1] WHO. (2010).

[2] WHO. (2012).

[3] Allwinn, R. *Medical Microbiology and Immunology* **200**(3), 155–159 (2011).

[4] Kumarasamy, V., Wahab, A. A., Chua, S., Hassan, Z., Chem, Y., Mohamad, M., and Chua, K. *Journal of Virological Methods* **140**(1-2), 75–79 (2007).

[5] Ambrosi, A., Airo, F., and Merkoci, A. *Analytical Chemistry* **82**(3), 1151–1156 (2010).

[6] Chunglok, W., Wuragil, D. K., Oaew, S., Somasundrum, M., and Surareungchai, W. *Biosensors & Bioelectronics* **26**(8), 3584–3589 (2011).

[7] Piao, Y., Lee, D., Lee, J., Hyeon, T., Kim, J., and Kim, H.-S. *Biosensors & Bioelectronics* **25**(4), 906–912 (2009).

[8] Velappan, N., Clements, J., Kiss, C., Valero-Aracama, R., Pavlik, P., and Bradbury, A. R. M. *Journal of Immunological Methods* **336**(2), 135–141 (2008).

[9] Hu, X., Spada, S., White, S., Hudson, S., Magner, E., and Wall, J. G. *Journal of Physical Chemistry B* **110**(37), 18703–18709 (2006).

[10] Diaz, J. F. and Balkus, K. J. *Journal of Molecular Catalysis B-enzymatic* **2**(2-3), 115–126 (1996).

[11] Ispas, C., Sokolov, I., and Andreescu, S. *Analytical and Bioanalytical Chemistry* **393**(2), 543–554 (2009).

[12] Linares, E. M., Kubota, L. T., Michaelis, J., and Thalhammer, S. *Journal of Immunological Methods* **375**(1-2), 264–270 (2012).

[13] Queiroz Lima, M. d. R., Ribeiro Nogueira, R. M., Schatzmayr, H. G., and dos Santos, F. B. *Plos Neglected Tropical Diseases* **4**(7) (2010).

[14] Nakazawa, J. and Stack, T. D. P. *Journal of the American Chemical Society* **130**(44), 14360–14361 (2008).

[15] Cauda, V., Schlossbauer, A., Kecht, J., Zürner, A., and Bein, T. *Journal of the American Chemical Society* **131**(32), 11361–11370 (2009).

[16] Wisdom, G. B. *Methods in molecular biology* **295**, 127–130 (2005).

[17] Libraty, D., Young, P., Pickering, D., Endy, T., Kalayanarooj, S., Green, S., Vaughn, D., Nisalak, A., Ennis, F., and Rothman, A. *Journal of infectious diseases* **186**(8), 1165–1168 (2002).

Chapter 8

Conclusions and Outlook

In the present work, different classes of nanometer-sized, mesoporous materials for the use in biocatalysis, targeted drug delivery and immunoassay applications have been developed.

In a first project, the impact of pore-wall modifications on the internal pH of mesoporous silica systems was presented. It was shown that depending on the nature of inner functionality, the pH inside the pores differs significantly from the pH in an external buffer solution. By incorporation of catalytic systems into the pores, the strong impact of different pore-wall modifications on the catalytic activity was demonstrated. It is anticipated that with the knowledge about the impact of pore-wall modification on the catalytic activity of incorporated catalysts, new high performance catalyst systems can be developed.

In chapter 4, the synthesis of colloidal nanosized carbon spheres by a reverse opal synthesis approach was discussed. After surface oxidation, these particles were loaded with calcein and sealed with a supported lipid bilayer. The addition of surfactant caused rupture of the bilayer and the dye was able to diffuse out of the particles. To the best of our knowledge, we were the first group achieving an on demand release system based on mesoporous carbon. In future experiments, this drug delivery system has to be studied regarding its ability for targeted on demand delivery of drugs *in vitro* as well as *in vivo*.

In chapter 5, we have developed a multifunctional drug delivery vehicle based on

polymer-functionalized mesoporous silica nanoparticles. With this system, the pH-responsive delivery of membrane-permeable as well as impermeable substances was demonstrated. The addition of targeting ligands allowed the system to distinguish between different cells. Biodistribution experiments *in vivo* revealed no agglomeration and an almost complete excretion of the particles within 72 h after intravenous administration in mice. In the future, this system should be further developed, to achieve similar targeting efficacy in mice as has been obtained in single cell experiments. We anticipate that the possible integration of almost any functionality of interest, as well as the efficient synthesis makes this system a very promising approach for wide-ranging applications, especially in cancer therapy.

In a further project, this polymeric cap system was transferred to MOF nanoparticles. We could demonstrate that it is possible to functionalize the nanoparticles with poly(2-vinyl pyridine) without affecting the porosity, shape and crystallinity of the nanoparticles. Finally, the ability of the system to act as a potential drug delivery vehicle was demonstrated by *in vitro* release experiments of a model drug. In future experiments, this drug delivery system should be studied regarding its ability for targeted on demand delivery of drugs *in vitro* as well as *in vivo*.

Finally, knowlegde on catalysis and targeting of biomolecules obtained in this work was used to create mesoporous silica nanoparticles for the detection of Dengue fever. In comparison to conventional enzyme-based ELISA, these new particles showed better detection performance for low Dengue-related NS1 protein concentrations. Additionally, the particles were successfully used in a nitrocellulose-based detection approach for NS1 proteins. In further experiments, this system could be further refined to develop commercially viable low-cost detection systems.

In summary, the findings of this work expand the scope of applications of various nanosized mesoporous particle-based systems. We could demonstrate that interdisciplinary collaborations offer the possibility to develop new classes of materials with unique properties. Additionally, we could gain a deeper understanding of host-guest interactions, that offer a starting point for the development of high performance catalysis and sensing devices.

Chapter 9

Curriculum vitae

Persönliche Daten:

Name:	Stefan Niedermayer
Geburtsdatum:	4. Dezember 1983
Geburtsort:	Eggenfelden
Nationalität:	Deutsch

Studium/Schulausbildung:

04.2013 - heute	**Ludwig-Maximilians-Universität München** Studium der Pharmazie
04.2011 - heute	**FernUniversität Hagen** Studium der Betriebswirtschaftslehre
11.2009 - heute	**Ludwig-Maximilians-Universität München, AK Prof. Bein** Promotion mit dem Thema "Mesoporous Nanoparticles for Sensing, Catalysis and Drug Delivery Applications"

01.2009 - 09.2009	**Commissariat à l'Énergie Atomique (CEA), Saclay, Frankreich** Diplomarbeit mit dem Thema "Block Copolymer Alignment using Nanoimprint Lithography" Arbeit wurde an der Universität Regensburg eingereicht
10.2007 - 09.2009	**Universität Regensburg** Vertiefungsstudium, European Master of Science "Complex Condensed Materials and Soft Matter" **Abschluss:** Diplom (Note 1,1)
09.2006 - 02.2007	**University of Bath, Sommerset, England** Auslandssemester mit Forschungsarbeit mit dem Thema "Research on the mechanism of lewis-acid catalyzed opening of α-epoxyalcohols"
10.2004 - 09.2007	**Universität Regensburg** Grundstudium im Fach Chemie
09.1994 - 07.2003	**Karl-von-Closen Gymnasium Eggenfelden**

Stipendien/Auszeichnungen:

05.2010 - 04.2013	Kékulé Stipendiat des "Fonds der Chemischen Industrie"
06.2010	Dr. Alfons Paulus Preis für herausragende Studienleistungen
01.2009 - 05.2009	Stipendiat des Deutschen Akademischen Austausch Dienstes, DAAD

Arbeitsverhältnisse/Zivildienst

07.2002 - 06.2004	**SV Wacker Burghausen**
	Vertragsamateur in der Abteilung Fußball
11.2009 - 08.2004	**Seniorenzentrum Massing**
	Zivildienstleistender als Hausmeister und Seniorenbetreuer

Zusatzqualifikationen

Sprachkenntnisse:	Deutsch (Muttersprache)
	Englisch (Verhandlungssicher)
	Französisch (Fließend)
EDV-Kenntnisse:	Betriebssysteme: Windows, Linux
	Microsoft Office, Adobe Photoshop

Chapter 10

Publications and Presentations

10.1 Publications

J. Hunger, S. Niedermayer, R. Buchner, G. Hefter, "Are Nanoscale Ion Aggregates Present in Aqueous Solutions of Guanidinium Salts?", *Journal of Physical Chemistry B*, **2010**, 114 (43), 48-55.

P. Thebault, S. Niedermayer, S. Landis, N. Chaix, P. Guenoun, J. Daillant, X.K. Man, D. Andelman, H. Orland, "Tailoring Nanostructures Using Copolymer Nanoimprint Lithography", *Advanced Materials*, **2012**, 24 (15), 1952-1955.

S. Niedermayer, M. Ilg, E. Calta, A. Schlossbauer, T. Bein, "Tuning the Activity of Immobilized Enzymes via Pore-Wall Modifications of Mesoporous Silica Particles with pH-active Functionalities", *to be submitted.*

B. Mandlmeier, S. Niedermayer, A. Schmidt, J. Schuster, T. Bein, "Lipid-bilayer Coated Nanosized Bimodal Mesoporous Carbon Spheres for Controlled Release Applications", *to be submitted.*

S. Niedermayer, V. Weiss, A. Herrmann, A. Schmidt, D. Edinger, E. Wagner, C. Bräuchle, T. Bein, "Multifunctional Polymer-Capped Mesoporous Silica Nanoparti-

cles for pH-responsive targeted Drug Delivery", *in preparation.*

S. Niedermayer, E. Linares, S. Thalhammer, T. Bein, "Enhanced NS1-Antigen detection using Multifunctional Mesoporous Silica Nanoparticles", *in preparation.*

10.2 Presentations

S. Niedermayer, A. Zürner, A. Schlossbauer, T. Bein, Poster presentation at the CeNS summer school, Venice (Italy), 2010

S. Niedermayer, M. Ilg, E. Calta, A. Schlossbauer, T. Bein, Poster presentation at the NIM Winterschool, Kirchberg (Austria), 2011

A. Schlossbauer, V. Cauda, A. Sauer, S. Niedermayer, C. Bräuchle, T. Bein, Poster presentation at the 5^{th} Annual Symposium on Nanobiotechnology, Seoul (Korea), 2011

S. Niedermayer, M. Lichtnecker, T. Bein, Poster presentation at the conference on Nanomaterials for Biomedical Technologies, Frankfurt (Germany), 2012

S. Niedermayer, V. Weiss, A. Schmidt, T. Bein, Poster presentation at the Herrenhausen Conference, Downscaling Science, Hannover (Germany), 2012

S. Niedermayer, V. Weiss, A. Schmidt, A. Herrmann, D. Edinger, E. Wagner, C. Bräuchle, T. Bein, Oral presentation at the MRS Spring Meeting, San Francisco (CA, USA), 2013

S. Niedermayer, V. Weiss, A. Schmidt, A. Herrmann, D. Edinger, E. Wagner, C. Bräuchle, T. Bein, Poster presentation at the 7^{th} Annual Symposium on Nanobiotechnology, Bristol (UK), 2013

B. Rühle, M. Davies, S. Niedermayer, C. Bräuchle, T. Bein, Poster presentation at the SFB749 meeting, Wildbad Kreuth (Germany), 2013

List of Figures

List of Tables